On the Late Permian Thermohaline Circulation

A Study of the Ocean Circulation and its Relation to the Permian-Triassic Extinction

Eirin Arnesen

Oppgave for graden
Master i Meteorology and Oceanography
60 studiepoeng

Department of Geosciences
Det matematisk-naturvitenskapelige fakultet

UNIVERSITETET I OSLO

Våren 2017

On the Late Permian Thermohaline Circulation

A Study of the Ocean Circulation and its Relation to the Permian-Triassic Extinction

Eirin Arnesen

Abstract

by

In this thesis, the large-scale thermohaline circulation in the Late Permian was studied. A steady state circulation was obtained by running MITgcm with a $2^\circ \times 2^\circ$ spherical-polar grid, and solving the nonlinear equations of motion until an equilibrium state was obtained. The results were compared to some linear theories on the ocean circulation, and a similar model study for a square basin ocean. The goal was to discuss the relevancy of these simplifications to the Late Permian ocean. Additionally, the results were discussed in terms of some previous numerical and proxy-based studies. The objective was to illustrate how the ocean circulation in this period could have contributed to the anoxic and euxinic conditions observed on the Permo-Triassic boundary, in relation the End Permian extinction, and to explore the uncertainties related to plaeoclimatic studies, both numerical and paleogeological. Such comparison studies can be useful in order to explore the causes for oxygen depletion in the Late Permian ocean, and separate out the causes for local extinction rates. The conditions on Permo-Triassic boundary are also highly relevant in order to understand the current climate changes, as rapid increase of atmospheric CO_2 is thought to be the main trigger of the End Permian extinction.

It was shown that both the linear models and the square basin case holds some similarities to the Late Permian ocean, but neither is a satisfactory simplification. Regarding the previous numerical and proxy-based studies, it was found that the circulation is highly sensitive to bathymetry, particularly in highly studied areas. Also, localities where anoxic conditions is seen in the proxy data, do not necessarily coincide with areas of stagnation. The results presented in this thesis consists only of a snap shot of the ocean circulation prior to the extinction event. Thus it can not be directly compared to the situation during and after the extinction. The aim is to illustrate how pairing numerical models and geological data can be advantageous when studying this particular event.

Acknowledgements

I'd like to thank my supervisors, Joe LaCasce and Henrik Svensen for valuable guidance and support. Without you, this thesis would not have been half as interesting. I'd also like to thank my fiancee, Robert Hagala, who in addition to keeping me healthy and happy, did a lot of proofreading and and assisted me with technical matters. Thanks to proffesors Frode Stordal, Pål Erik Isachsen and Lars Petter Røed at the department of Meteorology and Oceanography, for their helpful insights and advice, and to Liv Denstad for supplying me with the model results. Lastly, I'd like to thank Ilan Dehli Villanger for helping me to stay focused and motivated throughout the process of writing this thesis.

Contents

Abstract **v**

Acknowledgements **vii**

1 Background **1**
- 1.1 Introduction 1
- 1.2 The Role of the Ocean 3
- 1.3 Anoxia in the Late Permian 5
  - 1.3.1 On Different Proxies 6
  - 1.3.2 Results from the Late Permian 8
    - Geolocial Results 8
    - Numerical Results 11
- 1.4 Motivation 14

2 Theory of the Buoyancy Driven Circulation **17**
- 2.1 What Drives the Ocean Circulation? 17
  - 2.1.1 The Governing Equations 17
  - 2.1.2 Buouancy as a Driving Mechanism 21
  - 2.1.3 The Stommel-Arons Model 21
  - 2.1.4 The Importance of Mixing 23
- 2.2 The Square Basin Model Run 26
  - 2.2.1 Solutions 27
- 2.3 Topographic Effects 29
- 2.4 On the Choice of Parameters 31

3 Model Description: MITgcm **33**
- 3.1 Model Resolution and Time-Stepping 33
- 3.2 Model Equations and Parameters 36
  - 3.2.1 Gent-McWilliams/Redi parameterization 38
  - 3.2.2 Boundary Layer Mechanisms 39

4 Model results: The Ocean Circulation in the Late Permian 41
4.1 The General Circulation Pattern 41
4.1.1 The Surface Velocity Field 41
4.1.2 The Intermediate/Deep Velocity Field 42
4.1.3 Meridional Mass Transport 47
4.1.4 The Vertical Velocity Field and Convection 49
4.2 Heat Transport 52

5 Discussion 67
5.1 Comparison between the MITgcm Results and the Theoretical Models . 67
5.2 General Discussion and Comparison to the Square Basin Case 68
5.3 Comparison between the MITgcm Results and Paleo Proxy Data 70
5.4 Issues with the Model 71

6 Summary and Concluding Remarks 75

A Calculations 77
A.1 Calculations on mixing 77
A.2 Calculations on the Stommel-Arons model 80
A.2.1 Solutions 82

B The complete Figure 4.10 87

C MITgcm Model Parameters 91

D Thickness of Vertical Layers in MITgcm 93

List of Figures

1.1 The approximate continental configuration at 252 million years ago. The location of some of today's continents are seen. The red font indicate the locations of the super-continents Gondwana and Pangea. The red area shows the approximate location and size of the flood basalt provinces created by the Siberian Traps volcanic eruption. The Figure is adapted from PALEOMAP, Sctotese 2001, and taken from Encyclopædia Britannica. 1
1.2 A typical pyrite framboid composed of cubic crystals, approximately $15\,\mu$m in diameter. The picture is taken from `geology.com`. 7
1.3 Pyrite bed seen (on the dark color) on the transition from the Permian to the Triassic Period. Picture taken from `climatestate.org`. 9
1.4 The approximate locations refered to in this section. The numbers match with the numbers used in the text. The figure is adapted from Scotese 2001, PALEOMAP project and taken from Encyclopædia Britannica. . . . 10
1.5 The simulated SST from Kiehl and Shields [2005]. 12
1.6 The low and high north to south SST-gradient cases of Hotinski et al. [2001] compared to today's (modern) average SST. 13
1.7 A comparison of the bathymetry around the Paleo-Tethys Sea used by Osen et al. [2013] and in the MITgcm model run studied in this thesis. . 14

2.1 Figure adopted from Cessi [2001] and shows the theoretical ocean used in the model. Convective areas are shown in black, and here $w*$ represents diffusive UW. 22
2.2 Figure taken from Vallis [2006]. It shows the pressure field given in (2.15), for $r/\beta = 0.04x_E$, $f = \beta y$, and $y > 0$. Only the northern hemisphere is displayed. The arrows indicate the flow direction. Notice the WBC and the east and northward flowing interior flow. The convective mass source is just north of the domain. The width of the boundary current depends on the ratio of r/β. 24
2.3 Results from LaCasce and Gjermundsen [2017] 28

3.1 MITgcm spherical polar coordinates. longitude λ, latitude ϕ, and r the distance from Earth's center. 34
3.2 MITgcm Model bathymetry. 35
3.3 Three-dimensional staggering of velocity components. 35
3.4 Temperature forcing field $\mathcal{F}_\theta$ shown in °C. 36

4.1 Continuation of horizontal velocities and temperature field in °C. 56
4.2 The blue lines mark the latitudes ($60°$S, $22°$S, $,30°$N, and $60°$N) where the cross-sections of the meridional velocity component v was taken. . . 57
4.3 The variations of the meridional velocity component v with depth z and longitude taken at different latitudes in the NH. The locations of the sections can be seen on Figure 4.2. 58
4.4 The variations of the meridional velocity component v with depth z and longitude taken at different latitudes in the SH. The locations of the sections can be seen on Figure 4.2. 59
4.5 Figure shows the variation of the zonal velocity (u) with z for a single longitude $110°$ E, located in the middle of the Panthalassic Ocean. The vertical axis indicates depth. The velocities are generally small. The $\pm$ signs indicate whether the velocity is eastward (+) or westward (-) in that region, bounded by the black lines. At high latitudes the sign of u varies. 60
4.6 The zonal velocity u and the squared Brunt-Väisälä frequency N^2 for some latitudes along the same longitude ($110°$ E), which is indicated by the vertical black line on figure 4.1 61
4.7 Figure showing the stream function Φ of the poleward transport. The black lines indicate where the transport goes from being negative (southwards) to positive (northwards). The black lines located at $\sim \pm 80°$ show where the wall inhibiting flow into high latitudes is placed (see section 3). The colored values show the total mass transport at a given $z-$level and given latitude. 62
4.8 Figure showing depth-integrated vertical velocity. Purple coloring indicates DW, and yellow UW. 63
4.9 The vertical velocity in $\frac{\mathrm{m}}{\mathrm{s}}$ at different depths for all lon- and latitudes. . 64
4.10 Horizontal (red and green arrows) and vertical transport (blue arrows) for the upper 1200 meters. The negative vertical transport numbers points to UW, while the positive numbers are DW. Only the relevant numbers are shown in this figure. The size of the arrows are proportional to the transport. A full figure can be seen in Appendix B. 65
4.11 The total meridional heat transport given in terawatts ($= 10^{12}$ W) 66

B.1 The full figure showing the horizontal transport between different areas, as in Figure 4.10. The arrows are not scaled to proportion to the transport. Transitions between boxes without arrows indicate transports $< 10^{-4}$ Sv. Red arrows show zonal transport, green arrows meridional. The DW in the different locations is given in the table below. Each box is labeled with one letter from A-F and a number 1-6 given by the names of the columns and rows. 89

List of Tables

4.1 Meridional mass transport in the WBL given in Sverdrups $(1\,\mathrm{Sv} = 10^6\,\frac{\mathrm{m}^3}{\mathrm{s}})$ for selected latitudes. Negative figures refer to southwards, positive numbers to northwards transport. The Return current is the equatorward flowing flow beneath the surface WBC. 47

B.1 The DW (positive numbers) and UW (negative numbers) in the areas marked by the boxes in Figure B.1. 88

D.1 The thickness of the vertical layers used in the MITgcm model run, starting from the surface layer. 94

List of Abbreviations

OGCM	**O**cean **G**eneral **C**irculation **M**odel
WBC	**W**estern **B**oundary **C**urrent
EBC	**E**astern **B**oundary **C**urrent
WBL	**W**estern **B**oundary **L**ayer
EBL	**E**astern **B**oundary **L**ayer
NH	**N**orhtern **H**emisphere
SH	**S**outhern **H**emisphere
SE	**S**outh **E**ast
NW	**N**orth **W**est
U(D)W	**U**p(Down)**w**elling
MOC	**M**eridional **O**verturning **C**irculation
SST	**S**ea **S**urface **T**emperature
GMR	**G**ent **M**cWilliams - **R**edi
PTr	**P**erman-**Tr**iassic
R(L)HS	**R**ight (**L**eft) **H**and-**S**ide

List of Symbols

θ	latitude	
ρ	density	$\mathrm{kg/m^3}$
P	pressure	$\mathrm{kg/ms^2}$
Sv	Sverdrup	$10^6\mathrm{m^3/s}$
b	buoyancy	$\mathrm{kgm/s^2}$
ν	Kinematic viscosity	$\mathrm{m^2/s}$
k	thermal diffusivity	$\mathrm{m^2/s}$
A	Laplacian turbulent eddy viscosity	$\mathrm{m^2/s}$
K	eddy viscosity	$\mathrm{m^2/s}$
κ	diffusivity	$\mathrm{m^2/s}$
u	zonal velocity	$\mathrm{m\,s^{-1}}$
v	meridional velocity	$\mathrm{m\,s^{-1}}$
w	vertical velocity	$\mathrm{m\,s^{-1}}$
∇_H	horizontal gradient	$\mathrm{m^{-1}}$

Chapter 1

Background

1.1 Introduction

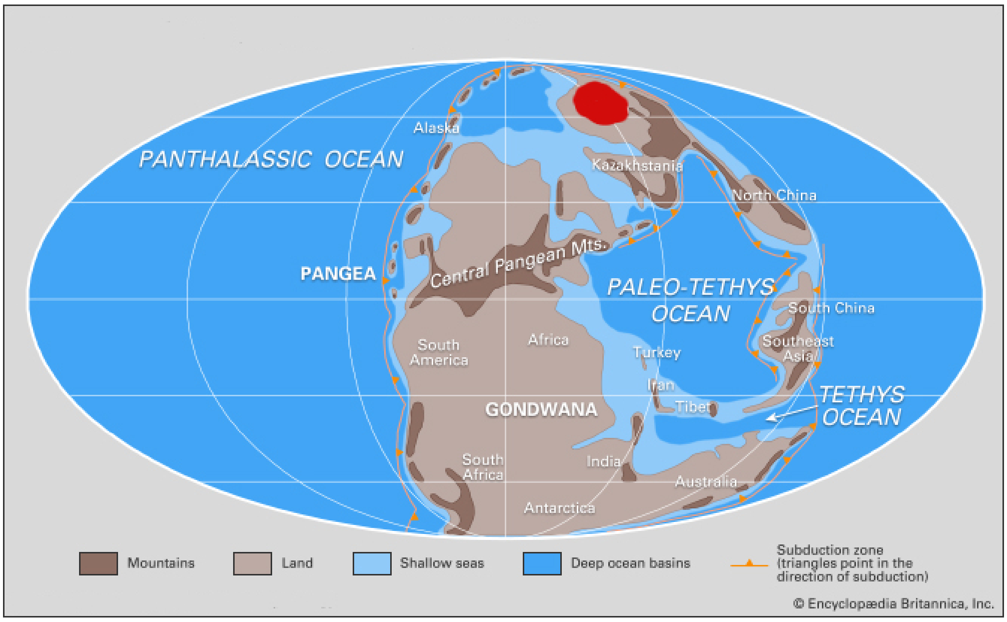
PANTHALASSIC OCEAN
Alaska
Kazakhstania
North China
PANGEA
Central Pangean Mts.
PALEO-TETHYS OCEAN
South China
Southeast Asia
South America
Africa
Turkey
Iran
Tibet
TETHYS OCEAN
GONDWANA
South Africa
India
Australia
Antarctica
Mountains
Land
Shallow seas
Deep ocean basins
Subduction zone (triangles point in the direction of subduction)
© Encyclopædia Britannica, Inc.

FIGURE 1.1: The approximate continental configuration at 252 million years ago. The location of some of today's continents are seen. The red font indicate the locations of the super-continents Gondwana and Pangea. The red area shows the approximate location and size of the flood basalt provinces created by the Siberian Traps volcanic eruption. The Figure is adapted from PALEOMAP, Sctotese 2001, and taken from Encyclopædia Britannica.

Some 252 million years ago, on the Permo-Triassic (PTr) boundary the most severe oceanic mass-extinction known occurred.

During this catastrophe, the loss of biodiversity was disastrous, as it is estimated that approximately 90 % of all marine genra, and half of all marine families were wiped out [Erwin, 2008]. The extinction was so severe that it has been nick-named "The Great Dying". It also marks the transition between the Paleozoic and the Mesozoic era.

The mass extinction coincides with the formation of one of Earth's largest flood basalt provinces, the Siberian Traps, which was formed during a massive basaltic volcanic eruption. Over several hundred thousand years, large amounts of basaltic lava, sulfur, methane, and carbon dioxide was ejected into the atmosphere. Svensen et al. [2009] calculated that the Siberian Traps eruption could result in a release of more than 30 000 GT (1 GT = 10^{12} kg) CO_2 into the atmosphere. However, the observed shift in the carbon cycle could not have been caused by this eruption alone, even with an input this large [Cui and Kump, 2014]. It is commonly accepted that a sudden, massive release of methane from the deep ocean calthrates (or from other sources) account for some of the increase in GHG-concentrations (Berner [2002], Cui and Kump [2014], Benton and Twitchett [2003]).

Some evidence also suggests that the extinction also coincides with changes in the ocean circulation and chemistry, particularly in the redox properties of the ocean, though this claim is disputed. A shift in the marine carbon cycle is also seen on the PTr boundary (Cui and Kump [2014] and references therein).

The timing of the Siberian Traps eruption fits so well that it is unlikely that the mass extinction was unrelated to the eruption. It has also been shown through U/Pb radiometric ages that the mass extinction and the Siberian Traps eruption overlap in part [Svensen et al., 2009]. It is also possible that the volcanic eruption triggered a cascade of feedback mechanisms that eventually lead to the loss of virtually all marine life.

Since the 1970s, researchers have been working on unraveling the Late Permian mass extinction, and only recently has it been determined that the Siberian Traps caused the observed marine organic carbon isotope excursion. The shift in the marine carbon cycle was thus a *result* of the mass extinction, not its cause (Payne and Clapham [2012] and references therein). It can be assumed that changes in the ocean circulation and composition that resulted from the eruption contributed to the extinction. In several studies, the occurrence of marine anoxic or euxinic conditions has been favored as an extinction cause, however, Payne and Clapham [2012] reasoned that the massive volcanic atmospheric carbon input resulted an increase in dissolved inorganic carbon (DIC) and a following decrease in ocean pH, which in turn could drive the marine extinction. Consequently, the importance the PTr anoxic episodes might have had on the extinction may need to be reevaluated. Understanding the ocean circulation is crucial to determining how long-lasting the anoxic or euxinic events were.

Fossil evidence on the selective nature of the marine extinction could indicate that change in ocean oxygen levels as well as an increase in oceanic DIC were vital parts of the event, as species with low tolerance of changes in oxygen, and especially carbon dioxide concentrations faced high extinction rates.

Figure 1.1 shows the approximate continental configuration of the Late Permian Period, together with the names of some continents and the major oceans. The red area indicate the approximate location and expanse of the Siberian Traps basaltic provinces.

1.2 The Role of the Ocean

The ocean has played an important role in the climate throughout the Phanerozoic Eon. Change in sea level, the transport and storage of nutrients, carbon, and oxygen has influenced the evolution of life, and life has in turn influenced the chemical composition of the ocean [Beerling, 2008].

Factors that influence the ocean circulation include changes in the biosphere and in atmospheric conditions, changes in continental weathering rates, and periodic astronomical phenomena [Cronin, 2009]. Thus the strength of the overturning circulation and the overturning time scale varies due to both periodic variability and non-linear relations to the atmosphere and the biosphere. Today the deep water overturning time scale is estimated to 600 years [Toggweiler and Key, 2003], and studies of the PTr-boundary imply that the overturning happened at a somewhat slower rate, depending on bathymetric features [Osen et al., 2013]. It has been shown that the ocean circulation is sensitive to bottom topography, especially at the continental boundaries [Ledwell et al., 2000]. The bathymetry influences the ocean circulation through topographic steering and mixing. Diapycnal mixing is, in the absence of any mechanical forcing from the winds, the only source of eddy diffusivity in the ocean [Vallis, 2006]. The mechanical forcing due to the tides are imperative. Hence uncertainties in paleobathymetry could complicate paleoceanographic studies. The paleobathymetry from the PTr boundary is altogether unknown, but Domeier et al. [2012] quantified the uncertainties in estimating the bathymetry from the PTr-boundary.

To identify the processes driving the ocean circulation, observational data can be analyzed, though that is not an easy option for studies on paleoclimate. Stratigraphic, geochemical, and biological data can be used; to mention some, biomarkers such as alkenones (long chained organic molecules) can be used as a proxy for SST, the ratio of stable isotopes (carbon, oxygen, boron and strontium), in sediment and organic depositions can be used as proxies for ocean productivity, temperature, CO_2-concentration, and ocean pH [Cronin, 2009]. In this thesis the focus will be on the indicators of the ocean redox properties, which is often linked to pyrite formations.

The markers used to determine ocean circulation hold many uncertainties. One major issue is that some past studies presume a casual relationship between the distribution and transport of chemicals and tracers and the ocean circulation, when in fact, the relationship is far from straight forward [Wunsch, 2003]. The transport of chemicals does not necessarily follow the ocean current streamlines. This complicates the study of the Paleozoic seas, as the available stratigraphic data does not yield an unambiguous picture of the ocean.

In many past studies (Hotinski et al. [2001] Kajiwara et al. [1994], Isozaki [1997], Racki and Wignall [2005]), it was found that an increase in atmospheric CO_2-concentrations would lead to a weaker Equator to Pole temperature gradient and a more sluggish overturning circulation. Often researchers related the weakened deep ocean circulation directly to the anoxic or euxinic conditions observed in the PTr shallows. Following Wunsch [2003], linking low oxygen levels explicitly to the sluggishness of the circulation may be an oversimplified conclusion.

The temporal resolution of the stratigraphic data makes sharp changes in the ocean circulation hard to catch [Roscher et al., 2011]. This is a prominent problem for the PTr boundary, as the environmental changes and the mass extinction is believed to have transpired over less than 1 million years (Payne and Clapham [2012] and references therein). Evidence reviewed by Burgess and Bowring [2015] puts even further constraint on the timing of the mass extinction. By utilizing Lranium-Lead Ziricon dating from several locations, they constructed an age model for the event and the links to climate change markers. They concluded that the extinction occurred between $251.941 \pm$ 0.037 and 251.880 ± 0.031 million years ago, i.e. an interval of 60.000 ± 48.000 years.

Most of the stratigraphical data from the end Permian Period is found either on land or on the continental shelves, due to the rate at which oceanic tectonic plates are renewed. The oldest sea floor today are some 200 million years old (apart from some areas of the Mediterranean Sea, which are remains of the Paleo-Tethys, at approximately 270 million years), thus very little deep ocean sediments from the PTr-boundary Panthalassic Ocean is preserved [Müller et al., 2008]. Accordingly, there is a shortage on data on the large scale overturning circulation in the Late Permian.

The ocean circulation at the end of the Permian Period deviates from the present one. First, the difference continental configuration impacts the ocean currents. Today the continents are separated by three large oceans, whereas in the Late Permian, the land masses were gathered in the massive super-continent Pangea, surrounded by the global Panthalasic Ocean Domeier et al. [2012]. Pangea stretched from the South to the North Pole, spanning virtually the entire range of latitudes. Secondly, the climate during the Late Permian was significantly warmer than it is today, and there was no sea or land ice in the northern hemisphere, and only a small amount in the southern hemisphere, if any at all [Roscher et al., 2011].

An understanding of the general ocean circulation at that time can help us understand how different factors could have contributed to the mass extinction that occurred in this time period. To figure out how the ocean circulation was in the Late Permian, comparing several approaches can be useful in order to separate out different effects. In this study, both numerical and analytical models can be used, as well as geochemical studies, which will be looked into in Section 1.3. Analytical ocean models (Pedlosky [1969], Stommel and B. [1959]) are generally linearized, with a flat bottom topography, while the numerical simulations often have more complex boundary conditions, with either realistic or simplified bathymetry and continents. In the numerical models, the non-linear terms of the equations are often included.

1.3 Anoxia in the Late Permian

In this section the main goal is to present the theory behind the use of proxies to determine the prevalence of ocean anoxia and euxina in the Paleozoic era. Some results from the PTr boundary, both numerical and geological will be presented. The results will be briefly compared to the model output studied in this thesis in Chapter 5.

Anoxia is a state characterized by depletion in oxygen ($0.1\,\frac{\mathrm{ml}}{\mathrm{L}} < [O_2] < 2\,\frac{\mathrm{ml}}{\mathrm{L}}$) in portions of the ocean at depths and over a large area. Anoxic conditions develop into euxina when water containing hydrogen sulfide develops. Anoxia has been suspected of being the main cause of the Late Permian marine extinction, though it has been proven that change in the ocean redox cycle was not the only killer [Payne and Clapham, 2012]. Anoxia can not account for the selectivity of the extinction, though species that were particularly sensitive to changes in oxygen levels were hit hard. However, main killer or not, indications of a sudden transition from well-oxygenated situation, to anoxic or even euxinic conditions in the Late Permian and early Triassic are frequently observed in proxy data from shallow habitats, and it should be studied in order to filter out the causes for the Late Permian extinction.

Depletion of ocean oxygen content can be induced in two ways; changes in the availability of nutrients and biological productivity, and changes in the ocean circulation. The mean water age (the elapsed time since contact with the surface) and thus the strength of the ocean circulation is correlated with oxygen levels in the water column. The structure of the MOC can impact the oxygen levels in the ocean, particularly through the depth of the convection at high latitudes. A shallow overturning efficiently cuts off the deep water from the surface, resulting in deep water anoxia, particularly in stagnating areas. Changes in ocean temperatures would also impact the solubility of oxygen. Also, bathymetric features can readily cut off parts of the oceans from the main circulation, and result in anoxic deep and intermediate waters in the cut-off areas.

Enhanced nutrient supply via river runoff can lead to algal blooms, which can rapidly lead to anoxic conditions. Today this is observed particularly near large river deltas close to densely populated areas, i.e. localities where anthropogenic pollution is high [Roberts, 2013]. Regarding the Late Permian extinction, an enhanced nutrient supply could be a result of an increase in continental weathering, subjected to the Siberian Traps volcanic eruption (making fresh rocks available to the atmosphere after a period of little orogeny), and increased temperatures.

The consensus regarding anoxia and extinction is that changes in ocean circulation alone can not account for the extent of anoxia observed on the PTr boundary. Changes in nutrient supply and biological production must have affected the redox cycle as well.

1.3.1 On Different Proxies

Several geochemical and paleoecological proxies can been used to reconstruct the redox history of the ocean. Pyrite petrography, U/Th concentrations, iron concentrations, sulfur isotopes, and biomarkers to mention some (Huang et al. [2016], Wignall and Twitchett [1996]).

While several of these proxies are powerful tools in reconstructing the ocean history, many are sensitive to changes by diagenesis, and thus unaltered samples are required. Huang et al. [2016] based their analysis of the PTr-oceans on Pyrite framboids; spheres of euhedral pyrite crystals. An example of a typical pyrite framboid is seen on Figure 1.2. The original framboidal structure can still be distinguished, even after diagenesis.

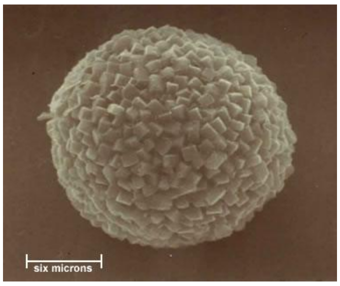

FIGURE 1.2: A typical pyrite framboid composed of cubic crystals, approximately $15\,\mu\mathrm{m}$ in diameter. The picture is taken from `geology.com`.

Furthermore, framboidal pyrite is not affected by surface weathering. The size of pyrite framboids are determined by the redox properties of the local availability of reactants, and thus the abundance and size of the framboids can serve as a proxy for the redox properties of the past ocean Wilkin et al. [1996].

An other way of exploiting how the ocean chemistry depends on the oxygen availability, is looking at the total degree of pyritisation (DOP) of Iron (Fe). Dissolved Fe is categorized as highly reactive (FeHR) and non-reactive Fe. DOP is related to the amount of FeHR which is converted to pyrite. This proxy works because the amount of FeHR converted into pyrite depends on exposure time to sulfide (S^{2-}), which again depends on the oxygen concentration in the water column, as sulfide is more abundant in anoxic environments. DOP is calibrated against bioturbations.

It must be noted that studies have found that DOP must be used cautiously when applied as a proxy for redox conditions [Roychoudhury et al., 2003].

An alternative method, not reliant on pyrite or carbon concentrations consists of analyzing the radioactive decay of Uranium to Thorium [Brennecka et al., 2011]. In anoxic environments, Uranium is reduced to insoluble U^{4+} in a fluride complex, which can be preserved in sediments. During times of oxygen abundance, however, Uranium is converted to U^{6+}-carbonate, which is soluble and thus *not* deposited in sediments. Anoxic sediments are thus more rich in Uranium than oxic ones. Thorium is not affected by the redox conditions, and remains insoluble. Hence the Th/U-ratio depends on the redox properties of the environment at the time of deposition. The methods described above is usually checked against the carbon isotope ratio.

Pyrite (FeS_2) formation is a key process in the employment of several of these proxies.

1.3.2 Results from the Late Permian

Cui and Kump [2014] created an overview of the numerical experiments and proxy data analysis on the PTr boundary. They went though the results from several studies and analyzed their findings. Regarding ocean redox properties, some numerical studies (Hotinski et al. [2001], Winguth and Winguth [2012]) showed a presence of large-scale euxina or anoxia, while others did not (Zhang et al. [2001], Winguth and Maier-Reimer [2005]). The results of the numerical studies on anoxia depended heavily on the nutrient availability in the ocean, frequently prescribed by the phosphate (PO_4) concentration. Without an elevated nutrient supply, the Late Permian ocean circulation patterns do not result in large scale ocean anoxia, even with a prescribed low Equator to Pole temperature gradient. In other words, a combination of both biological and oceanographic factors probably resulted in the anoxia observed in the proxy data.

Due to the geographical location of the Paleo-Tethys Sea it must be regarded in a different light than the Panthalassic Ocean. Its proximity to Pangea and the fact that it is, to a certain degree, separated from the Panthalassic Ocean, could signify that the localities here are more sensitive to change in river runoff (and thus nutrient supply), and the depth of the sills separating it from the Panthalassic. The paleobathymetry, the exact depth of the sills separating the two oceans, where the ocean passages were located, the sea level, and so on is not known in detail [Domeier et al., 2012], and has the potential to completely alter the circulation in the Paleo-Tethys Sea [Osen et al., 2013].

Geolocial Results

Proxy data on the redox properties of the ocean has been studied, from a multitude of localities. Figure 1.4 shows the approximate locations of the results that will be discussed here. The numbers refer to the different studies. The yellow dots show the approximate location of the data used by Isozaki [1997], which will also be discussed. The difference in topography between Figures 1.4 and 3.2 -the topography used in this study - should be noted, particularly the shape of the land surrounding the Paleo-Tethys Sea. The topography in both cases is representative for the Late Permian, and the difference between the two serves to illustrate the uncertainties tied to the paleogeography from this period.

Location 1 was studied by Schoepfer et al. [2012]. Their data was collected in Alberta, Canada. The section they studied was biostratigraphically continuous in the PTr boundary, and consisted of sediment deposited in a deep outer continental shelf setting. On the basis of nitrogen and reduced sulfur isotopes, as well as productivity-sensitive

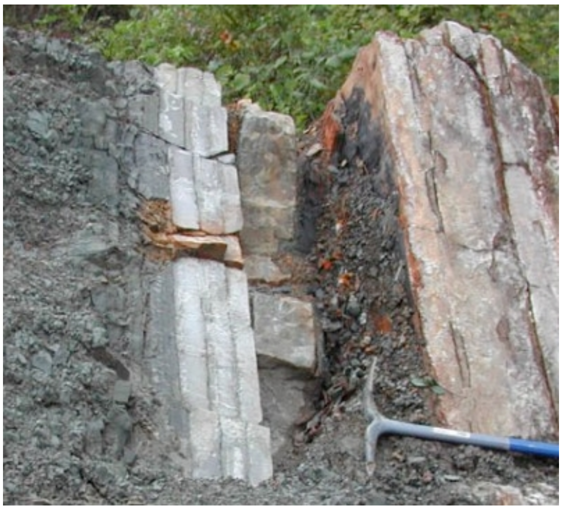

FIGURE 1.3: Pyrite bed seen (on the dark color) on the transition from the Permian to the Triassic Period. Picture taken from `climatestate.org`.

trace elements, they resolved that the location was a highly productive UW zone, with vigorous sulfate reduction occurring in the middle of the water column, in an oxygen minimum zone. These condition lasted until the Late Permian, where an euxinic event set in, represented among other things, by a discrete pyrite bed, as seen on Figure 1.3. This euxinic episode is immediately followed by the extinction of benthic fauna. Following the extinction are indications of termination of the coastal UW system, and a weakening of the mid-water column oxygen minimum. Their result point to prevailing dysoxic conditions in the Early Triassic, possibly due to enhanced continental erosion, and hence increased nutrient input into the ocean. In short, Schoepfer et al. [2012]'s result demonstrate that while a change in the ocean circulation could impact the coastal systems though a reduction of oxygen input from UW, an increase in productivity was probably what drove this particular system towards euxina and extinction.

Location 2 and 3 were studied by Wignall and Hallam [1996]. They studied the abundance of rare earth elements in biogenic apatite of fish and conodonts, along with pyrite formations, sulfur and carbon isotopic ratios to deduce the redox conditions of the ocean at the PTr boundary. Their data was collected in Northern Italy and the Western US (Idaho, Utah, Wyoming). Their results suggested that an abrupt , widespread anoxic event in low latitude marine waters occurred in the Early Triassic, which resulted in the disappearance of several marine taxa. Their results and comparisons to other studies do however, indicate that the anoxic event was confined to shallow waters, and that the

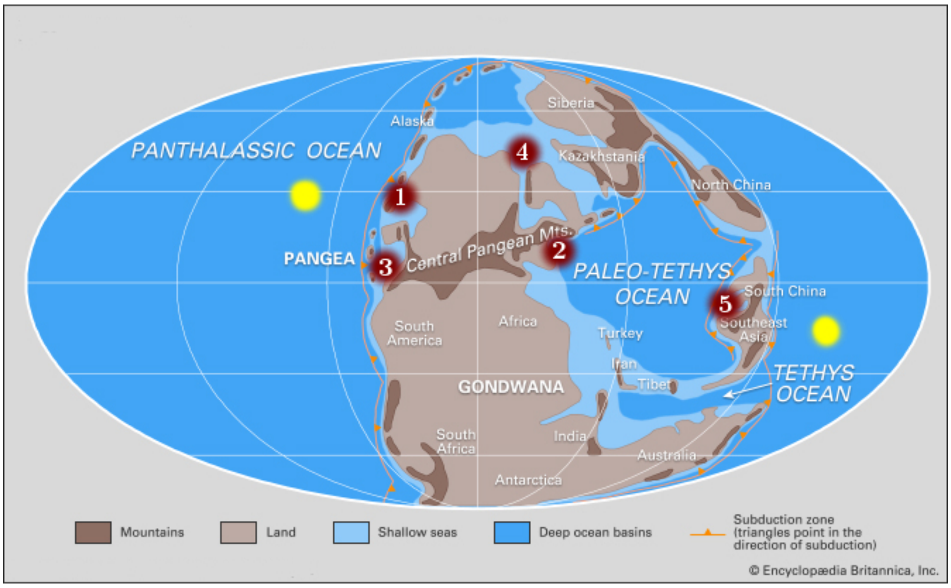
PANTHALASSIC OCEAN
Alaska
Siberia
Kazakhstania
North China
4
1
PANGEA
3
Central Pangean Mts.
2
PALEO-TETHYS OCEAN
South China
5
Southeast Asia
South America
Africa
Turkey
Iran
Tibet
TETHYS OCEAN
GONDWANA
South Africa
India
Australia
Antarctica
Mountains
Land
Shallow seas
Deep ocean basins
Subduction zone (triangles point in the direction of subduction)
© Encyclopædia Britannica, Inc.

FIGURE 1.4: The approximate locations refered to in this section. The numbers match with the numbers used in the text. The figure is adapted from Scotese 2001, PALEOMAP project and taken from Encyclopædia Britannica.

deep ocean waters remained well oxygenated throughout the PTr-transition. This could indicate that increased nutrient supply through enhanced continental weathering and river runoff was the main driver behind the anoxic event. A slowdown in the formation of deep water, and thus the MOC would be reflected in the deep water conditions as well as in the shallows.

Location 4, set in Spitsbergen, was studied by Bond et al. [2015]. The section is located in an area laying on the margin of the Boreal Sea, in the NE of the Panthalassic Ocean. To study the redox properties they utilized pyrite framboid analysis, and the presence of redox sensitive trace metals such as Uranium and Vanadium. The data from Spitsbergen implies that anoxic conditions were prevalent in the Boreal Sea during the PTr transition, but that changes in the redox properties of the ocean was probably not the only killer, as anoxia did not develop in the entire area. Particularly, southern Spitsbergen show no signs of establishing anoxic conditions. The extinction was equally severe in this location as in other areas of the Boreal Sea. Thus the results of Bond et al. [2015] demonstrate that anoxia alone was not the cause of the End Permian extinction.

Location 5, located in South China was studied by Huang et al. [2016]. South China is the most thoroughly studied area from the Late Permian, and Huang et al. [2016] studied more than 100 sections therefrom. They relied on the study of pyrite framboids, anomalies in some rare earth metals, along with analysis of carbon isotope ratios. They were able to reconstruct a detailed history of the ocean redox properties from the Late Permian to the Early Triassic. Overall their result displays three pulses of anoxic and euxinic events in this time period, with the most severe and long-lasting episode occurring in the Early Triassic. Thus their result support the well-established phenomena of intense euxinic or anoxic conditions in the Paleo-Tethys Sea during the PTr transition.

Lastly, Isozaki [1997] studied deep-sea cherts consisting of pelagic sediments primarily deposited in a mid-oceanic deep sea of the Panthalassic Ocean. The locations of these sections on the PTr boundary is marked by the two yellow dots in the Panthalassic, seen on Figure 1.4. In the Middle Permian and the Early Triassic, the prevalence of hematite (Fe_2O_3) suggests oxic conditions. In contrast, the Late Permian to the Early Triassic completely lack hematite, and contain framboidal pyrite, pointing to anoxic deep water conditions. Isozaki [1997] concluded that this deep sea anoxic event lasted for nearly 20 million years. In the Changhsingian (the latest stage of the Permian Period, $\sim 252.2 - 254.1$ million years ago) Isozaki [1997] found evidence suggesting anoxic conditions in the pelagic shallow waters. They concluded that deep-sea ventilation terminated at this stage, creating a "superanoxic" ocean. Even if the data point to such conditions, neither through modeling nor data gathering, has the mechanism that could have generated and sustained such a superanoxic episode been discovered [Cui and Kump, 2014]. Additionally, as have been mentioned earlier, ocean stagnation has often been diagnosed though the presence of large chemical gradients, a relationship that though intuitive, has been proven to be largely incorrect [Wunsch, 2003].

The results presented above will be compared to the MITgcm model results in Section 5.3.

Numerical Results

Kiehl and Shields [2005] ran a numerical experiment using CCSM3 (The Community Climate System Model version 3.0), with 25 vertical levels in the ocean, a horizontal resolution of $3.75°$ and a flat bottom condition. The CO_2-concentration was set to $10\times$ present day levels, or 3350 ppmv, along with a high methane concentration of 0.7 ppmv. Compared to the MITgcm model simulation analyzed in this thesis, Kiehl and Shields [2005] used a continental configuration that leads to less coupling between the Paleo-Tethys and the Panthalassic. Their resulting surface temperature field, seen in Figure 1.5, fits well with Cui and Kump [2014]'s estimations for post-eruption conditions.

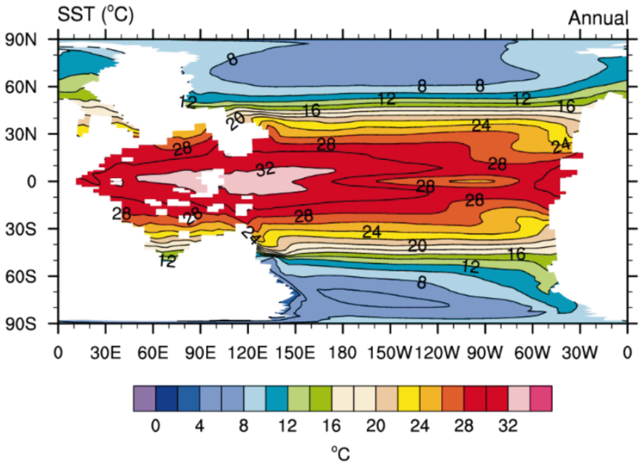

FIGURE 1.5: The simulated SST from Kiehl and Shields [2005].

Kiehl and Shields [2005]'s result show a weak MOC ($\sim 10\,\mathrm{Sv}$). The Paleo-Tethys Sea is particularly stratified, due to its limited connection to the Panthalassic. Warm, less dense waters at high latitudes inhibit deep water formation, and the result is a high mean water age. In the Paleo-Tethys, mean water age exceeds 1000 years. All in all, Kiehl and Shields [2005]'s result show that a relatively shallow and weak MOC, due to high polar temperatures, is sufficient to account for the observed redox conditions in the paleodata, though the authors point out that biological factors probably played a role in the development for the anoxic conditions as well.

Hotinski et al. [2001] ran a 3D ocean general circulation model that included a simple biochemical scheme of phosphate and oxygen cycling with a low Equator to Pole temperature gradient ($28° - 12°$), and comparing the results to a similar run, with a higher gradient ($\sim 32° - 3°$). The temperature forcing of the two cases is seen on Figure 1.6. Their model resolution was similar to that of Kiehl and Shields [2005]. The most striking difference between the low and high temperature gradient runs is the oxygen levels in the deep ocean, at $\sim 4500\,\mathrm{m}$ depth. While the high gradient case show well-oxygenated waters, the low gradient case displays dysoxic or anoxic waters in virtually the entire Panthalassic and Paleo-Tethys Sea. The oxygen level in the low gradient case is, however not low enough to account for the observed amount of sulfur reduction seen in the proxy data. Hotinski et al. [2001] thus concluded that while polar warming in the Late Permian could result in widespread deep ocean anoxia, other factors besides a reduced MOC must have been at play.

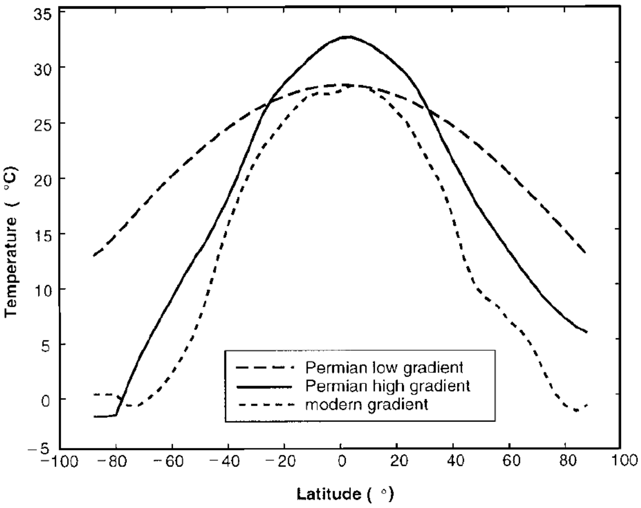

FIGURE 1.6: The low and high north to south SST-gradient cases of Hotinski et al. [2001] compared to today's (modern) average SST.

Lastly, Osen et al. [2013] studied the Late Permian ocean circulation and its sensitivity to bathymetric features. Overall their result show that implementing a mid-ocean ridge at 3000 meters depth do not profoundly alter the circulation. However, the circulation in the Paleo-Tethys is sensitive to the depth of the sill separating it from the the Panthalassic. Adding a shallow area ($\sim$ 200 meters deep, see Figure 1.7a) between the two oceans results in both a slow-down in the circulation in the Paleo-Tethys and an increase in productivity, both of which affect the oxygen concentration negatively. Indeed, the oxygen levels are significantly lower in the case with a shallower sill. The reader is refereed to Osen et al. [2013] for further details. This experiment is of particular interest because the majority of the marine proxydata from the PTr boundary is found in localities close to the Paleo-Tethys Sea. Hence knowledge on the paleobathymetry seems to be of importance, simply because this experiment show that the conditions in these areas are sensitive to the sea floor topography. Note the difference in the bathymetry used in Osen et al. [2013] - Figure 1.7a, and in the model run analyzed in this thesis, seen on Figure 1.7b.

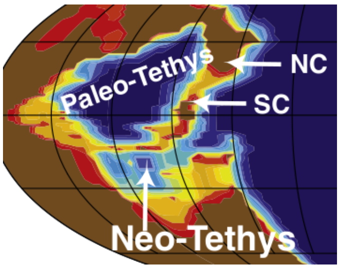

(A) The bathymetry used in Osen et al. [2013]'s experiment with a shallow bathymetry in the Paleo-Tethys Sea. SC = South China, NC = North China. The red coloring represents depths of < 100 meters, yellow $\sim 150 - 300$ meters, the light blue ~ 1000 meters, and finally dark blue ~ 4000 meters.

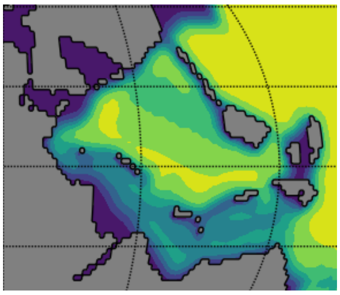

(B) The bathymetry surrounding the Paleo-Tethys used in the MITgcm model run. The coloring scales as on Figure 3.2.

FIGURE 1.7: A comparison of the bathymetry around the Paleo-Tethys Sea used by Osen et al. [2013] and in the MITgcm model run studied in this thesis.

1.4 Motivation

Mass extinctions are seen as important happenings in the history of life on Earth, marking transitions and turning points in evolution. However, due to the restrictive nature of the available geochemical data from deep time, feedback mechanisms in the atmosphere-ocean system occurring on timescales less than ~ 1000 years are poorly understood [Burgess and Bowring, 2015]. Hence the cause and effect relations between the environment and living organisms connected to major events that occur over small timescales remain a mystery. Recognizing the drivers and dynamics of major mass extinctions may help us to further project our own future by predicting the impact of the antrophogenic CO_2-emissions and other effects human activity have on the Earth system and the biodiversity.

In this thesis, the thermally driven flow in the Late Permian Period will be compared similar model run conducted without bathymetry, for a square basin [LaCasce and Gjermundsen, 2017]. The results from the Late Permian will also be discussed in terms of analytical theories. The goal is to determine the relevancy of such simplifications to the Late Permian case. The model results will also be compared to previous paleoceanographic studies described above in Section 1.3. Particularly, shifts in the ocean redox properties will be looked into.

The main goal is to answer the following questions: How well do the thermally forced ocean circulation at the PTr boundary fit with analytical and simplified numerical models of the overturning circulation? Can we use the available paleo proxy data from this period to validate the model results? And, is it possible that a shift in the ocean circulation have been a direct or indirect cause of the worst crisis in the history of life? The answer to the last question is beyond the scope of this thesis, but I hope to open some doors to further research on the matter.

The model results consist only of one snapshot of the circulation pre-extinction, and before the Siberian Traps volcanic eruption occurred, and thus the model results cannot be directly compared to paleodata showing the conditions *after* eruption happened. The goal here is to illustrate how oceanographic circulation models coupled with analysis of geological data can be a good approach to study the PTr-transition.

Chapter 2

Theory of the Buoyancy Driven Circulation

2.1 What Drives the Ocean Circulation?

The major oceanic surface currents are thought to be mainly driven by the wind-stress, while the deep circulation is forced by variations in density, related to thermal and saline forcing [Cessi, 2001]. Others suggest that evaporation and precipitation are major drivers as well [Ferrari and Ferreira, 2011], but the thermal forcing is more important [Marshall and Plumb, 2007]. The meridional gradient in heat influx, where the Equator on average receives energy from the atmosphere, and the polar areas experience a net loss of heat, is the main contributor to the density variations driving the deep circulation. Additionally, mixing over topography due to tidal forces also plays a role.

2.1.1 The Governing Equations

The governing equations are based on fundamental fluid dynamical principles, such as the conservation of mass, momentum, salinity and temperature, and on the principle of conservation of energy. The derivations in this section are heavily based on Vallis [2006].

First we will look at the equation of conservation of mass, here in its Lagrangian form:

$$\frac{\mathrm{D}\rho}{\mathrm{d}t} + \cdot\nabla(\rho\vec{u}) = 0. \tag{2.1}$$

The large scale density variations are small in the ocean, and as we are looking at basin scale motion we can decompose the density ρ into two parts, the background density, which is constant and a perturbation, which varies with all spatial terms. By splitting the density field into two parts like this we effectively filter out longitudinal compression waves (sound waves) with periods and wavelengths much shorter than the typical time and length scale of the motion. This is called the Boussinesq-approximation. Thus we can write:

$$\rho = \rho_0 + \rho'(x, y, z, t)), \tag{2.2}$$

where $|\rho'| \ll |\rho_0|$.

As a result, a fluid parcel with a velocity can be considered incompressible, or,

$$\nabla \cdot \vec{u} = 0, \text{ or } \nabla_H \vec{u} = -\frac{\partial w}{\partial z} \tag{2.3}$$

∇_H is the divergence of the horizontal velocity components, u and v. The reference density field (ρ_0) is associated with a reference pressure field, and by definition they are in hydrostatic balance, i.e.

$$\frac{\mathrm{d}p_0}{\mathrm{d}z} \equiv -g\rho_0, \tag{2.4}$$

where

$$p = p_0(z) + p'(x, y, z, t), \tag{2.5}$$

and we assume that $p_0 >> p'$.

We are looking at the large scale overturning circulation, and thus the full equations may be simplified and the small-scale effects are parameterized to represent their mean effects on the large scale motion. We will start by looking at the full momentum equation and manipulate it:

$$\frac{\mathrm{D}\vec{u}}{\mathrm{d}t} + f\hat{k} \times \vec{u} = -\frac{1}{\rho}\nabla p - g\hat{k} + \vec{F}. \tag{2.6}$$

The terms on the LHS are the total derivative of the motion of a fluid parcel and the Coriolis force. The RHS consists of terms that force the motion of the fluid. The last term represents frictional and turbulent forces. It can be parameterized in many ways. Away from boundaries, it is common to use by momentum diffusion, where $\vec{F} = \nu\nabla^2\vec{u}$.

To obtain the Boussinesq-equatons, we insert

equations (2.2) and (2.5) into the momentum equation, (2.6). This yields

$$\frac{\mathrm{D}\vec{u}}{\mathrm{d}t} + f\hat{k}\times\vec{u} = -\nabla\phi + b\hat{k} + \nu\nabla^2\vec{u}, \tag{2.7}$$

where we have utilized (2.4) and that the perturbations of p and ρ are substantially smaller than the value of the background field.

We define $\phi = \frac{p'}{\rho_0}$ and $b = \frac{-g\rho'}{\rho_0}$, where b is the *buoyancy*. The buoyancy is associated with density differences in the fluid. Thus the buoyancy of a fluid parcel depends on the temperature and the salinity of the parcel and its surroundings. ϕ is the perturbation pressure field.

Next we will look at the thermodynamic equation, which can be expressed in terms of the buoyancy:

$$\frac{\mathrm{D}b}{\mathrm{d}t} = \frac{\partial b}{\partial t} + \nabla\cdot(b\vec{u}) = J + \kappa_h\frac{\partial^2 b}{\partial x^2} + \kappa_h\frac{\partial^2 b}{\partial y^2} + \kappa_z\frac{\partial^2 b}{\partial z^2}. \tag{2.8}$$

J is the non-diffusive heating (external heating), and the second term on the RHS is the diffusive heating. κ is the diffusivity.. Typical values for the ocean are $10^2\,\frac{\mathrm{m}^2}{\mathrm{s}}$ in the horizontal, while the diapycnal value range between 10^{-5} and $10^{-2}\,\frac{\mathrm{m}^2}{\mathrm{s}}$ [LaCasce, 2004].

When working on abyssal flow in the ocean, we can assume that $J \simeq 0$ everywhere except at the surface $(z = 0)$, where solar radiation is absorbed, and heat is lost to the atmosphere. Moreover, external heat sources at the sea floor, such as hydrothermal vents and other geothermals are ignored (The heat influx from geothermals are estimated to $0.05\,TW$, compared to 1 TW estimate for wind forcing [Wunsch and Ferrari, 2004]). If we assume the ocean is in a steady state, (2.8) reduces to

$$\nabla\cdot(b\vec{u}) = \kappa_h\frac{\partial^2 b}{\partial x^2} + \kappa_h\frac{\partial^2 b}{\partial y^2} + \kappa_z\frac{\partial^2 b}{\partial z^2} \tag{2.9}$$

away from boundaries. Applying the Boussinesq-approximation to (2.6) the vertical velocity evolves according to

$$\frac{\partial w}{\partial t}+\vec{u}\cdot\nabla w=-\frac{\phi}{\partial z}+b+\nu\frac{\partial^2 w}{\partial z^2}, \tag{2.10}$$

and applying reasonable scalings for planetary flow, we find that

$$b=\frac{\partial \phi}{\partial z}. \tag{2.11}$$

If we continue by looking at the horizontal components of the momentum equation (2.6), applying the Boussinesq-approximation and scaling the equation for planetary scale motion, while assuming that the Rossby number (the ratio of the advective term to the Coriolis force) is small, we obtain the following equation,

$$f\hat{k}\times\vec{u}=-\nabla_H\phi+\nu\nabla_H^2\vec{u}. \tag{2.12}$$

The H-subscript refers to the horizontal derivative. The horizontal momentum equation, together with the continuity equation (2.3), (2.11) and (2.9) form the *Planetary Geostrophic Equations*, with an added mixing term (the last term on the RHS) to satisfy boundary conditions [Pedlosky, 1969].

This set of equations is a fairly good approximation to the basin scale interior flow in the ocean. They are however, not valid at the Equator, where $f\rightarrow 0$, and our assumption of a small Rossby number is no longer valid.

For seawater, the equation of state -linking the salinity and temperature to the fluid density is empirical- and the first order variation (usually a good approximation) looks as follows:

$$\rho=\rho_0(1+\beta_0(S-S_{\text{ref}})-\alpha_0(T-T_{\text{ref}})), \tag{2.13}$$

where α and β are empirical constants, T is the temperature, and S is the salinity. S_{ref} and T_{ref} are the reference salinity and temperature values.

2.1.2 Buouancy as a Driving Mechanism

The sun transfers energy to the ocean via short-wave radiation, which results in a differential heating at the ocean surface. The lower latitudes gain substantially more energy than the polar regions. On average, the low latitudes receive radiative energy, while the high latitudes experience a net radiative energy loss. To compensate for this skewed heating, the ocean circulates to transfer energy from the Equatorial and subtropical regions to higher latitudes. This is what ultimately drives the oceanic (and the atmospheric) circulation.

The energy is absorbed in the top 100 meters or so in the ocean, depending on biological productivity, water clarity etc. This is called the euphotic zone, where life thrives. As the density of water depends on the temperature (more so than on salinity), the contrast in net radiative energy gain between latitudes result in a difference in density in the surface waters. This yields a meridional density gradient with lighter and warmer waters at low latitudes. This water flows polewards and gradually releases its energy as long-wave radiation to the atmosphere thus increasing its density. This results in convection at high latitude boundaries, where this cool water sinks due to enhanced vertical mixing, and slowly ascends from the abyssal ocean. As of today, one of the largest gaps in our knowledge on the thermohaline circulation is related to the slow UW of abyssal water. We do not know where the UW occurs nor how the ascending water is returned to the regions where deep water is formed.

Several analytical theories has been proposed in order to understand the buoyancy driven part of the ocean circulation, and the analytical theory can be used as tools to understand the underlying concepts and they have historical value. In the following subsection we will look at one of the most influencial theories and discuss the model's short-comings and their fluid dynamical relevance will be discussed. In the discussion (See 5) they will be compared to the model results. The analytical models will not be compared to the paleo data, simply because the restrictions on the analytical models are too severe.

2.1.3 The Stommel-Arons Model

The Stommel-Arons model for abyssal flow was proposed in 1960, and has had a strong influence on physical oceanography. The derivation here is based on Cessi [2001]. It regards the ocean as a two-layer fluid where the lower layer is supplied with mass from the upper layer through convection at high latitudes, and the lower layer loses mass to the upper layer through uniform, diffusive UW. The thickness of the abyssal layer is $H - h$, where H is the total thickness of the water column, while the thickness of the upper layer is h. The density of the lower and upper layer is ρ_2 and ρ_1 respectively. Moreover, we assume that the UW is roughly constant, a small aspect ratio ($= \frac{H}{L}$, where H and L are typical height and length scales of the motion). Also, It is assumed that the ocean is flat-bottomed and that a WBC may be added to satisfy mass conservation. A Cartesian system on the β-plane $(f = f_0 + \beta y)$ will be employed, and I will utilize a variation the planetary geostrophic equations (Equations (2.12), (2.3), (2.11) and (2.9)) derived in section 2.1.1. Rayleigh drag is employed in the viscous term.

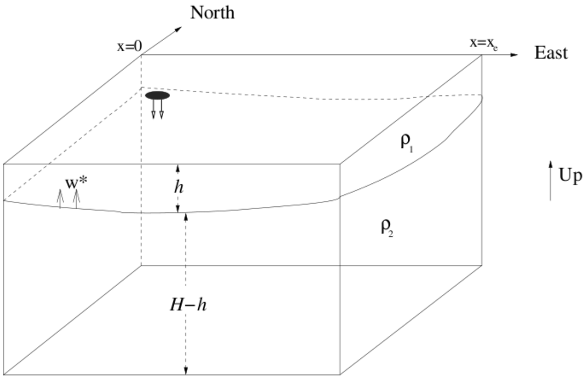

FIGURE 2.1: Figure adopted from Cessi [2001] and shows the theoretical ocean used in the model. Convective areas are shown in black, and here $w*$ represents diffusive UW.

Figure 2.1 shows the theoretical layout of the Stommel-Arons model, taken from Cessi [2001]. The equations will be solved for both layers, and continuity will be employed on the boundary between them. The calculations and further reasoning can be seen in Appendix A.2.

The simplifications utilized in the Stommel-Arons model lead to the dominating balance away from boundaries and convective sources being

$$\beta v_g = f \frac{\partial w}{\partial z}, \tag{2.14}$$

called the *Sverdrup balance*. v_g is the geotrophic, meridional velocity component. In general, this is a good approximation away from boundaries and the Equator. Since we are away from convective sources, w is the *local* mass loss though UW, considered to be uniform. Thus the interior flow (as (2.14) applies) is polewards, regardless of the location of the convective mass source.

Writing the solution in terms of a stream function Φ, and separating solution between the one boundary layer portion, Φ_B, and one interior part, Φ_I we end up with

$$\Phi = \Phi_B + \Phi_I = -2S_0 \frac{y}{y_N} e^{-\frac{r}{\beta}x} + \frac{f^2}{\beta} s_u (x_E - x). \tag{2.15}$$

S_0 is the total rate of DW, i.e. mass flow from the upper to the lower layer in the convective region, y is the meridional, and x the zonal length component, and y_N and x_E the northern and eastern boundary respectively. r is the drag coefficient, and s_u is the mass loss though UW in the lower layer.

The solution is not valid near the convective sources, as this violates the model assumption, and it does not satisfy the condition of non-normal flow at the northern wall. The solution can be seen in Figure 2.2. The values for the dissipation rate r can vary with the scale of the domain Cessi [2001].

For the full calculation on the solution to the Stommel-Arons model, see Appendix A.2.1.

2.1.4 The Importance of Mixing

The Stommel-Arons model regards buoyancy with an uniform UW as the driving force behind the MOC, but the UW actually occurs due to mixing.

Disregarding underwater heat sources such as geothermal vents, the ocean is supplied with heat from the atmosphere through the surface $z = 0$ alone. Hence, as opposed to the atmosphere, the ocean can not be considered a heat engine, simply because the heating occurs at the top, rather than the bottom of the fluid.

Sandström [1908] made the earliest discussion on this (that we know of), on the basis of the second law of thermodynamics and energy conservation. He considered the ocean as a perfect fluid going through the Carnot cycle. It was assumed that the ocean is heated solely at the surface, though not uniformly, as the tropics are heated and the polar areas are cooled. Overall the heating would take place at *lower* pressures than the cooling. This lead to the conclusion that the ocean would end up stagnant, with circulation confined to a thin surface layer driven by a very weak convection at high

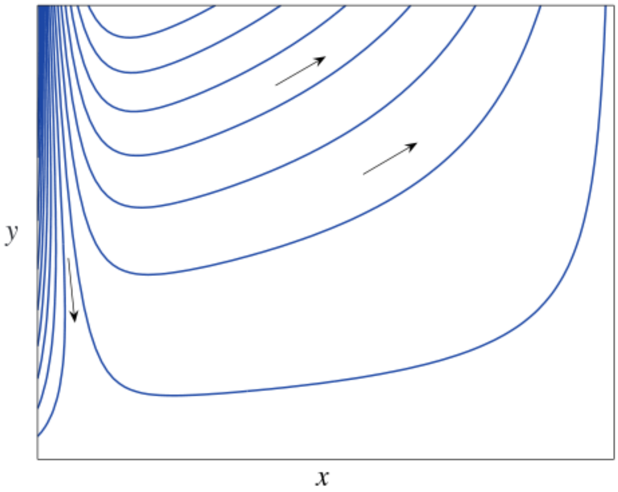

FIGURE 2.2: Figure taken from Vallis [2006]. It shows the pressure field given in (2.15), for $r/\beta = 0.04x_E$, $f = \beta y$, and $y > 0$. Only the northern hemisphere is displayed. The arrows indicate the flow direction. Notice the WBC and the east and northward flowing interior flow. The convective mass source is just north of the domain. The width of the boundary current depends on the ratio of r/β.

latitudes, which would fill the abyss with uniform density fluid. The thin boundary layer at the surface would mark the transition between the deep ocean and the surface temperature.

This result clearly deviates from the real ocean. Sandström [1908]'s reasoning is entirely based on thermodynamics, and does not take the effects of wind stress, tidal forcing or diffusion into account, all of which would alter the model by supplying the system with mechanical energy.

Combining the equation

$$\frac{D}{\mathrm{d}t}bz = z\frac{\mathrm{d}b}{\mathrm{d}} + bw = \langle zJ\rangle + \kappa\langle z\nabla^2 b\rangle + \langle bw\rangle, \tag{2.16}$$

where brackets denote volume integration, with the energy equation

$$\frac{1}{2}\frac{\partial}{\partial t}|\vec{u}^2| = -\vec{u}\cdot\nabla B + wb + \nu u\cdot\vec{\nabla}^2\vec{u}, \tag{2.17}$$

where $\frac{1}{2}|\vec{u}^2|$ is the kinetic energy, E_k, we get the following result:

$$\frac{\mathrm{d}}{\mathrm{d}t}\langle E_k - bz\rangle = \langle zJ\rangle - \epsilon - \kappa\langle z\nabla^2 b\rangle, \tag{2.18}$$

where ϵ is the total energy dissipation given by $\epsilon = -\nu\langle(\nabla \times \vec{u})\rangle$, which is strictly negative. and bz is the potential energy. In steady state we get

$$\langle zJ\rangle = -\epsilon + \kappa\langle z\nabla^2 b\rangle. \tag{2.19}$$

What does (2.19) signify? The term on the LHS is external heating J at level z. In the ocean, most of the heating happen at the surface, where $z = 0$. Hence the LHS $\to 0$. Thus we see that the energy dissipation must be balanced by the diffusive heating.

As $-\epsilon < 0$, the heating and the height z must be negatively correlated, or the mixing must on average, occur on lower $z-$levels than the cooling. This means that circulation can be maintained, in the absence of mechanical forcing, only if the diffusion is non-zero and fulfills (2.19), i.e. diffusion must be so efficient that it can provide a heat source in the deep ocean. We can conclude that mixing is needed for the circulation to penetrate into the interior.

Making a similar argument closer to that of Sandström [1908], it can be shown that heating must occur on lower levels than the cooling in order for *work* to be done to convert potential energy into kinetic energy and maintain the circulation against the retarding force of friction. Sandström's ideas are perfectly thermodynamically sound, and the MOC is generally very sensitive to pressure differences and the locations of heating and cooling. However, in order to maintain the ocean circulation, in the absence of mechanical forcing, mixing is needed.

Wunsch and Ferrari [2004] found that in order to maintain the density distribution related to a global MOC overturning of 30 SV, an energy supply of 2.1 TW is required. They argue that most of this energy is supplied though tidal mixing and wind, each component accounting for $\sim$ 1 TW. The ocean is definitely *not* a heat engine, as it requires mechanical energy to maintain the circulation. The wind, in addition to supplying energy directly also adds energy to the system though generation of internal waves. The exchange of buoyancy between the ocean and the atmosphere holds a marginal contribution to the energy budget, and it might even be negative. Wunsch and Ferrari [2004] estimated that the total release of E_p into the ocean lies between 2 and 3 TW, with some mechanical energy being lost to compensate for frictional forces at work in boundary layers. Regardless of the source of mechanical forcing, the MOC certainly cannot be maintained without it.

The mechanical energy budget of the ocean remains uncertain, but it is clear that most of the diapycnal mixing in the ocean is confined to topographically complex boundaries.

2.2 The Square Basin Model Run

This section is a brief a presentation of LaCasce and Gjermundsen [2017]'s results. Similar studies have been conducted in the past, cf. Marotzke and Scott [1999], Park and Bryan [2001].

LaCasce and Gjermundsen [2017] investigated how a 3D linear model based on Pedlosky [1969] and Salmon [1986] compares with a numerical model for an idealized domain (a square basin with no topography) applied to both models. They omitted both wind forcing and sea ice formation in their numerical simulations in order to compare the buoyancy driven part of the ocean circulation alone.

LaCasce and Gjermundsen [2017] used the Massachusetts Institute of Technology general circulation model (MITgcm), with an ocean-only configuration and no sea ice with a horizontal resolution of $0.45° \times 0.45° \cos(\theta)$, where θ is the latitude. In the vertical they used 24 vertical layers, with increased thickness with depth, stretching over 6000 meters in total. The surface layers' vertical resolution were set to $20\,\mathrm{m}$, while the deep layers spanned up to $900\,\mathrm{m}$.

They applied a surface relaxation temperature given by $27\cos(\theta)$, where θ is the latitude, and a relaxation time of one month. The model spin-up time was 5500 years, which was when a steady state was reached. The thermal diffusion coefficients k_h (horizontal) and k_v (vertical) were set to $10^3\,\frac{\mathrm{m}^2}{\mathrm{s}}$ and $10^{-4}\,\frac{\mathrm{m}^2}{\mathrm{s}}$, despite varying in space in the real ocean. A horizontal viscosity of $\nu = 10^4\,\frac{\mathrm{m}^2}{\mathrm{s}}$ was employed.

Convection was parameterized as an intensification of vertical diffusion; if the density profile was statically unstable, value of the vertical diffusivity κ_v was increased to $100\,\frac{\mathrm{m}^2}{\mathrm{s}}$.

The object of this thesis is, among other things, to compare the numerical solution for the idealized domain with a similar run with the topography of Late Permian. One interesting aspect here is that the continental configuration of the this time period resembles the square basin, with one large world ocean and a supercontinent spanning both the northern and southern hemispheres.

2.2.1 Solutions

All figures in this section are taken fom LaCasce and Gjermundsen [2017].

The surface velocities in the square basin run are generally eastward, except for a strong western boundary layer, and a slightly more intense eastward flow near the southern boundary -where $f = 0$. The flow along the western boundary turns south-eastwards at approximately 70°. The flow is eastward at the northern, and westward at the southern boundary, supplying the WBC.

Figure 2.3 shows the square basin surface velocities (2.3a), the zonal velocity in the middle of the basin (2.3b), and the meriditonal velocity v at 30° and 60° (2.3c).

The depth of the eastward flow increases with latitude, reaching 2000 meters depth at the northern boundary, while it is strictly seen in the surface layer south of 40°. At 20° the surface flow is westward.

The meridional velocity field is dominated by the WBC which reaches depths of 1000 meters at both 60° and 30°. Under the WBC there's a southward flowing return current, which makes the structure at the western boundary resemble the first baroclinic mode, the velocity crossing zero at $1000\,\mathrm{m}$. The WBC is notably narrower at 30° than at 60°, as seen on Figure 2.3c.

The widening of the WBC could be attested to the change in f. It was found that the width of the WBC scaled as $\frac{\nu}{\beta^{1/3}}$, indicating a Munk layer in the WBL.

Below the eastward flow at the northern wall, there is a strong westward flowing current. The structure of the flow at the northern boundary strongly resembles the WBC, showing the same two-layer structure. This suggests that the flow along the northern boundary is fed by the WBC.

The EBC displays a barolinic structure, with a northwards surface flow, and a southward flow beneath. The EBC is stronger at 60° than at 30°, which suggests that the flow is fed by the eastward interior flow.

Analyzing the depth integrated vertical velocity w (not shown here), it is seen that the square basin run produces a vigorous UW in the western boundary layer in a band

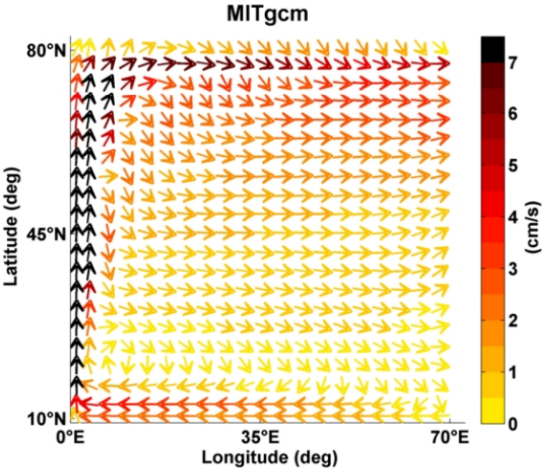

(A) Results from LaCasce and Gjermundsen [2017], showing the surface velocity field for the square basin run with MITgcm.

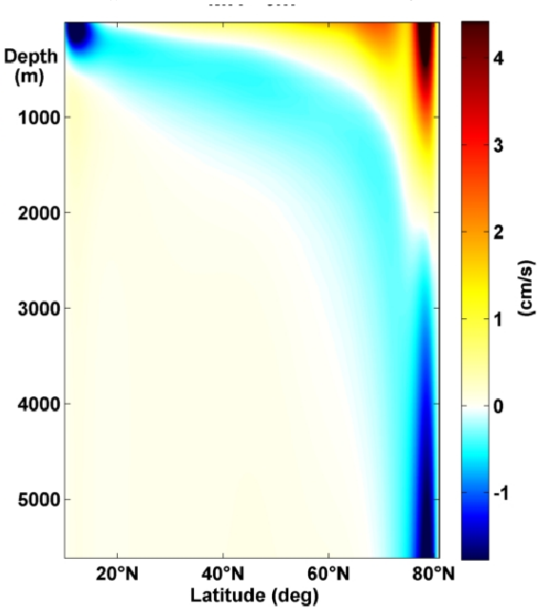

(B) Results from LaCasce and Gjermundsen [2017], showing u-variations with depth in the middle of the basin for the square basin run with MITgcm.

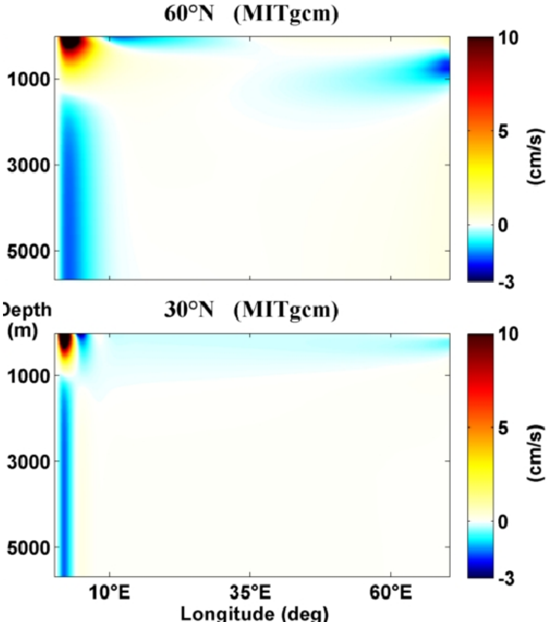

which widens with latitude. In most of the interior of the basin a weak, uniform UW is observed. LaCasce and Gjermundsen [2017] investigated the strength of the DW in the interior recirculation region versus the UW at the western boundary, and concluded that the DW in the interior is not sufficient to balance the UW in the west. Hence the western boundary layer is a significant source of deep water in the model run. In the NE corner both areas of depth-integrated UW and DW are seen, together with a wavy pattern which signifies convection. There's a major DW site in the NE corner, where $\sim 30\,\mathrm{Sv}$ sinks. Omitting the western boundary layer, the similarities between this model run and the Stommel-Arons model described in Section 2.1.3 is worth noting. Strong vertical velocities are also observed in the no-slip layers at the northern and southern boundary, as well as in the EBL. The UW in the EBL could also account for some of the increase in mass transport in the EBC with latitude.

The zonal stratification (expressed in terms of potential temperature, not shown here) is fairly unchanging from the southern boundary to around 70°, where the adiabats start sloping significantly. θ is fairly constant with depth at 80° and northwards. These highly mixed areas indicate where convection is present.

[LaCasce and Gjermundsen, 2017] noted that simulations with realistic topography should be carried out in order to further investigate the importance of the presence of a continental slope, mid-ocean ridges etc. It has been shown that a sloping bottom near the WBC can influence the flow [Park and Bryan, 2001]. Moreover, today the Equatorial region is an important site for UW, and LaCasce and Gjermundsen [2017]'s simulation does not portray a realistic Equator, with the southern wall and a no-slip condition.

2.3 Topographic Effects

A major difference between the Late Permian run and the square basin run lies in the lack of bathymetry in the latter. Topography has the potential to impact the flow in the following ways, through topographic steering, and by enhancing turbulent diapycnal mixing (Gille et al. [2004], Ledwell et al. [2000]). Additionally, the addition of slopes along the continental borders has the potential to change the modal structure of the flow [Winton, 1997].

We will focus on the latter, as topographic steering is a phenomena mostly observed in areas of weakly or non-stratified flows, though some effects remain in situations where the first baroclinic mode dominates.

Some authors have investigated the effect a sloping bottom has on the WBC (Park and Bryan [2001], Winton [1997] and others). Assuming that Sverdrup relation is valid, and integrating it in the vertical from the bottom to the surface of the ocean, the result is

$$\int_{-H}^{0} \beta v \, \mathrm{d}z = \int_{-H}^{0} f \frac{\mathrm{d}w}{\mathrm{d}z} \, \mathrm{d}z = f(w(0) - w(-H)). \tag{2.20}$$

$w_{-H} = \vec{u} \cdot \nabla h$, where $\vec{u}$ is the horizontal velocity, and h is the topography. At the eastern boundary we can take $h = h_0 x$ to resemble a continental slope, assuming that $h \ll H$. This yields

$$\beta v_0 = -f u_{-H} h_0 x. \tag{2.21}$$

What (2.21) tells us is that the flow has a barotropic, *southhwards* flowing component over an eastward-tilting slope. For a bowl-type topography, where a continental slope in the northern and southern boundaries as well as along the western side of the basin, this can influence the flow in the polar boundary layers as well by impose a barotropic component along topography. Vallis and Maltrud [1993] investigated among other things, how and where jets and mean flows are generated over topography for a $\beta-$plane approximation. Their results point to formations of zonal flows, and that exceptionally persistent zonal jets can form in barotropic flows. In relation to Vallis and Maltrud [1993]'s result on zonal jets, it's worth mentioning that if the topography is weak, such that the local bottom conditions are flat (i.e. $w_{-H} = 0$), (2.20) leads to a non-existing barotropic mode, while a sloping bottom does not forbore a barotropic component.

Results from Wunsch [1997] imply that the distribution of energy in different vertical modes depends on both latitude, bottom roughness and topography. Generally, their result showed that roughly half of the energy was retained in the barotropic, and half in the first baroclinic mode.

de La Lama et al. [2016], conducted - on the basis of Wunsch [1997] - a study based on satellite data and 81 globally distributed current meters. They found that the dominant mode in the ocean was the first baroclinic surface mode, which appear like the traditional first mode, only with horizontal velocities $\to 0$ at the bottom. This mode strongly resembles a combination of the first baroclinic and the barotropic modes. LaCasce [2017] found that the dominance of the first baroclinic surface mode was clear in areas with modest topography and bottom friction. He found that the surface mode dominates in areas where the slope of the topography is $> 10^{-5}$, regardless of bottom friction. This applies to most of today's ocean. However, energy cannot be transferred down the turbulent cascade if only the surface mode is present, as it is unaffected by friction. The addition of a *topographic* mode near topography can account for energy dissipation. Hence the apparent existence of a barotropic mode can be explained in terms of a surface baroclinic mode and a topographic mode.

2.4 On the Choice of Parameters

The diapycnal diffusivity (κ_v) is typically set to to $10^{-4}\,\mathrm{m}^2/\mathrm{s}$ in accordance with several studies on the MOC (cf. Munk and Wunsch [1998], Waterhouse et al. [2014]). Munk and Wunsch [1998] stated that this value was required to maintain the abyssal stratification against a global UW of $\sim 25\,\mathrm{SV}$, in accordance with Ledwell et al. [1993]'s measurements in the Pacific Ocean. This volume of UW is close to today's situation, and can form a basis for the Late Permian Period as well. Ledwell et al. [1993]'s result also show that most heat transport into the thermocline occur along density lines, rather than through diapcynal diffusivity.

Measurements carried out in Pelagic zones has confirmed a diffusivity of $10^{-5}\,\mathrm{m}^2/\mathrm{s}$ away from topography and boundaries. However, Munk and Wunsch [1998] argued that the global average κ_v is closer to $10^{-4}\,\mathrm{m}^2/\mathrm{s}$. Mixing across isopycnals require energy, which must be supplied though mixing mechanisms, as discussed in section 2.1.4.

The horizontal diffusivity κ_h is much higher than the vertical or diapycnal diffusivity, and is often set to $\sim 10^3\,\mathrm{m}^2/\mathrm{s}$ [Sallée et al., 2008].

The eddy viscosity K is related to the mean velocity gradient, in a way that the turbulent transfer of momentum through eddies can be parameterized in terms of the velocity. K is generally larger than κ, and is usually set to $\sim 1\,\mathrm{m}^2/\mathrm{s}$.

Chapter 3

Model Description: MITgcm

Information taken form mitgcm.org and correspondence with Liv Denstad.

As LaCasce and Gjermundsen [2017] did, MITgcm (Massachusetts Institute of Technology General Circulation Model) was used to simulate the global ocean circulation for a continental configuration from 252 million years ago. The simulation was run by Liv Denstad in 2014 (UiO, MetOs), and the results analyzed at present (2016). MITgcm is under constant development, so the present version may differ from from the 2014 version when the data was produced. The documentation can be reviewed at `http://mitgcm.org/public/r2_manual/latest/online_documents/manual.pdf`.

3.1 Model Resolution and Time-Stepping

The horizontal resolution for the Late Permian run is coarser than that of the square basin from LaCasce and Gjermundsen [2017], with a $2^\circ \times 2^\circ$ spherical polar grid (see figure 3.1), spanning the range of latitudes between -84° and 84°. A wall was added at $\pm 84^\circ$ in addition to the bathymetry. The depth (employed as height in the model) is resolved through 24 vertical layers, their depth spanning from 15 meters at the surface to 950 meters in the deep ocean. The thickness of the vertical layers is seen in Appendix C.

A partial cell capacity is implemented in the model, allowing the bottom cells to adjust to the bathymetry, i.e. the actual thickness of a cell at a certain point on the $xy-$grid is adapted to the bathymetry at that certain point. The bathymetry is shown in figure 3.2.

The time step is set to 1800 seconds for both the tracer and momentum equations. Staggered baroclinic time-stepping (Adams-Bashforth) is applied for the thermodynamic fields. This means that the calculations of the thermodynamic fields are delayed for

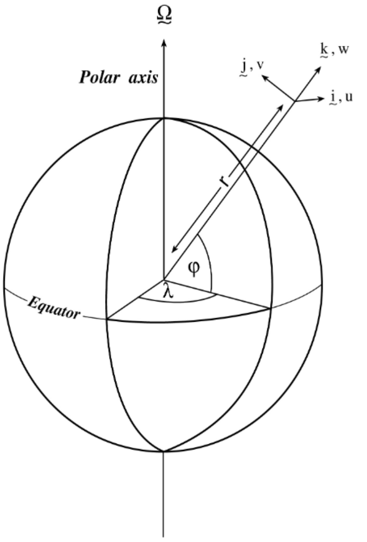

FIGURE 3.1: MITgcm spherical polar coordinates. longitude λ, latitude ϕ, and r the distance from Earth's center.

half a time step, allowing for use of the updated flow field to calculate the advective terms. Essentially, this makes it so that the gravity wave terms can leap-frog in time (and thus conserve their energy), yielding higher accuracy and stability. This is recommended for well-stratified problems.

The algorithm used for stepping forward is employed on the basis of preserving non-divergent flow, readily done by employing a C-grid staggered in space. For better conservation of mass, the zonal (u) (meridional (v)) components are calculated in such a way that the zonal(meridional) velocities fall on the interface between continuity cells in the zonal(meridional) cell face, see Figure 3.3.

By scaling the general diffusion equation

$$\frac{\partial \Psi}{\partial t} = \kappa \nabla^2 \Psi, \tag{3.1}$$

where Ψ is some tracer and κ is the diffusivity, it is seen that the diffusive time scale is given by $\tau_z \sim \frac{D^2}{}$. κ_v - the vertical diffusivity, is set to $10^{-4} \frac{\mathrm{m}^2}{\mathrm{s}}$. Inserting $D = 5000\,\mathrm{m}$ as a typical depth scale in the global ocean yields $\tau_z \simeq 1800\,\mathrm{years}$.

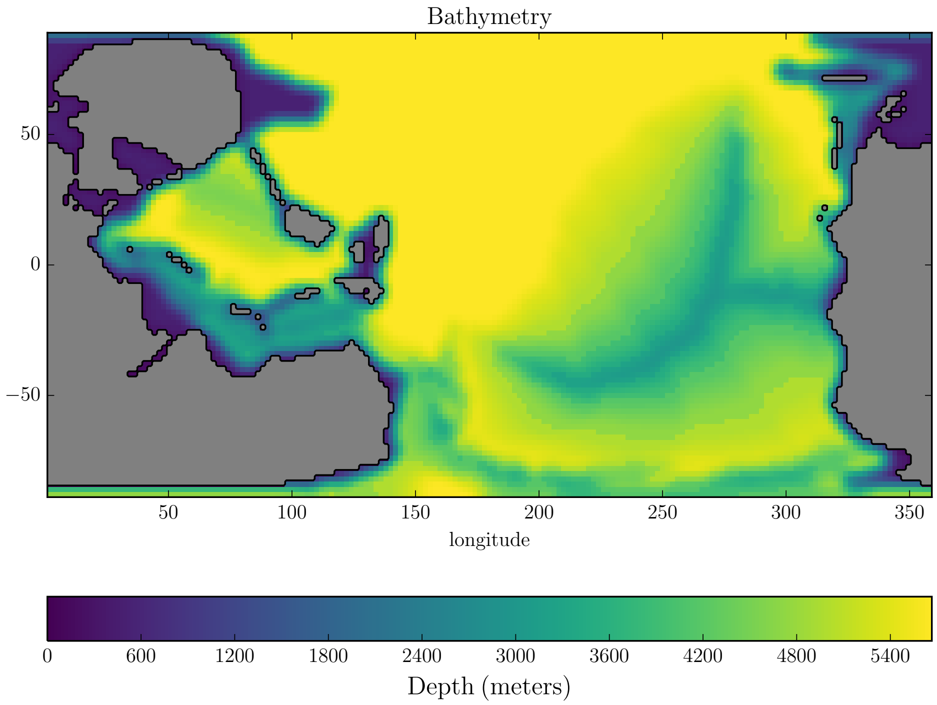
Bathymetry
50
0
−50
50
100
150
200
250
300
350
longitude
0
600
1200
1800
2400
3000
3600
4200
4800
5400
Depth (meters)

FIGURE 3.2: MITgcm Model bathymetry.

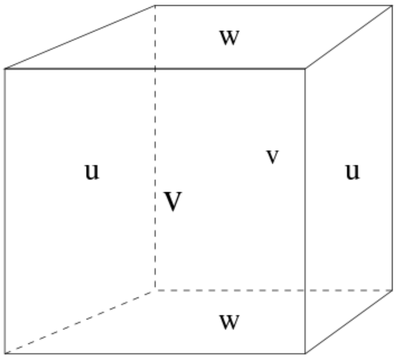

FIGURE 3.3: Three-dimensional staggering of velocity components.

The advective time scale is $\tau_{\text{adv}} \sim \frac{L}{U}$, where L and U are scaling variables for domain in the $xy-$direction and horizontal velocities. This yields $\tau_{adv} \sim \frac{10^7\,\text{m}}{0.5\,\text{cms}^{-1}} = 2 \times 10^9\text{s} \simeq$ 60 years.

The time scales give a general estimate of the time a system governed by either takes to reach equilibrium, and thus gives an estimate of the spin-up time of the model. They are therefore a good estimate of the spin-up time of the model.

In this case the model was spun for 2000 years before reaching equilibrium. In the results, the average values of the last 300 years of the simulation is used to even out small fluctuations and grant a better picture of the overall circulation.

3.2 Model Equations and Parameters

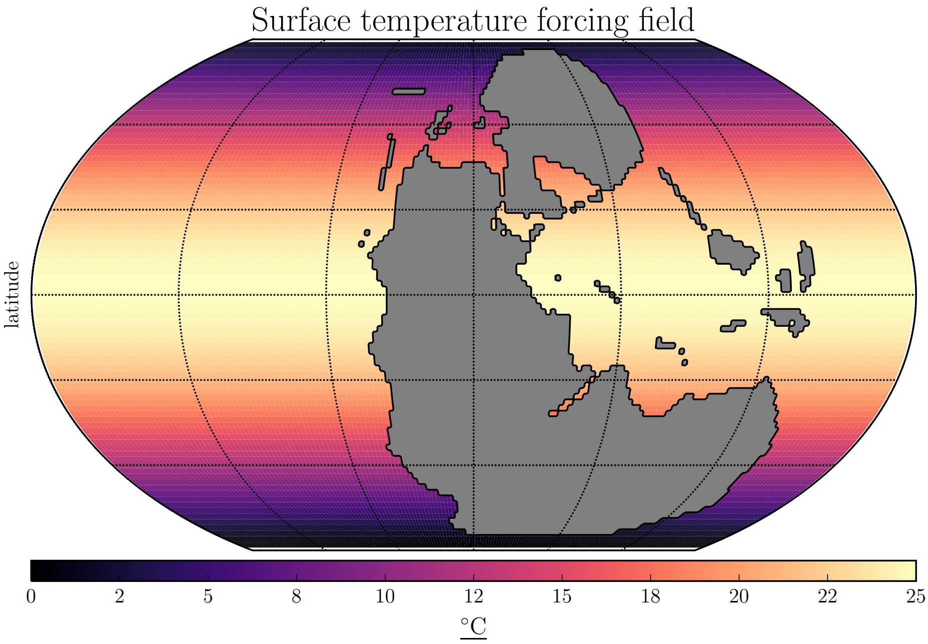

FIGURE 3.4: Temperature forcing field $\mathcal{F}_\theta$ shown in °C.

In this study, we focus on the buoyancy driven circulation. In order to separate the buoyant effects from atmospheric effects, no wind field was implemented in the model. Additionally, the salinity effects were neglected, as the salinity was set to a constant equal $35\,\mathrm{psu}$.

The surface temperature forcing is parameterized by relaxation to a specified temperature field [Vallis, 2006]. It is given by

$$\mathcal{F}_\theta = C_\theta(\theta^* - \theta), \tag{3.2}$$

where $\mathcal{F}_\theta$ is the temperature forcing, and C_θ is a constant specified by the relaxation time, which was set to 1 month. θ^* is the relaxation temperature for a given longitude and latitude. The effects of seasonality was neglected, and thus the temperature forcing field does not change in time. The relaxation temperature field, $\mathcal{F}_\theta$, is seen in Figure 3.4.

The horizontal momentum equation solved is

$$\frac{D\vec{u}_H}{dt} + (2\vec{\Omega} \times \vec{u})_H + \nabla_H \Phi = \mathcal{F}_{V_H}, \tag{3.3}$$

where Ω is the rotation rate of the Earth, Φ is the pressure term given by $\Phi = \frac{P}{\rho_c}$, and $\mathcal{F}_{V_H}$ is the forcing and dissipation term. The parameterization of $\mathcal{F}_{V_H}$ varies according to grid size, and external forcing. In this case,

$$\mathcal{F}_{V_H} = \nabla_H \cdot A_h \nabla_H \vec{u} + \frac{\partial}{\partial z} A_z \frac{\partial \vec{v}}{\partial z}, \tag{3.4}$$

where a horizontal Laplacian operator ∇^2 is used to parameterize viscous dissipation. A_H and A_z are the horizontal and vertical Laplacian turbulent eddy viscosity coefficients. They are generally larger than the molecular viscosity coefficients K_z and K_h. The viscous processes that occur on sub-grid scales are contained in the eddy viscosity coefficients, also represented by a Laplacian operator.

The temperature equation is given by

$$\frac{D\theta}{dt} - \nabla_h \cdot K_h \nabla_h \theta - \frac{\partial}{\partial z} K_z \frac{\partial \theta}{\partial z} = \begin{cases} \mathcal{F}_\theta, & \text{surface.} \\ 0, & \text{otherwise.} \end{cases}$$

(3.5)

where θ is the potential temperature, and K is the thermal diffusivity. K is related to the mean velocity gradient, in a way that the turbulent transfer of heat through eddies can be parameterized in terms of the mean gradient. The vertical diffusivity is approximated to the diapycnal diffusivity (K_z), which was set to $10^{-4}\,\frac{\mathrm{m}^2}{\mathrm{s}}$. The mixing is in part due to tidal forces, and partly due to wind stress. So in a way mixing by winds is implemented in the model.

The horizontal diffusivity K_h was set to $500\,\frac{\mathrm{m}^2}{\mathrm{s}}$, which is the same order of magnitude as LaCasce and Gjermundsen [2017] used. The model is hydrostatic, and thus mass overturning can not occur. However, in cases of static instability (represented by a convective adjustment index), mixing is applied by increasing the vertical diffusivity K_z to $100\frac{\mathrm{m}^2}{\mathrm{s}}$. This results in a rapid mixing of buoyancy in the vertical.

The RHS of (3.5) demonstrates that only through the ocean surface can external heat exchange occur.

Initially, the ocean was at rest, such that the initial velocities were set to zero before the spin-up. A no slip-condition was employed for the ocean walls (the continental borders) and the bottom; $\vec{u} \cdot \hat{n} = 0$, where $\hat{n}$ is the normal unit vector of the borders.

3.2.1 Gent-McWilliams/Redi parameterization

In dynamically active areas, as the WBL, with sloping isopycnals and in promixty to topography, it can be shown that the vertical velocity is highly sensitive to the adiabatic and the cross-isopycnal mixing. In a coarsely resolved run, both mixing terms are parameterized in terms of the Gent-McWilliams/Redi parameterization. We have the following equation (in steady state):

$$\vec{u} \cdot \nabla T = \bar{w}\frac{\partial \bar{T}}{\partial z} + \nabla\overline{\vec{u}T} - \frac{\partial}{\partial z}\kappa\frac{\partial \bar{T}}{\partial z}. \tag{3.6}$$

Equation (3.6) tells how the mixing of temperature occur. The second term on the RHS denotes the horizontal mixing, the last term on the RHS the vertical mixing. Both of these terms are parameterized in the model. The GMR scheme shifts the horizontal mixing so that it occurs adiabatically, and the vertical mixing across isopycnals. Thus it can be a source of artificial vertical velocities, w, as w is directly dependent on the mixing (seen in (3.6)).

However, while the GMR scheme is a source of some errors it also reduces the U- and DW associated with Veronis effect, an abnormally large offshore downwelling and compensating UW in the WBL, often observed in OGCM's at midlatitudes. These features are a result of diffusion of mass across the sloping isopycnals in the deep WBC, or the return current.

The GM part of the scheme reduce this artificial vertical mass transport by *not* parameterizing the effects of mesoscale eddies in terms of diffusion, as the GM-scheme works by adiabatically re-arranging tracers through an advective flux where the advecting flow is a function of the slope of the isentropic surfaces [MIT, 2006].

Hence the GM parameterization flattens the density front in the WBL associated with the strong poleward current by advecting warm and cold water across the boundary associated with the WBC.

As Lazar et al. [1999] stated: *'The advection near the boundary tends to lower isopycnals, while upward induced advection tends to raise them offshore. In order to maintain a stationary equilibrium, the Eulerian-mean currents have to counteract this vertical movement by forming an opposite WBL UW and interior DW system.'*

In other words, the GMR-scheme promotes UW in the WBL, and DW just offshore.

The Redi-part of the scheme mixes tracers along the local isentropic surface through diffusion.

3.2.2 Boundary Layer Mechanisms

In the WBL, the forces governing the flow is complex, but the equation can be approximated to

$$v\frac{\partial b}{\partial y} + w\frac{\partial b}{\partial z} = \kappa_h \frac{\partial^2 b}{\partial x^2}. \tag{3.7}$$

The equation is taken from LaCasce and Gjermundsen [2017]. The RHS is a representation of the lateral mixing. The dominating term in on the LHS in (3.7) is the vertical advection, which is positive near the boundary, where $w > 0$. The first term on the RHS - the meridional advection is *negative* near the boundary, where $v > 0$ and $\frac{\partial b}{\partial y} < 0$ in the NH. The signs are reversed in the SH.

Utilizing the fact that the lateral mixing term follows the thermal wind (through geostrophic adjustment), the sign of lateral mixing term can be derived. It is calculated to be positive near the boundary, and negative offshore in the WBL, where $\frac{\partial v}{\partial x} < 0$.

The WBL is however a highly active location, and due to parameterizations of sub-grid processes in this area, the results, while quantitatively good, can partly be a result of rough parameterization.

Chapter 4

Model results: The Ocean Circulation in the Late Permian

4.1 The General Circulation Pattern

In this section, the horizontal velocity field will be described. Figure 4.1 shows the horizontal velocity field at the surface (4.1a), at $z = 870\,\mathrm{m}$ (4.1b), at $z = 2250\,\mathrm{m}$ (4.1c), and at $z = 3920\,\mathrm{m}$ (4.1d), together with the temperature fields at the respective depths.

4.1.1 The Surface Velocity Field

The surface velocity field is seen on Figure 4.1a.

As in the square basin model run, the surface velocities in the interior mid-latitudes of the Panthalassic Ocean away from the Equator are primarily zonal and eastward, with velocities in the range of a few $\mathrm{mm/s}$ to some $\mathrm{cm/s}$. It is in thermal wind balance with the zonal temperature gradient.

In the Tropics the surface velocities are of the same order of magnitude, but turned westward. The zonal flow in the Tropics increases from west to east, which could indicate UW along the Equator in upper layers.

The WBC dominates the velocity field, and at the surface (4.1a) the flow is initiated in the Paleo-Tethys Sea, flowing along the eastern coast of Pangea before entering the Panthalassic Ocean through the strait separating the continent from the islands of South and North China. Here it merges with the weaker branch of the WBC flowing along the eastern shore of North and South China. At roughly $50^\circ\,\mathrm{N}$ the WBC flow veers eastwards, and turns towards the Equator in both hemispheres. This reversal of v could influence the vertical velocity field through the Sverdrup balance (Equation (2.14)). A change in the sign of has a direct impact on w, as long as (2.14) holds. It was tested and confirmed that the relation stands everywhere except in the vicinity of the Equator, the western and the polar boundary layers. This will be investigated further in Section 4.1.4. Hitting the wall at $\pm 84°$, the WBC flow is turned eastward, flowing along the polar boundaries towards the western shore of Pangea. However, in the NH the flow turns westward before hitting the continental shelf in the NE of the Pathalassic (see Figure 3.2 for location of the continental shelf). Thus the mass transport into the NE part of the basin is reduced. This feature sets this model run apart from the square basin case. This turning does not occur in the SH, where the surface flow along the polar border is strictly eastward.

The sluggish eastward flow in the interior turns polewards as it encounters the western shore of Pangea, and the velocities increase somewhat, but not close to the speed of the WBCs. In the SH, the EBC flow veers westward, merging with water masses originating from the WBC at high latitudes. The northern EBC encounters the islands off the shore of North America. Here its relatively warm water joins with the cold water from the northern WBC.

The surface WBC is divided into two components, one weak component in the Panthalassic, and the main branch in the Paleo-Tethys Sea. This main branch is fed by the westward interior flow at low latitudes. In the Tropics, the westward flow is topographically steered around North and South China and into the Paleo-Tethys sea, feeding the WBC in both hemispheres.

4.1.2 The Intermediate/Deep Velocity Field

Figure 4.1b shows the horizontal velocity field at 870 meters. The most striking difference between the surface flow and this intermediate flow is that the interior velocities' direction are reversed, now being westward. This indicates baroclinic interior flow. The direction of the flow is also reversed in the EBL, as the flow is equatorwards at this depth. This interior eastward flow is warmer than both the tropical water, and water located at higher latitudes. This indicates DW in the interior, and UW in the Tropics. In the WBLs, the flow has a deeper structure, and its characteristics are the same as at the surface.

In the NH, the WBC still displays the dual structure, being divided between the Panthalassic Ocean and Paleo-Tethys Sea, but at this depth most of the mass transported into the polar areas originates from the Panthalassic. Additionally, the NH WBC is clearly influenced by the topography. At the polar boundaries the flow is much deeper than in the interior, and shows the same characteristics as at the surface, similar to the WBC.

Figure 4.1c shows the horizontal velocity field at 2250 meters. At this depth the flow is vastly different than at 870 meters and at the surface. The WBL displays a baroclinic quality, as the WBCs flow equatorwards. At the depths were the sign of v is reversed, the flow reaches velocities up to several $\mathrm{cm/s}$ in both hemispheres. Some of this return flow enters the Paleo-Tethys Sea through the shallow straits separating the two oceans, but most of the WBC return flow is confined to the Panthalassic, resulting in a fairly weak coupling between the the Panthalassic Ocean and the Paleo-Tethys Sea at this depth. The WBC turns eastward in the Tropics. The interior flow is westward in both hemispheres, but the flow in the SH is clearly affected by the topography seen in Figure 3.2, showing a gyre-like structure offshore of South America. The eastward flow in the Tropics loses momentum from west to east, particularly east of $250°$ E, which indicates that the layer loses mass, either via UW or DW when closing up on Pangea. At the northern boundary, the flow is quite strong and mainly flowing westward, though in the NE corner southwards flow is observed together with a pool of water much warmer than its surroundings. The flow at the southern boundary looks more chaotic, but here as well the eastern warm pool is observed, along with high velocities. Here the direction is westward, though with an equatorwards component.

Lastly, Figure 4.1d shows the velocity field field at 3920 meters depth. In the Tropics the velocities are still eastward, but clearly topographically steered around the mid-ocean ridge. At midlatitudes in the NH the velocities are small and westward, while the flow in the SH is heavily influenced by the topography. The cyclonic gyre south of the ridge is seen through the alternating sign of v around $250°$ and $300°$E. South of the mid-ocean ridge water is steered westward and northward before veering westward into the WBL. The WBC's are the most predominant feature, flowing equatorwards in both hemispheres. At this depth, the Paleo-Tethys Sea is almost completely cut off from the Panthalassic Ocean, except for a small inflow of water in the WBL in the NH. At the polar boundaries the flow is primary eastward, though in the SH the flow is stronger, and more locally influenced by the topography. A warm pool is observed in both the SE and NE corner. Here the warmest water in the basin is located, at almost $8°\mathrm{C}$, compared with a $7°\mathrm{C}$ water in the interior of the basin in the NH. This might be related to the rate of DW in these areas. This issue will be examined in section 4.1.4.

The topography in the SH steers the currents in their redistribution of heat, making the water south of the ridge warmer than the equivalent latitude and depth in the NH.

Figure 4.3 shows the variations in the meridional velocity (v) with depth for 60°N (4.3a) and 30°N (4.3b). The locations of the cross sections are seen on Figure 4.2. A WBC is clearly seen in both latitudes, though at 30° N a northward flowing current is seen both in the Paleo-Tethys sea and in the Panthalassic. The northwards flow expands down to approximately $1500\,\mathrm{m}$ depth. Below the WBC the southward return flow is seen. The return flow reaches the bottom, but the velocities are clearly smaller than for the surface WBC, where the velocities are of order of $10\,\mathrm{cm/s}$. This is approximately 10 times the velocities in the return flow. At 60° N the WBC velocities are slightly stronger than at 30° N, but it spans only the upper $1000\,\mathrm{m}$, making it shallower than at 30° N, though in addition, it is also somewhat wider. At 60° N the WBC covers the enire continental shelf.

At the eastern boundary, the situation looks quite different than in the west. At 30° N a weak southwards flowing EBC is observed below the surface, its velocities around $1\,\mathrm{cm/s}$. The EBC is noticeably wider than the WBC. At both 30° N and 60° N a southward flowing EBC is seen below the poleward flowing surface EBC, and the flow changes directions at $200\,\mathrm{m}$ and $1000\,\mathrm{m}$ depth at 30° N and 60° N respectively.

The meridional velocities in the interior are insignificant compared to the boundary currents and the flow at the polar boundaries. Though overall the transport in the interior is equatorwards.

An important distinction between the Late Permian run, the square basin run and the theoretical models described in Section 2, is the existence of an Equator where water can be exchanged between the hemispheres in the Late Permian case. In the square basin run the Equator is represented by a wall. However, the flow is very similar in the two cases. The UW is more intense at the Equator in the square basin case, but it's qualitatively the same otherwise (i.e. westward surface flow, increasing in strength to the west).

In the Late Permian case, the meridional transport across the Equator is weak, separating the northern and the southern hemispheres to a certain degree. Though at the western boundary in both the Panthalassic and the Paleo-Tethys Sea, some mass transport past the Equator is seen, though mostly caused by topographic steering around North and South China.

Figure 4.4 shows the meridional velocity with depth at latitudes 60°S (4.4a) and 22°S (4.4b). The location of the section is seen oi Figure 4.2. As in the NH, the most dominant feature is the southwards WBC, with velocities exceeding $10\,\mathrm{cm/s}$, and an equatorial return flow stretching from 1500 meters depth to the bottom, giving the WBL a clear baroclinic character.

At $22°$S, the cylonic gyre observed close to the mid-ocean ridge in the SH is also observed between $250°$E and $300°$E, with velocities of the order $\sim 1\,\mathrm{cm/s}$. A portion of the surface WBC is observed in the Paleo-Tethys Sea, though the deep return flow is completely confined to the Panthalassic. A striking feature of this section is how the entire WBL is affected and steered by the topography. Even the surface WBC in the Panthalassic follows the contours of the topography. It has been shown that the topography can affect the flow throughout the water column in baroclinic cases where the first mode dominates [Hurlburt and Thompson, 1981]. Moreover, a strong southwards flow is observed just east of the WBC with a northwards flow beneath.

At $60°$S, the WBCs baroclinic structure remains the same, and the northwards surface flow just east of the WBL is also observed. Also, the subsurface gyre south of the mid-ocean ridge is observed through alternating directions in v around $\sim 250 - 300°\,$S. A southwards flowing surface current and an equatorwards subsurface current is observed in the EBL, though the velocities are small compared to the WBL.

Figure 4.5 shows a cross section of the zonal velocity, u taken in the middle of the Panthalassic Ocean (220° E, indicated by the vertical line in Figure 4.1). We see that the westward flow at low latitudes is part of a wide westward flowing belt, that develops into a subsurface flow with higher latitudes. The depth of the surface flow is related to the depth of the thermocline δ, which is shown to vary with $\delta \sim f^{\frac{2}{3}}$ for a case that applies the steady state planetary geostrophic equations, without wind forcing [Vallis, 2006]. This fits well with Figure 4.5. Above the westward flow, poleward of $\pm 20°$, the flow is eastward and gradually becomes deeper with higher latitudes, and extends to the bottom at approximately $\pm 70°$. At $\pm 80°$ it reaches its maximum velocity of roughly $10\,\mathrm{cm/s}$. A strong westward flow is observed below this eastward flow, with velocities of around $0.1\,\mathrm{cm/s}$. At these latitudes, in the NH, in particular, u alternates between positive and negative values. The velocity reaches up to $2.5\,\mathrm{cm/s}$ in both directions. The zonal flow in the NH and the SH boundary layers deviates from the results of LaCasce and Gjermundsen [2017]'s square basin run. The strong westward flow observed along both boundaries displays an apparent *barotropic* quality, which the square basin run did not.

This barotopicity can be due to the existence of a continental slope along the polar boundaries, cf. Section 2.3. The flow just equatorwards of the westward flow along the boundaries displays a more baroclinic structure.

The distinctive westward surface jet observed close to the Equator in the square basin run is not observed to the same extent in the Late Permian case. While the surface flow is westward in both cases, in the Late Permian run, the tropical surface velocities

velocities are not distinctively greater than in the subsurface interior flow. Additionally, beneath the sluggish, eastward flow in the tropical interior of the basin, a westward bottom flow is observed. This feature is completely absent in the square basin case, and could indicate that more energy is retained in the second and third baroclinic modes at low latitudes for Late Permian case than in the square basin case.

Nevertheless, which mode that dominates would depend on the latitude and the stratification. As stated in Section 2.3, Wunsch [1997] showed that the barotropic and first baroclinic modes more or less dominate in midlatitudes. Newer results [de La Lama et al., 2016] suggest that the vertical structure of a flow that *seems* to be dominated by the barotropic and the first baroclinic modes, is really dominated by the first surface mode. LaCasce [2017] stated that this combination of modes holds true for most of today's ocean. The bathymetry used in this study, however, include locations with no topography what so ever, particularly in the NH - see Figure 3.2.

Figure 4.6a shows the zonal velocity (u) for some chosen latitudes at longitude 220° E, located in the center of the Panthalassic Ocean. The dashed lines indicate zero-crossings, i.e. where the flow changes direction. Figure 4.6b shows the calculated Brunt-Väisälä frequency for the localities in Figure 4.6a. The locations were chosen due to their location in the middle of the Panthalassic, and due to the absence of significant bottom topography in these areas. However, a slight, mainly meridional topographic slope is present at 3° N and 45° N (see Figures 3.2 and 4.6a).

Following the argument in section 2.3 we would expect the areas to be seemingly dominated by the first or second baroclinic modes, as the absence of bottom topagraphy would inhibit energy from gahtering in the barotropic mode [Winton, 1997].

Studying the sections and comparing them to the work done by LaCasce [2012] it is apparent that some of the kinetic energy in the flow is retained in the first and second baroclinic surface modes for all latitudes displayed in Figure 4.6a. The second baroclinic surface mode seems to dominate in the Tropics.

At mid-latitudes (45° N), the first baroclinic mode surface is more predominant than in the Tropics and at high latitudes, while the second mode is more noticeable at 80° N.

Without thoroughly analyzing the result shown in Figures 4.6a and 4.6b it is futile to draw clear conclusions on whether the surface mode or the classical mode is what dominates the vertical velocity profiles. Though following the arguments LaCasce [2017] made on the effects a rough bottom, and a slight topography can have, it is plausible that the first and second surface modes is what dominates the flow, with the addition of topographic waves to resolve energy dissipation.

4.1.3 Meridional Mass Transport

Latitude/location	Mass transport [Sv]
$-60°$/Surface	-39.6
$-60°$/Return current	27.6
$-30°$/Surface	-45.3
$-30°$/Return current	29.1
$30°$/Surface	35.0
$30°$/Return current	-25.3
$60°$/Surface	24.4
$60°$/Return current	-30.8

TABLE 4.1: Meridional mass transport in the WBL given in Sverdrups ($1\,\mathrm{Sv} = 10^6\,\frac{\mathrm{m}^3}{\mathrm{s}}$) for selected latitudes. Negative figures refer to southwards, positive numbers to northwards transport. The Return current is the equatorward flowing flow beneath the surface WBC.

Table 4.1 shows the total poleward mass transport in the surface WBC, and the total mass transport in the return current beneath the surface WBC for a range of latitudes. The poleward mass transport in the WBC in the NH is calculated to be 35 Sv at $30°\,\mathrm{N}$ and 24 Sv at $60°\,\mathrm{N}$, hence the mass transport in the western boundary layer decreases with increasing latitude. The same goes in the SH. It is seen that the strength of the WBC is generally slightly greater in the SH than in the NH, but that the return currents are of the same size in both hemispheres. The weaker poleward flow in the NH could be a result of the differing bathymetry in the two hemispheres (see Figure 3.2). In the NH midlatitudes a pronounced continental shelf could inhibit WBC flow, and reducing the total poleward mass transport through cross-sections. The shelf is approximately $750\,\mathrm{m}$ deep, and the main branch of the WBC is located on top of the shelf. While the SH, the WBC is not hindered by shallow topography. Here the WBC reaches depths of $1200\,\mathrm{m}$ at the equivalent latitude. Thus the WBC is generally broader and deeper in the SH than in the NH, which could bring about the difference in WBC mass transport between the hemispheres. The WBC transport is also affected by the extent and localities of DW areas.

This reduction in WBC transport with increasing latitude could be a consequence of of the eastward internal flow, which is supplied by the WBC, even while the WBC is constantly supplied with mass UW from the deep. Or a consequence of increased DW along the boundary. The rate of UW and DW in and in the vicinity of the the WBC will be estimated in section 4.1.4.

The situation in the EBL (not shown in Table 4.1) is quite different from the WBL. An EBC is observed both in the NH and in the SH, though the meridional mass transport is not close to that of the WBC. At ±30°, the surface EBC transport was below $1\,\mathrm{Sv}$, though the mass transport increases with increasing latitude in both hemispheres, reaching $3\,\mathrm{Sv}$ at $60^\circ\,\mathrm{S}$ and $9.6\,\mathrm{Sv}$ at $60^\circ\,\mathrm{N}$. The general increase in mass transport with latitude in the EBC is a consequence of the zonal mass transport in the interior, which constantly supplies the EBL, turning polewards as it encounters the western shore of Gondwana. The direction of the resulting meridional flow is a direct result o of the Sverdrup balance (Equation (2.14)). The EBL will be looked into in Chapter 5. The difference in strength of the EBC at $60^\circ\,\mathrm{S}$ and $60^\circ\,\mathrm{N}$ is possibly due to the dissimilar topography in the two hemispheres.

Figure 4.7 shows the stream function Φ given by

$$\Phi(y,z) = \int_{x_w}^{x_e} \int_{-H}^{-z} v\, dx dy, \tag{4.1}$$

where v is the meridional velocity, and x_e and x_w are the eastern and western boundaries of the basin at the given latitude (y). The stream function is a measure of the *total overturning circulation*, i.e. its magnitude reflects the total MOC. The MOC looks similar in the NH and SH when it comes to both total mass overturning and the depth of the convection, which spans to around $3000\,\mathrm{m}$ depth.

The most significant convection is seen at $\sim \pm 70^\circ$. The total DW is of the same order of magnitude as the total mass transport in the WBC. Hence it can be concluded that the majority of the poleward mass transport occurs in the WBL. The MOC seems to be divided into two cells at the northern boundary. This fature could be a result of the numerical representation of the polar boundary in the MITgcm, and may not be a genuine feature of the MOC.

Figure 4.7 implies a rather strong overturning, with $\sim 30\,\mathrm{Sv}$ transported in the surface layers in both hemispheres. This is of the same magnitude as the transport in the WBC. At ± 70° a strong overturning is seen, with approximately $60\,\mathrm{Sv}$ sinking in total.

The total mass transport is slightly less in the SH than in the NH, which might be a result of northwards topographic steering in the SH (see Figure 4.1d and 3.2), which results in a larger equatorwards mass transport, balancing the poleward WBC. However, it is insignificant compared to the WBC concerning the total poleward mass transport.

A symmetrical MOC is to be expected as the forcing is the same in both hemispheres, and the most significant DW occurs at approximately the same latitudes - as I will show in Section 4.1.4.

The stream function also indicates that the equatorial return flow in the deep ocean stretches over a greater depth than the poleward surface transport. The deep velocities are generally sluggish, but the vertical (and zonal) extent of the return flow are extensive compared to the surface flow. The UW generally occurs poleward of $\pm 20^{\circ}$.

Following Winton [1997], we would expect the MOC to be shallower in this case than in the square basin run, as the Late Permian simulation was conducted with sloping topography along most boundaries. However, when comparing Figure 4.7 to the overturning circulation for the square basin, it is clear that the Late Permian case shows just a slightly shallower overturning than the square basin scenario of LaCasce and Gjermundsen [2017]. On the other hand, the sloping sides of the bathymetry used by Winton [1997] stretched from high latitudes to approximately 50° N, which is much more extensive than the narrow continental shelves located at the polar boundaries in the Late Permian case. In Winton [1997]'s experiment, the topography effectively inhibits parts of the deep water formation.

4.1.4 The Vertical Velocity Field and Convection

Figure 4.8 shows the vertically integrated vertical velocity. Positive values indicate locations of UW, and negative values point to DW. A large UW area is seen west in the Panthalassic Ocean, along the eastern side of the islands of North and South China. Also, a region of significant DW is observed east of the WBC, as we would expect (See section 3.2.1). The western Paleo-Tethys Sea is also a site for UW, though it is less intensive than in the western Panthalassic Ocean. As in the square basin run, depth-averaged DW is observed in the Tropics.

Areas of depth-averaged, weak U- and DW are also seen in vicinity of the mid-ocean ridge (see Figure 3.2), along with a localized area of strong DW close to the north-south ridge, and an areas of UW south and west of the ridge. This region of UW and DW is, through the Sverdrup balance (Equation (2.14)) be related to the cyclonic gyre observed in the $uv-$field in this area - seen on Figure 4.1.

Around 60° in both hemispheres, the integrated vertical velocity starts shifting between positive and negative values, almost in a wave-like pattern. This pattern has been shown to be correlated with areas of convection [LaCasce and Gjermundsen, 2017].

the reason why the $w-$field has this appearance in the convective region can be explained by how convection is implemented in the model (explained in Section 3.2). The dominant balance in the interior is

$$\frac{\partial b}{\partial z} w = k_z \frac{\partial^2 b}{\partial z^2}, \tag{4.2}$$

where k_z is the diapycnal diffusivity. (4.2) states that the dominant forces in the interior is vertical advection and diffusion. It looks similar to the dominant balance in the WBL (equation (3.7)), but here the *vertical* mixing is more important than the horizontal, and the meridional advection of buoyancy is insignificant compared to the vertical. In areas where the convective adjustment index -a measure of when the water column becomes unstable- is > 0, k_z is increased by a factor of 10^6 to enhance mixing. As (4.2) shows, w would increase accordingly, hence resulting in the huge values of w in these areas. Additionally, artificially large values for w can develop along the basin walls in hydrostatic models as a result of basin geometry. Straight vertical walls, and calculating w from the continuity equation could lead to large vertical velocities along the basin boundaries.

Figure 4.9 shows the vertical velocity w at 790 meters (Figure 4.9a) and 2480 meters (Figure 4.9b) below the surface.

At 790 meters (Figure 4.9a) the most interesting region is the WBL. In the NH, strong UW is observed in the Paleo-Tethys Sea along the coast of Gondwana. UW is seen in the WBC branch in the Panthalassic Sea, but not to the same extent. In the SH, on the other hand, the majority of the WBL UW occurs in the Panthalassic Sea. The DW region just east of the WBL mentioned above is present in both hemispheres. A weak UW is seen along the Equator and in the EBL, whilst DW occurs in the NE, NW, SW, and SE corners.

At 2480 meters (Figure 4.9b) the WBL looks much the same as at 790 meters in the SH, though in the NH, the majority of the UW occurs in the Panthalassic rather than the Paleo-Tethys. DW is still observed in the basin corners, though to a lesser extent in the NE and SE. Weak UW is seen along the Equator. In addition, singular localities of up and DW is seen in the SH. These local effects appear due to the topography.

Integrating the Sverdrup balance (2.14) in the vertical to obtain w from the meridional velocity field yields

$$w(-z) = -\frac{\beta}{f} \int_{-z}^{0} v dz. \tag{4.3}$$

Hence the vertical velocity at a given depth $-z$ can be diagnosed though the integrated meridional velocity from that depth to the surface. Looking at the horizontal velocity field (Figure 4.1c) in the areas of the local U- and DW, the coupling between v and w can be explained in terms of (4.3). This applies to the DW region just offshore of the WBC, where v changes sign (Figure 4.1b), and the gyre-like structure in the SH just south of the mid-ocean ridge. The validity of the Sverdrup relation was tested and confirmed for both of these areas.

At 430 meters depth (not shown) the UW into the WBL equals $12\,\mathrm{Sv}$ in the SH, and $9\,\mathrm{Sv}$ in the NH, $7\,\mathrm{Sv}$ in the Paleo-Tethys Sea, and $2\,\mathrm{SV}$ in the Panthalassic. The rate of UW into the WBC displays that approximate magnitude, which is greatest between 900 and 2000 meters depth in the Panthalassic. The WBC UW in the Paleo-Tethys Sea ensues at shallower depths, between 100 and 1000 meters below the surface.

Results by Schloesser et al. [2012] indicate that UW occurs in the WBL in model studies like this as a result of horizontal diffusion of mass across the sloping isopycnals in the boundary layer. The tilting $\rho-$field is linked to the geostrophic adjustment occurring in the WBL. However, it has been argued that UW into the WBL is a true feature of the ocean circulation, and not attributed to Veronis effect alone (LaCasce and Gjermundsen [2017] and references therein). The magnitude of the UW depends on the topography in the area and the strength of the WBC, i.e. the slope of the isopycnals, as the meridional flow in the WBL is in geostrophic balance.

Around the Equator (between $15°$ S and $15°$ N), water upwells into upper layers of the Panthalassic Ocean down to $3600\,\mathrm{m}$, below which DW occurs. At 960 meters depth, the total UW along the Equator equals approximately $17\,\mathrm{Sv}$. This is the maximum total UW for any depth in the Tropics. The total UW stays close to this value between the depths of 700 and $1700\,\mathrm{m}$. Below $1700\,\mathrm{m}$ and above $700\,\mathrm{m}$, the amount of upwelled mass decreases steadily. At $3600\,\mathrm{m}$ depths, DW occurs, a total of $4.3\,\mathrm{Sv}$. Accordingly the overall sign of $\frac{\partial w}{\partial z}$ changes with z, which again influences the meridional velocity field though the Sverdrup Relation.

Matching the result up against the Sverdrup relation (2.14), it is clear that the changes in $\frac{\partial w}{\partial z}$ coincides with v, even in close vicinity of the Equator. The Sverdrup relation loses it's relevancy close to the Equator (as $f \to 0$), but for this model run it holds polewards of $\pm 4°$.

Studying the horizontal velocity fields (Figure 4.1), the NE and SE corners of the Panthalassic appear to be major DW sites, but the vertical velocity field itself is hard to decipher in these areas. Figure 4.10 can be more helpful when pinpointing where DW takes place. Here the DW and UW in different areas marked by the grid is calculated from the horizontal velocity field in the upper 1200 meters of the Panthalassic Ocean. Only the most relevant numbers are shown in Figure 4.10. The numbers indicate the net mass loss (-) or gain (+) in the locations by horizontal mass transport into the area. Mass loss indicates that a net *UW* of mass from the depths > 1200 meters, as a net influx of mass is needed in order to compensate for the total divergence, as the results are in steady state (i.e. no temporal change in surface height). A net *convergence* into an area would result in DW from this upper layer and into the deep ocean. The sizes of the arrows are proportional to the transport. Some of the transport arrows lack numbers for cleanness' sake. A complete figure can be seen in Appendix B, with all arrows and mass transports added.

Matching the numbers seen in Figure 4.10 together with the mass transports in the WBC shown in Table 4.1, it is seen that most of the water flowing into the Paleo-Tethys Sea from the Panthalassic past North and South China, and the UW into the WBL contributes to the WBC. A greater transport into Paleo-Tethys Sea in SH than in NH could possibly be a part of the explanation why SH WBC is more powerful than in the NH.

The most striking result seen in Figure 4.10 is the substantial DW region in the SE and corner of the Panthalassic. Close to 30 SV is sinking in this area. Adding the total sinking in the NE and NW corner, we see that approximately 30 SV is sinking in the NH polar areas in total. Some DW is also observed in the SW corner. Here approximately 6 Sv is sinking.

A net UW is observed in the midlatitude WBL in both hemispheres.

When studying the $uv-$field at intermediate depths, it is seen that more mass flow into the Paleo-Tethys Sea in SH. This is also observed in Figure 4.10. In the NH some the westward flow in the Panthalassic is steered northwards, east of North China and turned eastward along the continental shelf, before ever entering the Paleo-Tethys Sea. This also occurs in the SH, but to a lesser extent, possibly due to the fact that the strait separating the Panthalassic and the Paleo-Tethys Sea is wider in the SH than in the NH.

4.2 Heat Transport

The Late Permian was a time of great climatic change. An interesting aspect of these climatic changes are potential shifts in the heat budget. If the ocean temperature increased at the Equator, how much of that heat would reach the polar areas, potentially causing melting of sea ice, land ice, or gas hydrates? How sensitive is the heat transport to the continental configuration? It has been shown that the poleward ocean heat transport is highly sensitive to the placement of the continents. Among other things, Poussart et al. [1999] showed a $\sim 42\%$ increase in poleward heat transport in the SH compared to today for the Late Ordovician geographical configuration.

The continental configuration in the Late Permian is generally seen as favorable to meridional heat transport, with no possibility of circumpolar currents blocking meridional transport, as the Antarctic Circumpolar Current does today. However, a large uncertainty rests on the fact that the bathymetry of this period is not known. In Figure 4.1a the equilibrium SST from the model is shown. Note the difference in temperatures between this model run and that of Kiehl and Shields [2005]. Temperaturewise, the results discussed here and those seen in Figure 1.5 (Kiehl and Shields [2005]'s results) represent pre- and post the Siberian Traps eruption respectively. This is however, a comparison drawn by the author alone. The model runs are fundamentally different, and cannot be compared directly.

To calculate the meridional heat transport, it was assumed that the main transport mechanism is *advection*, i.e. the heat is transported with the current flow. Conductive heat transport is neglected. The temperature can then be seen as a conserved quantity. Assuming that the continuity equation $\nabla \cdot \vec{u} = 0$ holds and that the flow is steady, the advection equation looks as follows;

$$\nabla \cdot (\theta \vec{u}) = 0. \tag{4.4}$$

When looking at the meridional heat transport alone, (4.4) reduces to

$$v \frac{\partial \theta}{\partial y} = 0.$$

Numerically, this is done straight forwardly by multiplying the zonal velocity with the temperature at a given latitude. To calculate the total heat flow, the cumulative sum of the heat transport is calculated. The values for the density and heat capacity is taken from phy [2016]. I used $s = 35\,\mathrm{psu}$ and $T = 20°\mathrm{C}$.

Figure 4.2 shows the total meridional heat transport for all given latitudes. Comparing the results to Winguth et al. [2002]'s experiments on today's situation it is seen that the heat transport is more symmetrical around the Equator for the Late Permian. This could be due to the differences in continental geography, both due to the fact that the land masses are so unevenly distributed between the hemispheres today compared to the Late Permian, and the existence of the Antarctic Circumpolar Current. Winguth et al. [2002] also showed that the geography of South and North China could heavily influence the inflow of heat into the Paleo-Tethys Sea. However, they conducted this study for the Wordian stage (~ 265 million years ago). While differing from the Changhsingian stage ($\sim 254/252$ million years ago) in terms of paleogeography, the CO_2-concentration likely doubled over the ~ 10 million years separating the stages, from Wordian concentrations to concentrations following the Siberian Traps eruption Royer [2006].

Winguth et al. [2002]'s result, indicate that today's oceanic heat transport lies closer to $1000\,\mathrm{TW}$ at $\pm 30^\circ$, so there is some uncertainties tied to today's situation as well, and results may also vary due to differences in the model used, and the model implementations.

Either way, Ganachaud and Wunsch [2003]'s results also show that the oceanic heat transport today decreases with latitude at a higher rate than the MITgcm results shown here, which can also be seen for Winguth et al. [2002]. This could be due to several factors. i) Ganachaud and Wunsch [2003] is based on actual hydrological data, and is thus affected by the winds. The wind-driven oceanic gyres are responsible for a great deal of the oceanic heat transport [Wunsch, 2005]. ii) The shape of the continents today inhibit heat transport past 60° N in the Pacific Ocean, and past 60° S due to the Antarctic Circumpolar Current, and the continent of Antarctica. This is not the case for the Late Permian. iii), the method used to calculate the oceanic heat transport. Ganachaud and Wunsch [2003] used a different technique to calculate the heat transport than I did. Their method was based on inverse box models Wunsch [1996] and included vertical advection and diffusion between layers; an adjustment to Ekman transport and the net freshwater transports, including evaporation, precipitation, and river runoff in each oceanic box between sections where the hydrostatic measurements were made.

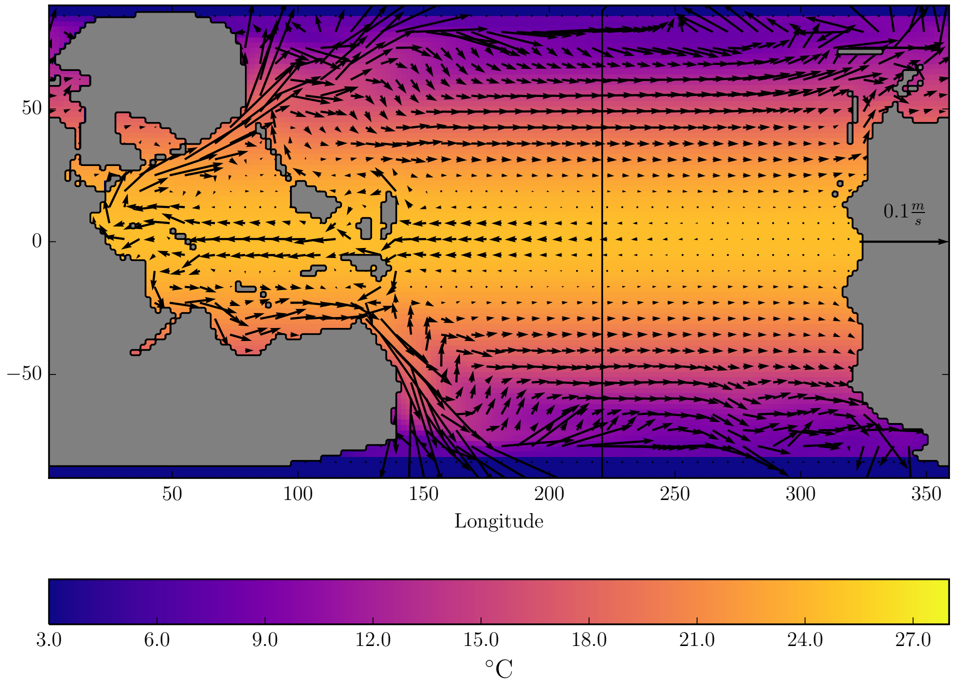
50
0
−50
50
100
150
200
250
300
350
Longitude
$0.1\frac{m}{s}$
3.0
6.0
9.0
12.0
15.0
18.0
21.0
24.0
27.0
°C

(A) Horizontal surface velocities are shown in black arrows, while the color map shows the surface temperature in °C. The line running though the center of the basin indicates the longitude at which the zonal velocity u is investigated below.

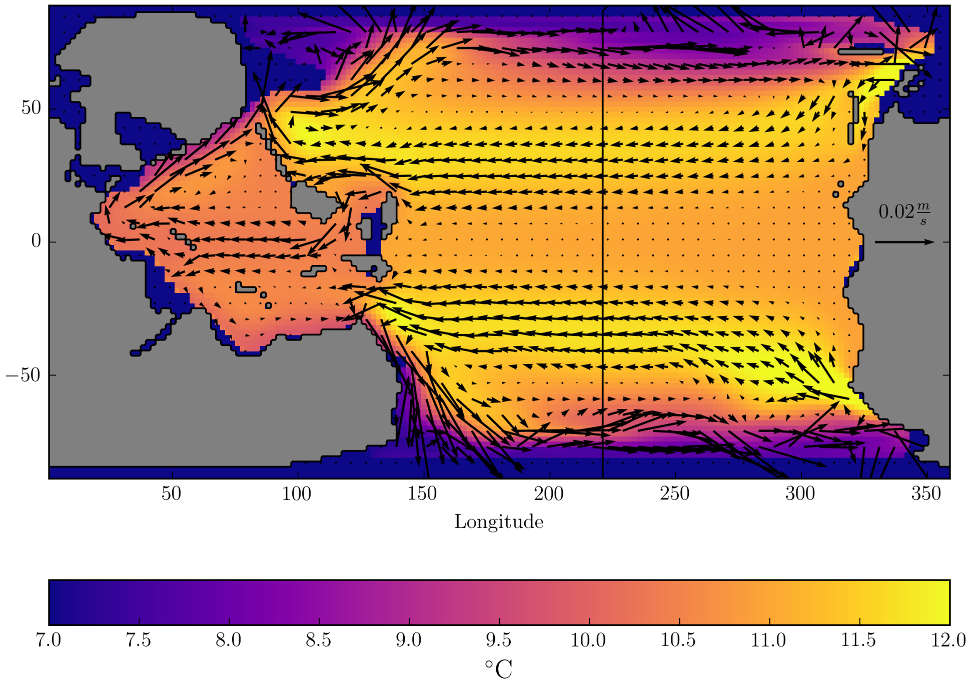
50
0
−50
50
100
150
200
250
300
350
Longitude
$0.02\frac{m}{s}$
7.0
7.5
8.0
8.5
9.0
9.5
10.0
10.5
11.0
11.5
12.0
°C

(B) Horizontal velocities for $z = 870\,\mathrm{m}$ are shown in black arrows, while the color map shows the surface temperature in °C. The line running though the center of the basin indicates the longitude at which the zonal velocity u is investigated below.

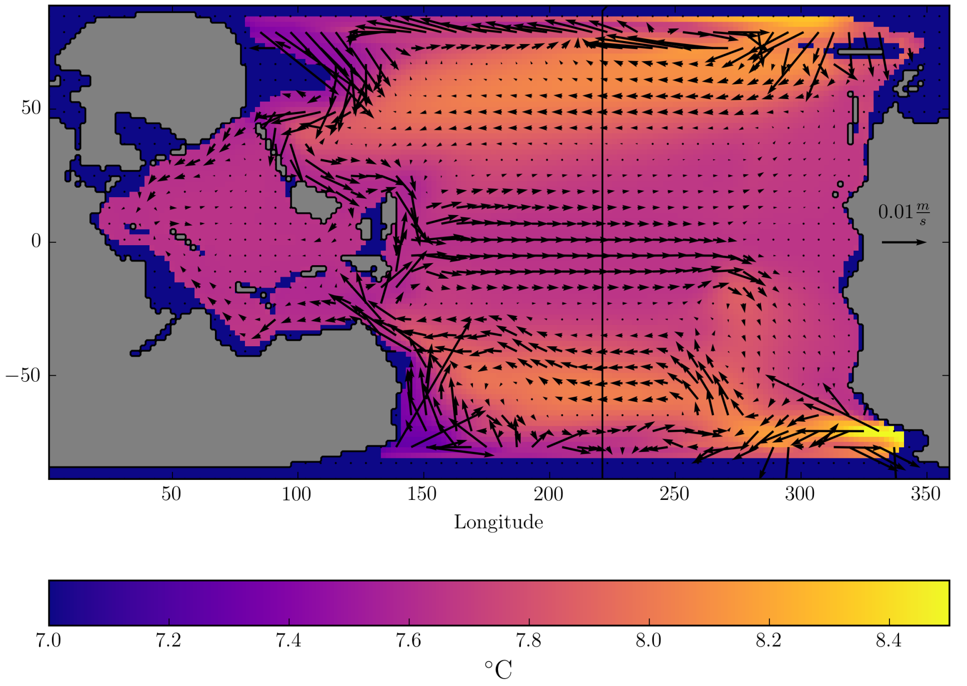
50
0
−50
50
100
150
200
250
300
350
Longitude
$0.01\frac{m}{s}$
7.0
7.2
7.4
7.6
7.8
8.0
8.2
8.4
°C

(C) Horizontal velocities for $z = 2250\,\mathrm{m}$ are shown in black arrows, while the color map shows the surface temperature in $^\circ\mathrm{C}$.

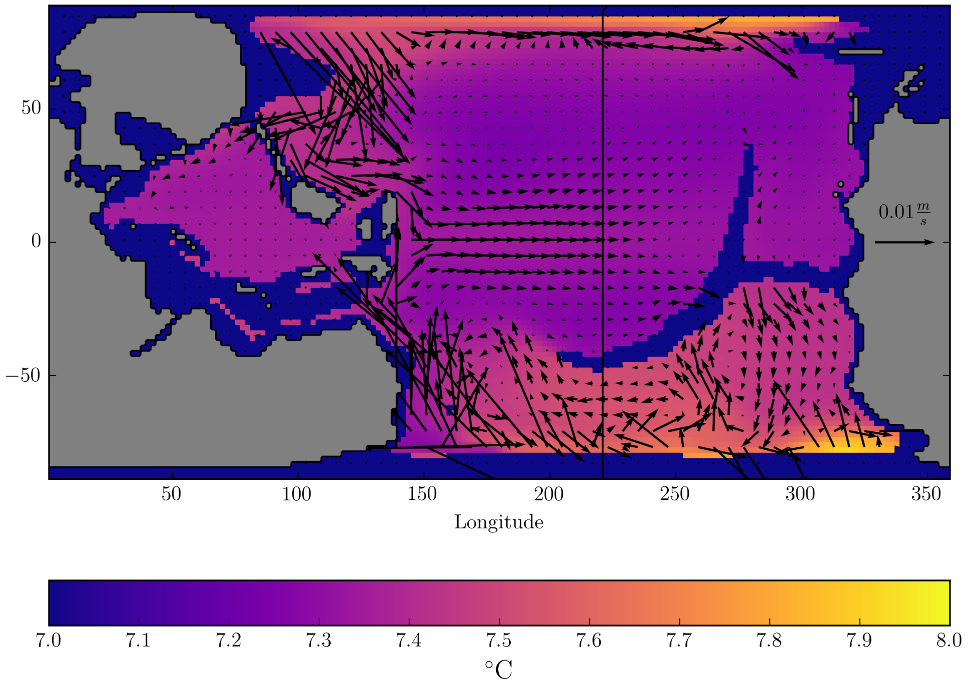
50
0
−50
50
100
150
200
250
300
350
Longitude
$0.01\frac{m}{s}$
7.0
7.1
7.2
7.3
7.4
7.5
7.6
7.7
7.8
7.9
8.0
°C

(D) Horizontal velocities for $z = 3920\,\mathrm{m}$ are shown in black arrows, while the color map shows the surface temperature in $^\circ\mathrm{C}$.

FIGURE 4.1: Continuation of horizontal velocities and temperature field in $^\circ\mathrm{C}$.

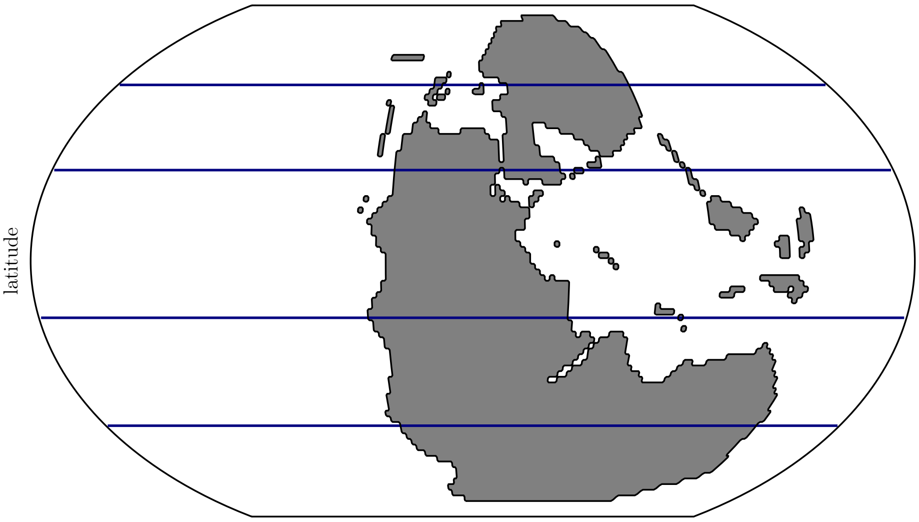

FIGURE 4.2: The blue lines mark the latitudes (60°S, 22°S, , 30°N, and 60°N) where the cross-sections of the meridional velocity component v was taken.

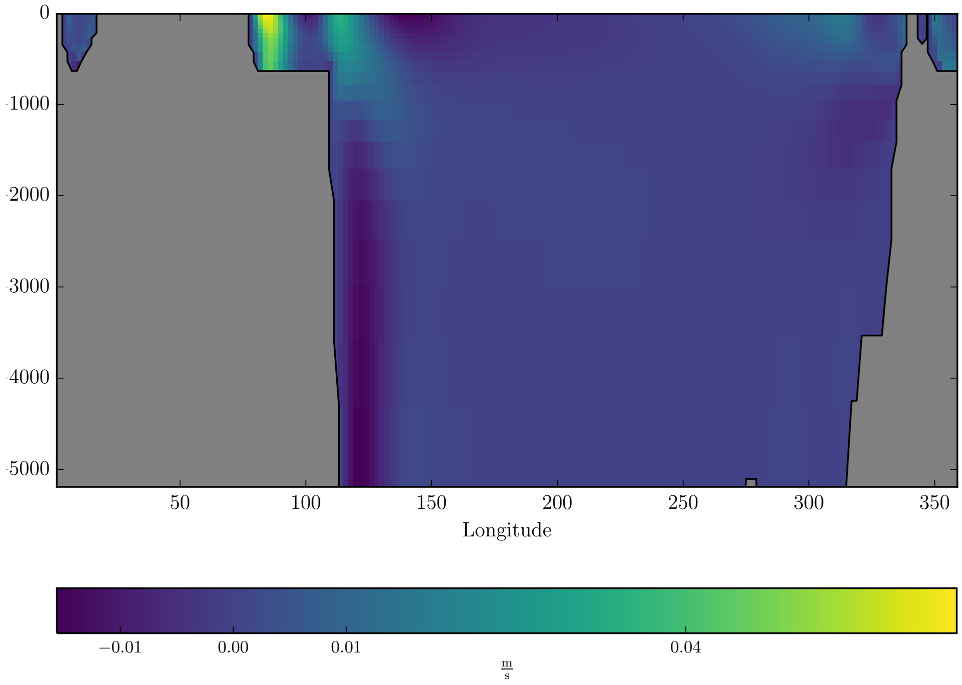

(A) The meridional velocity component at 60°N.

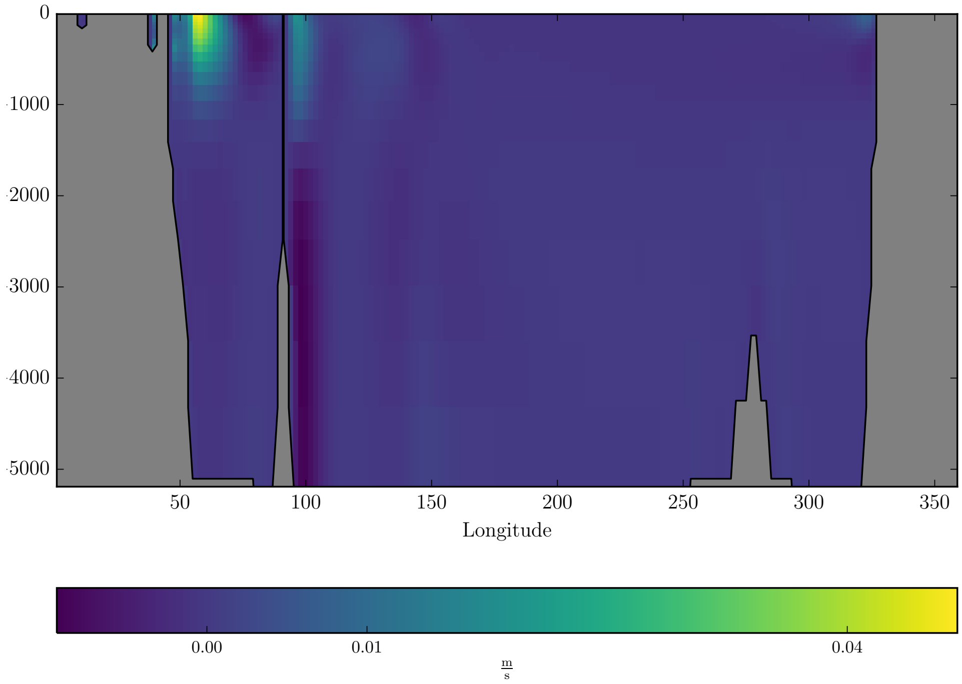

(B) The meridional velocity component at 30°N.

FIGURE 4.3: The variations of the meridional velocity component v with depth z and longitude taken at different latitudes in the NH. The locations of the sections can be seen on Figure 4.2.

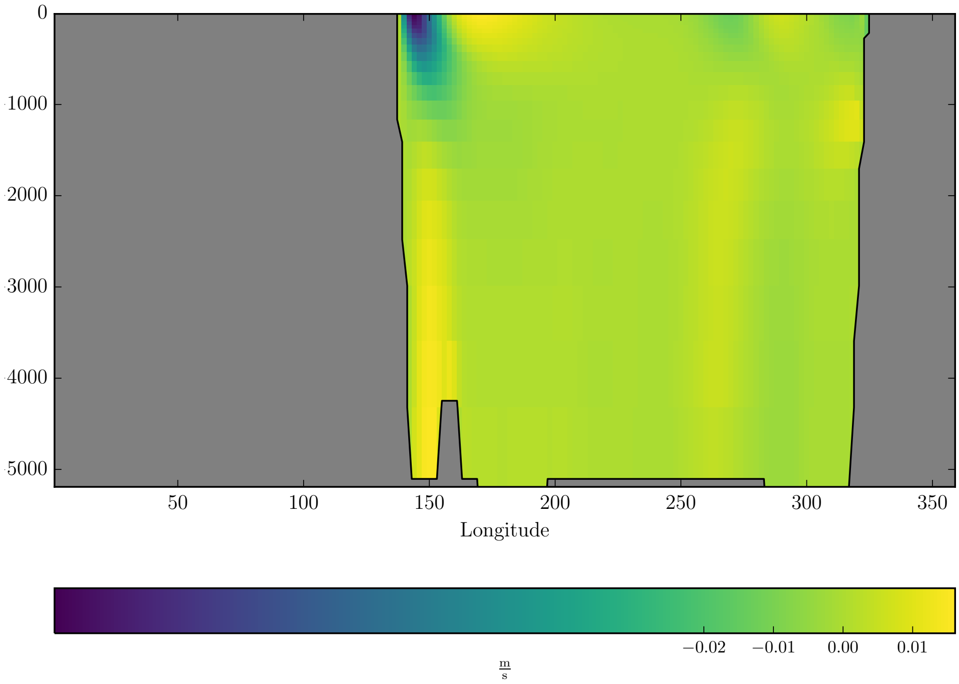

(A) The meridional velocity component at 60°S.

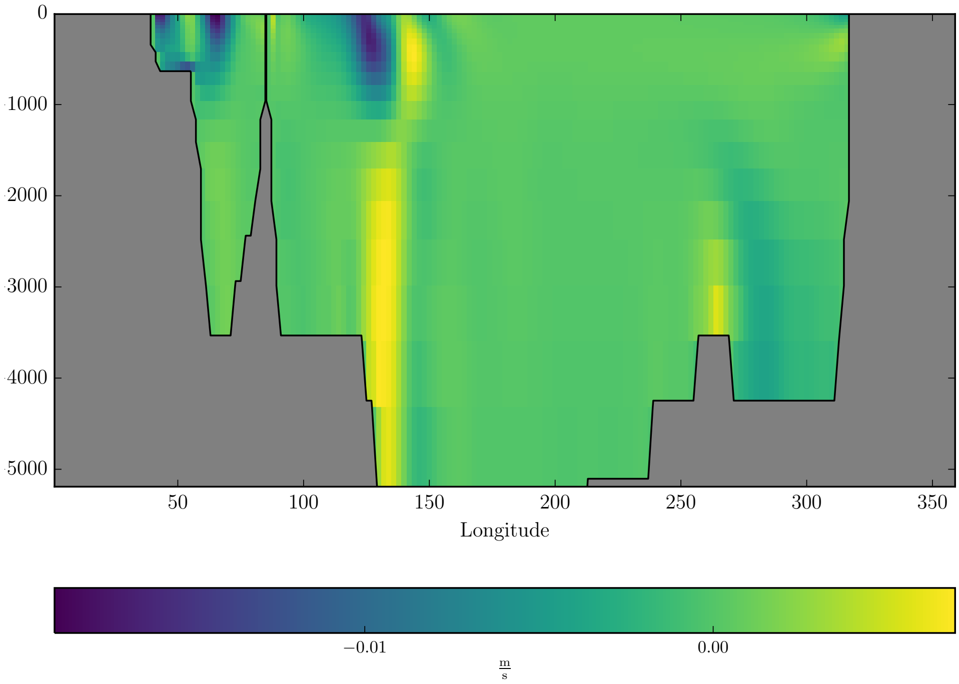

(B) The meridional velocity component at 22°S.

FIGURE 4.4: The variations of the meridional velocity component v with depth z and longitude taken at different latitudes in the SH. The locations of the sections can be seen on Figure 4.2.

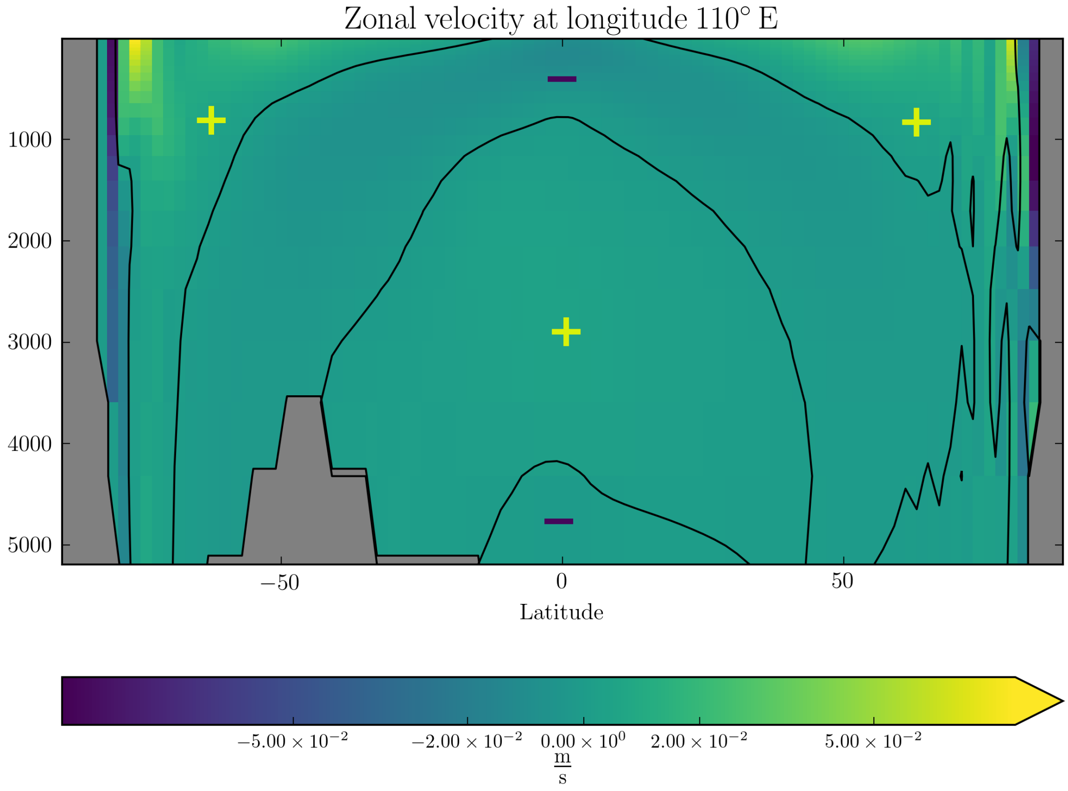

FIGURE 4.5: Figure shows the variation of the zonal velocity (u) with z for a single longitude 110° E, located in the middle of the Panthalassic Ocean. The vertical axis indicates depth. The velocities are generally small. The ± signs indicate whether the velocity is eastward (+) or westward (-) in that region, bounded by the black lines. At high latitudes the sign of u varies.

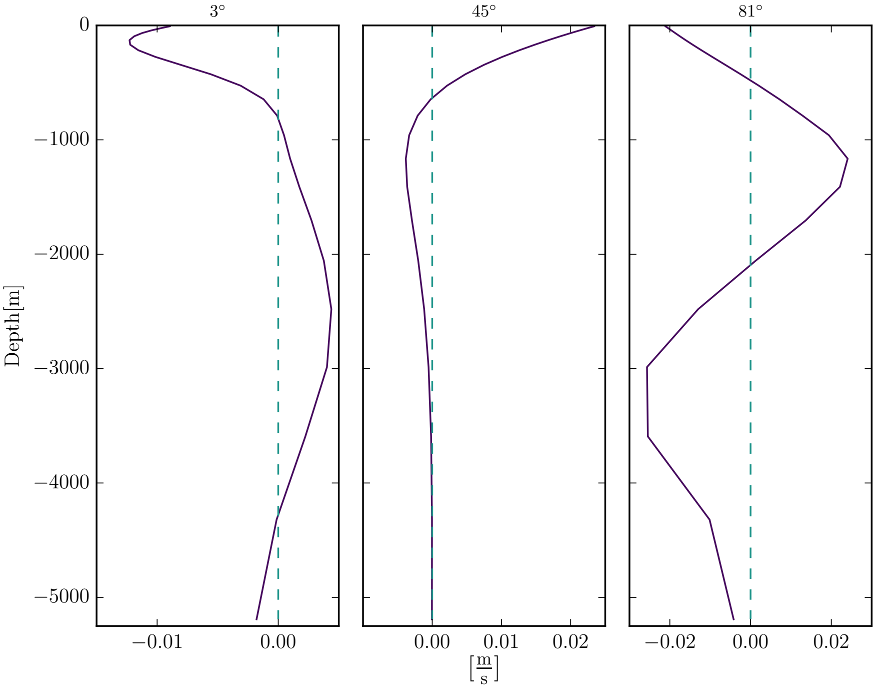

(A) the vertical profiles of u for some latitudes. The dashed lines show where the $u-$ values cross zero. The sections are taken from the same longitude.

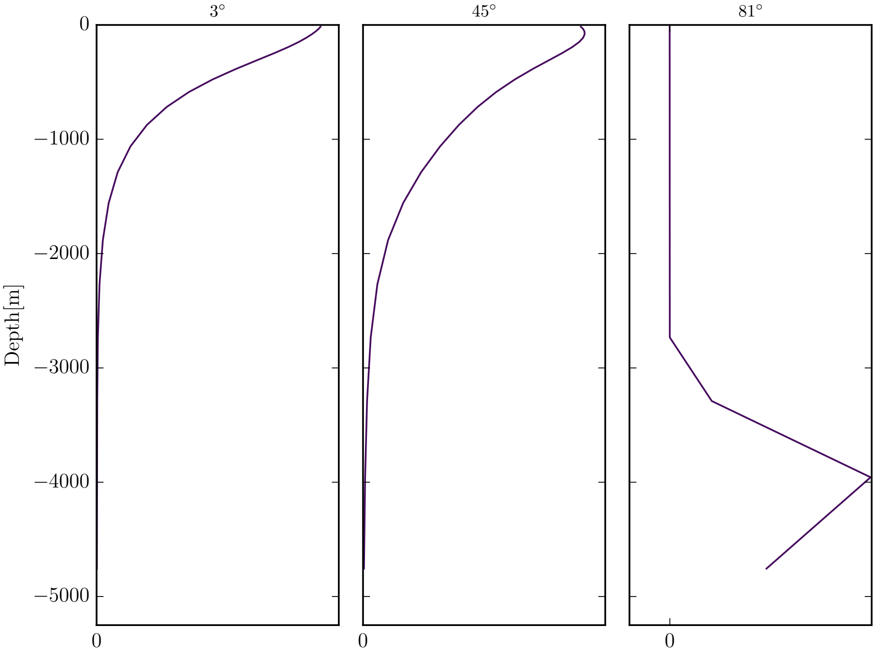

(B) The squared Brunt-Väisälä frequency N^2, where $N = \sqrt{-\frac{g}{\rho_c}\frac{\partial\rho}{\partial z}}$, concuring with the sections in Figure 4.6a. N is a measure of stability in the water column, where $N^2 > 0$ indicates stability, and $N^2 < 0$ refers to an unstable water column.

FIGURE 4.6: The zonal velocity u and the squared Brunt-Väisälä frequency N^2 for some latitudes along the same longitude (110° E), which is indicated by the vertical black line on figure 4.1

.

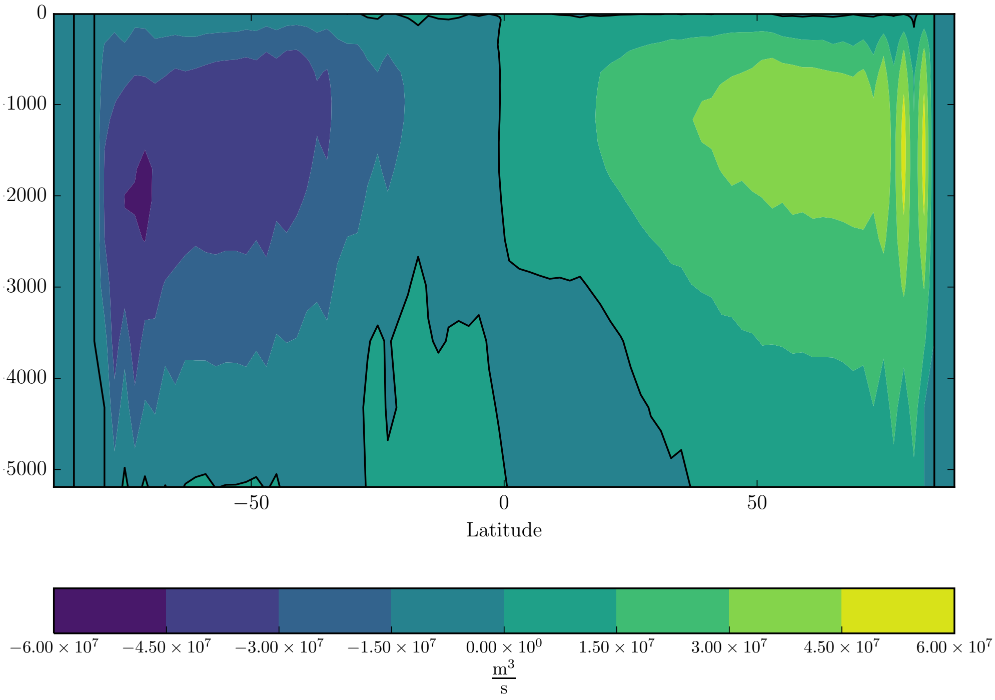

FIGURE 4.7: Figure showing the stream function Φ of the poleward transport. The black lines indicate where the transport goes from being negative (southwards) to positive (northwards). The black lines located at $\sim \pm 80^\circ$ show where the wall inhibiting flow into high latitudes is placed (see section 3). The colored values show the total mass transport at a given $z-$level and given latitude.

.

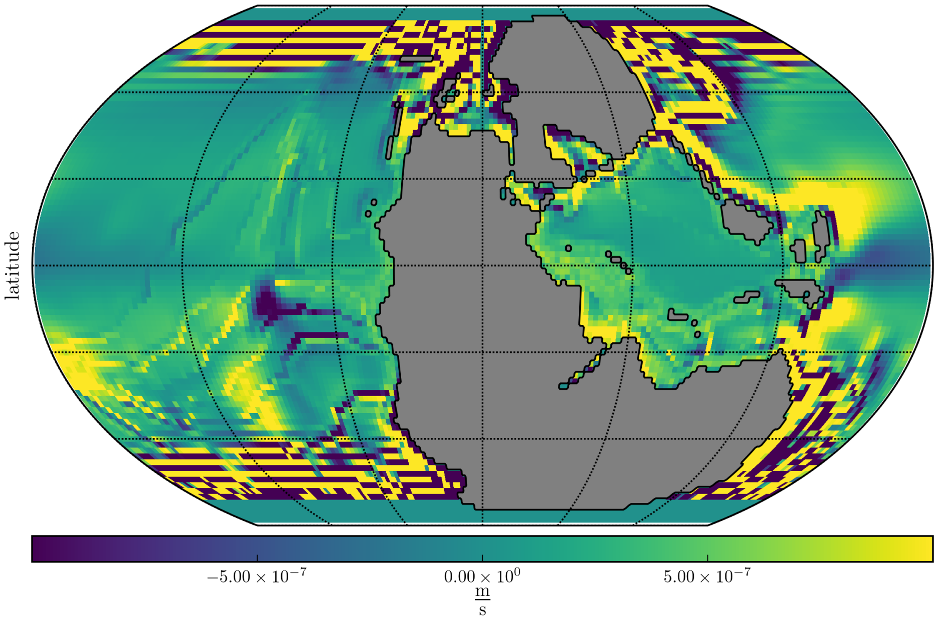
latitude
−5.00 × 10−7
0.00 × 100
5.00 × 10−7
m/s

FIGURE 4.8: Figure showing depth-integrated vertical velocity. Purple coloring indicates DW, and yellow UW.

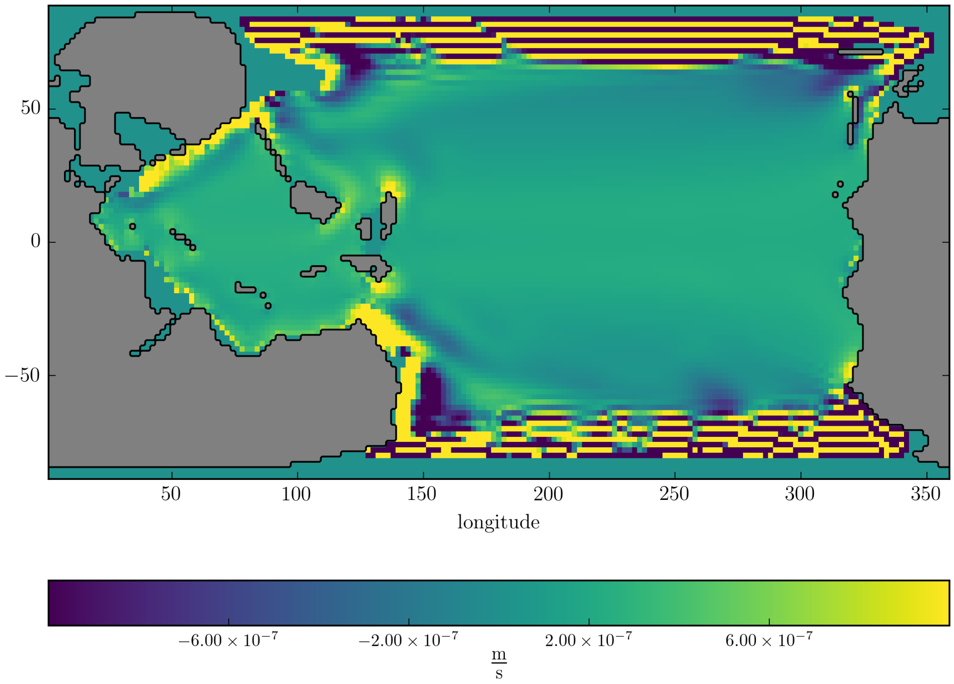
50
0
−50
50
100
150
200
250
300
350
longitude
-6.00×10^{-7}
-2.00×10^{-7}
2.00×10^{-7}
6.00×10^{-7}
$\frac{\mathrm{m}}{\mathrm{s}}$

(A) $w-$field at $z = 790$ meters.

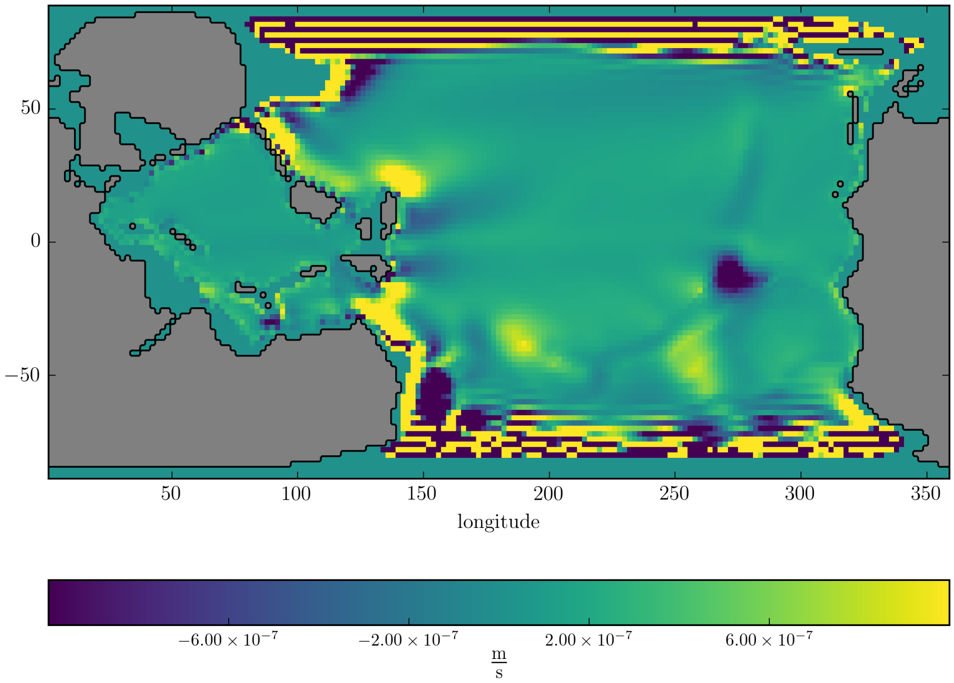
50
0
−50
50
100
150
200
250
300
350
longitude
-6.00×10^{-7}
-2.00×10^{-7}
2.00×10^{-7}
6.00×10^{-7}
$\frac{\mathrm{m}}{\mathrm{s}}$

(B) $w-$field at $z = 2480$ meters.

FIGURE 4.9: The vertical velocity in $\frac{\mathrm{m}}{\mathrm{s}}$ at different depths for all lon- and latitudes.

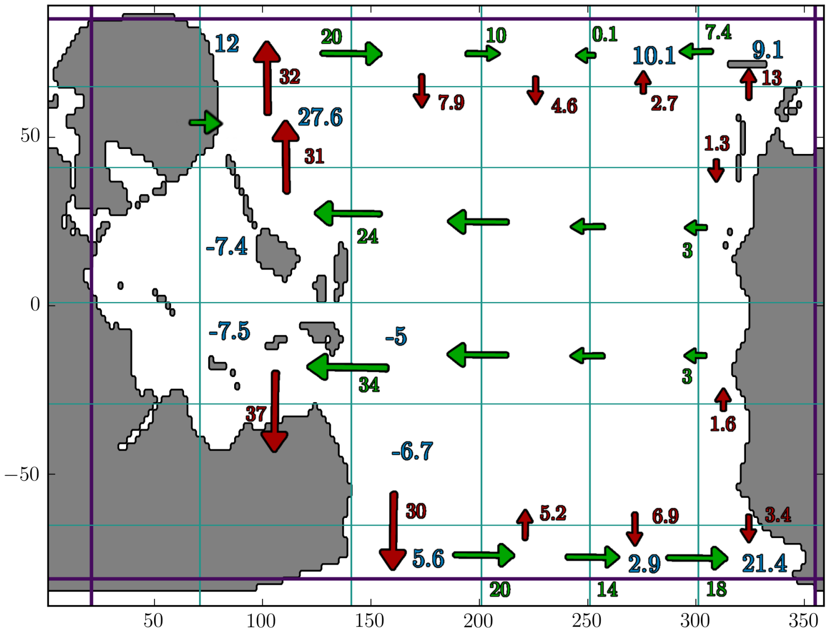
12
20
10
0.1
7.4
10.1
9.1
32
13
7.9
4.6
2.7
27.6
1.3
31
24
-7.4
3
-7.5
-5
34
3
37
1.6
-6.7
30
5.2
6.9
3.4
5.6
2.9
21.4
20
14
18
50
0
−50
50
100
150
200
250
300
350

FIGURE 4.10: Horizontal (red and green arrows) and vertical transport (blue arrows) for the upper 1200 meters. The negative vertical transport numbers points to UW, while the positive numbers are DW. Only the relevant numbers are shown in this figure. The size of the arrows are proportional to the transport. A full figure can be seen in Appendix B.

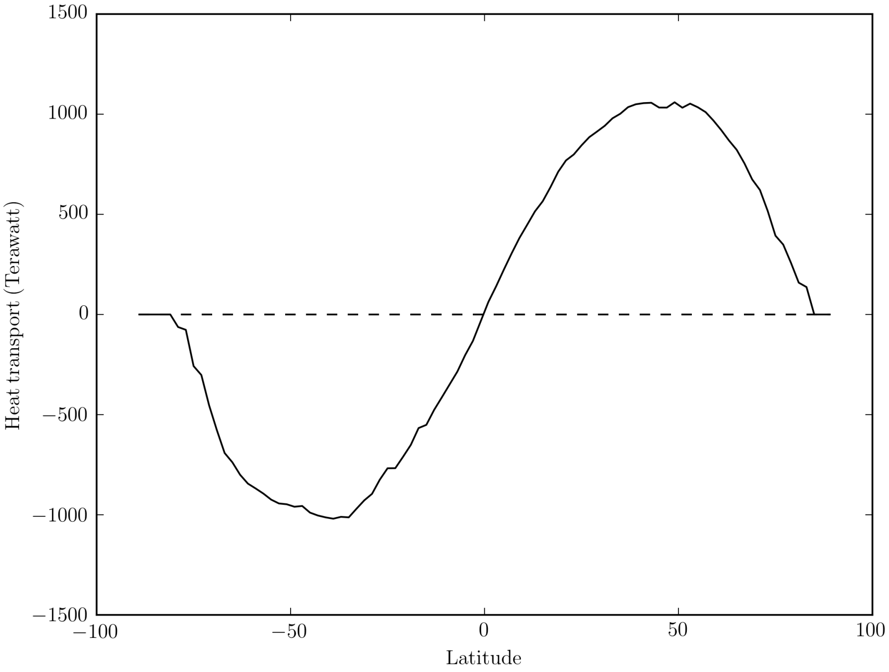

FIGURE 4.11: The total meridional heat transport given in terawatts ($= 10^{12}$ W)

.

Chapter 5

Discussion

5.1 Comparison between the MITgcm Results and the Theoretical Models

In the MITgcm simulation, an artificial wind mixing in the surface layer is employed through the diapycnal diffusivity κ_z. This is one of the many ways the model is set apart from Sandström's theory, described in Section 2.1.4. The other obvious difference is the existence of mechanical mixing over topography and in the boundary layers. Sandström's theory is also based on several assumptions not applicable to the real ocean. Among other things, the real ocean does not consist of closed streamlines alone, due to the existence of pressure gradients at the surface. This one of the assumptions made in Sandström's theory.

The Stommel-Arons theory described in Sections 2.1.3 and A.2.1 holds some similarities to the MITgcm results shown in Chapter 4. The WBC dominates the solution, the surface flow is generally eastward in both cases, and northwards in the EBL in both cases. The Stommel-Arons model predicts the NE corner to be a site of major DW, however. In the Late Permian case, the DW in the NH is spread out over a larger area, with $\sim 30\,\mathrm{Sv}$ sinking in total (Figure 4.10). In the SH the major DW site is located in the SE. The difference between the hemispheres can be related to the difference in topography, particularly the shallow continental shelf located in the NE of the basin, which inhibits water from the WBC from flowing into, and deep water from forming in this area. The structure of the WBC in the NH in the MITgcm run is highly influenced by the topography. The surface flow is separated in to branches, one in the Paleo-Tethys, and one in the Panthalassic. The return flow is mostly confined to the Panthalassic. Hence the upper and lower layer of the WBC is located away from one another.

The Stommel-Arons Model assume uniform UW in the interior, which is not the case for the MITgcm run. In the interior of the basin a weak and fairly uniform UW is observed, though areas of increased UW or DW is observed in the vicinity of steep topography, in the WBL and in polar areas (Figure 4.8). The non-uniform UW seen in the model is due to both non-linearity in the model and topographic effects.

5.2 General Discussion and Comparison to the Square Basin Case

Here the Late Permian model run will be compared to the square basin case conducted by LaCasce and Gjermundsen [2017]. In this section I will refer to the Late Permian run as P-r and the square basin case as Sq-r.

The WBL is an area of interest in both the P-r and the Sq-r. The WBC shows the same basic structure in both cases, though in the NH in the P-r, the poleward flow in the WBC is divided into two branches. The main branch originates in the Paleo-Tethys Sea, while the smaller branch flows east of North China.

In the SH the WBC shows the same structure as in the Sq-r. The transport in the WBC in the P-r is approximately $30\,\mathrm{Sv}$ in the NH, and $40\,\mathrm{Sv}$ in the SH -see Table 4.1. The poleward mass transport in the Sq-r is estimated to $20\,\mathrm{Sv}$. Looking at the stream function, Figure 4.7, the total MOC mass transport at these latitudes seems to be mostly due to WBC transport. The upper branch of the WBC runs slightly deeper in the P-r (down to ~ 1000 meters) than in the Sq-r (~ 800 meters). A recirculation region is seen just east of the WBC in both cases.

The difference in the strength of the WBC observed in the NH and SH for the P-r can be a result of the differing topography in the two hemispheres, affecting the width and depth of the current. The flow is generally narrower and shallower in the NH than in the SH. The general MOC -seen on Figure 4.7- look quite symmetrical around the Equator. This is to be expected as the forcing is the same in the two hemispheres, and the DW along the polar boundaries happen at approximately the same latitudes. Also, Figure 4.10 tells us that the total amount of DW is about the same in both hemispheres. Thus the asymmetry observed in the horizontal velocity field (Figure 4.1 is a result of topography.

In the EBL, a weak EBC is observed in the P-r, poleward in the surface layer, and equatorward beneath. In the Sq-r, the EBL shows the same structure as in P-r, though the subsurface, equaorwards velocities are more prominent, and the poleward surface current is almost absent. Comparing Figure 2.3 with Figure 4.1a we see that the poleward veering of the zonal surface velocities observed in the EBL for the P-r case is absent in the Sq-r. This implies that the rate of DW in the surface layers in the Sq-r is higher than in the P-r, where some of the mass flow from the interior supplies the surface EBL. The topography, as well as the difference in horizontal resolution in the two cases is what sets them apart in this area.

At the northern and southern boundary eastward velocities at the surface is observed in the P-r (Figure 4.5). It is clear that the surface mode is dominating, particularly at the northern boundary. The sloping topography at the boundary - which is absent in the Sq-r, could result in a mean transport at these latitudes. Just south of this eastward flow is westward surface flow with a weaker eastward flow below, resembling more the structure of the Sq-r (Figure 2.3b), where the first baroclinic mode dominates.

Around the Equator, the third baroclinic mode is more prominent in the P-r, as eastward surface flow, westward interior flow, and eastward flow at the bottom is observed. The prevalence of higher baroclinic modes at the Equator was also observed by de La Lama et al. [2016]. In the Sq-r the structure looks much the same as in P-r, though without the eastward bottom velocities. Comparing the interior flow in Figures 4.5 and 2.3b it is seen that the velocity fields in the interior of the basins look similar, with an eastward flow in the surface layer, and westward below. The depth of the surface layer increases with $\sim f^{\frac{2}{3}}$ in both cases, consistent with the depth of the thermocline calculated by LaCasce and Gjermundsen [2017]. The interior surface flow away from tropics is in geostrophic balance with the Equator to Pole temperature gradient in both cases. The differences in the flow in the tropics noted, could be related to the fact that the Equator is open in the P-r, while represented by a rigid boundary in the Sq-r.

Regarding the vertical velocity field, the P-r and Sq-r holds many similarities, like the existence of UW in the WBL and DW in the recirculation region and UW in upper layers at the Equator. The major difference between the two runs, -besides the influence of the topography surrounding the Paleo-Tethys Sea has on the vertical velocity field- lies in the location of DW along the northern boundary.

5.3 Comparison between the MITgcm Results and Paleo Proxy Data

In this section the geological results presented in Section 1.3.2 will be briefly compared to the MITgcm model results. The analysis of the proxy data focuses on the extinction event, while the model results better reflect the situation *before* it occurred.

Studying the MITgcm model results from the area around location 1 (Figure 1.4) studied by Schoepfer et al. [2012] it is seen that the model results point to the existence of UW in this area. The presence of UW in the EBL can be explained in terms of the Sverdrup Balance, and its strength depends on the rate of mass inflow into the EBL. This in turn depends on the Equator to Pole-gradient, so it is not unreasonable to assume that this UW system could be reduced as a result of a rapid increase in atmospheric CO_2 and polar warming. However, if changes in ocean circulation could result in the entire UW-system collapsing is unclear.

Wignall and Hallam [1996]'s result indicated that anoxia and euxina was prevalent in location 2, located in the promixty of the Equator in the Paleo-Tethys Sea. Studying the circulation pattern from the MITgcm model output on Figure 4.1 it is seen that, while the circulation turns weaker and more sluggish with depth, some coupling between the Paleo-Tethys and the Panthalassic exits down to depths of $\sim 4000\,\mathrm{m}$. Figure 4.9 shows that, while UW into the WBL occurs at intermediate depths, the rate of UW turns weaker with increasing depth. This could indicate that the deep water renewal rate in the Paleo-Tethys was slow, despite the large rate of inflow and outflow in upper layers (see Figure 4.10).

A proper sensitivity study, where the coupling between the Panthalassic and the Paleo-Tethys and the rate of water mass renewal is analyzed for different sill depths and bathymetry and compared to the available proxy data on anoxia in the area.

At location 3 Wignall and Hallam [1996] found that anoxia was only prevalent in the shallows, and that the deep ocean was still well oxygenated. In other words, oxygen rich deep waters was still available in this area throughout the PTr transition. Location 3 is close to the vicinity of the mid-ocean ridge in the MITgcm model run. If the bathymetry shown in Figure 3.2 is realistic for the Late Permian, such steep topography could lead to more well-mixed bottom waters. Additionally, location 3 is placed ideally to receive fresh water from the DW area in the SE corner (seen on Figure 4.10) though circulation in the cyclonic gyre observed in this area, particularly on Figure 4.1d. Lastly, at location 4, located in modern Spitsbergen Bond et al. [2015] found that anoxia only developed in certain areas, pointing to changes in nutrient supply as the main cause.

In the model run, this location is set on top of a shallow continental shelf in the NE of the Panthalassic Ocean. Looking at Figure 4.1a it is seen that the area is supplied by water though the EBC. The question then remains, how would a change in the equator to polar temperature gradient impact the EBC? Location 4 also lies in the vicinity of the Siberian Traps, and the promixty to the center of the catastrophe could have an impact on life here, and lead to extinction even without anoxia caused by shifts in the ocean circulation.

In the MITgcm model results we see that the South China area has a sluggish circulation compared to the Panthalassic and the western Paleo-Tethys (Figure 4.1c and 4.1d). The WBC has a two-layer structure, making it resemble baroclinic mode. Flows dominated by the first mode is affected by the topography all though the water column. it is possible that while the passages between the Panthalassic and the Paleo-Tethys are deep enough for water to flow though, the WBC is topographically steered along the eastern side of the Chinese Island, efficiently cutting off the eastern Paleo-Tethys from the main circulation. The flow in the upper layers is topographically steered into the eastern Paleo-Tethys, but this does not happen in the deep ocean. Thus the topography could play a direct role in the oxygen depletion around South China. South China is the most studied area from this time period, with a lot of well-preserved sections originating from here. The circulation in the Paleo-Tethys is highly sensitive to the topography, and determining the topography in here is necessary to determine whether the observed anoxia is a result of changes in circulation, nutrient levels, or both.

5.4 Issues with the Model

In this section, the uncertainties related to the model, and implementations will be discussed.

First of all, the sea level in the Late Permian could have an impact on the ocean circulation, particularly in the boundary layers, as the flow is dependent on the shape of the continental border. Hallam and Wignall [1999] argued that the PTr transition was a time of marine transgression, which is often observed along with anoxic events.

An other uncertainty lies, as previously mentioned, in the topography surrounding the Paleo-Tethys Sea. Among other things, the MITgcm results imply that the depth and width of the passage between North China and mainland Pangea have the potential to drastically alter the WBC flow.

The effects a prescribed, uniform salinity has on the flow would depend on the rate of sea ice formation and brine release. While disregarding these effects in the present climate would be inadvisable, it has been shown that sea ice formation in the Late Permian was at a minimum, and the temperatures shown in Figure 4.1 imply that there was little or no ice formation. Also, the Permo-Triassic weather is not well known, and adding salinity into the equation could potentially lead to misleading results, as the precipitation patterns are unresolved.

A large simplification in the model run lies in the disregarding of the winds. The WBC is known to be partially wind driven and partially driven by density gradients. Additionally, the large scale weather patterns could potentially alter the interior surface circulation of the ocean, and contribute to mixing in the surface layer, though surface mixing is prescribed in the model. The winds could also have an impact on the U/DW patterns along the continental borders and at the Equator, as is seen today. Studies show that the atmospheric circulation on the PTr boundary can be sensitive to topography and land elevation [Fluteau et al., 2001]. As the knowledge on the exact Late Permian topography is still under development, this makes the wind field a potential source of uncertainty in paleoanographic studies.

It's worth noting that the length of the day in the Late Permian was shorter than it is today by approximately 40 minutes [Denis et al., 2002]. This accounts for the Coriolis parameter increasing by $\sim 3\%$. Not a large increase, but worth keeping in mind when working on paleoceanography. An increase in the Coriolis parameter could lead to a decrease in the MOC, as the scale of the general overturning goes as $f^{-\frac{1}{3}}$ [Robinson and Stommel, 1959]. This would only result in a $\sim 0.7\,\%$ reduction in the MOC for the Late Permian. An other issue related to paleooceanography is the change in the lunar tidal forcing. In the Late Permian the Moon was approximately 1008 kilometers closer to the Earth than it is today, or the Moon-Earth distance then was approximately $99.7\,\%$ of what it is today, resulting in an increase of $\sim 0.2\,\%$ the gravitational pull from the Moon. Again, not a large number, but enough to demonstrate that the astronomical effects can add some uncertainty to studies in paleoclimate.

In the EBL, the flow can be affected by the model resolution. Park [2006] ran an experiment with on ocean only model with a high ($0.25°$) and a low ($2°$) resolution. Their result showed that the circulation was not significantly sensitive to the resolution, except for in polar areas, and in the EBL. At higher resolutions a northward flowing EBC appeared. Park [2006] conducted a simple scaling analysis based on the linear vorticity equation and revealed that the EBC is initiated by vortex column stretching, related to DW at the eastern wall. The rate of the DW is linked to the sea surface temperature gradient. They predicted that the magnitude of the EBC is inversely proportional to the horizontal resolution. It was concluded that a $0.5°$ resolution is required to resolve the EBL. The lateral viscosity coefficient also plays a role in resolving the EBL, as the stratification in the layer affects the rate of DW. An increased temperature advection in the EBL would increase the stratification and thus reduce the DW, so that a larger part of the zonal flow turns poleward and strengthens the EBC.

Park [2006] also investigated how the northern boundary was affected by the resolution. They found that, as the resolution becomes higher, the deep convection site in the NH is pushed along the northern wall from the northeastern corner to the middle, coupled with an increased stratification. This in turn, weakens vertical convection, and consequently the high latitude DW. They found that the MOC was reduced by 30% in the high resolution case ($0.25°$) compared to the coarsest ($1°$).

The MITgcm model is run in a hydrostatic mode, which implies that w is calculated from the continuity equation. In other words, along the boundaries, particularly at high latitudes, the model simulates artificially large values for w, hence the calculated vertical velocity field may show unrealistically high values along the polar boundaries, though w is often larger in non-hydrostatic runs.

Kirtman et al. [2012] also demonstrated, with a full ocean-atmosphere coupled model (CCSM3.5) that the poleward oceanic heat transport increased for high resolution models ($0.1°$ vs $1.2°$). Perhaps surprisingly this increase in heat transport is not a result of better resolved eddies, but changes in the mean circulation itself.

The model run described in this thesis was conducted with a 2° × 2° horizontal resolution, which puts it in the low resolution categories described above. Regarding the EBC, Figures 4.3 and 4.4 show that the model run shows a clear EBC, though the results of Park [2006] imply that the strength of the current could hold some uncertainty. However, Park [2006]'s runs were conducted with a flat bottom, and the resolution issues may not be so serious with topography present at the boundary. A sloping topography would cause the EBC to turn polewards, as the Sverdrup relation (2.14) holds in the EBL. On the polar boundaries, our results show indeed that the NH convection site is located along a longer stretch of latitudes than in the square basin run, which was conducted at a higher resolution ($0.45° \times 0.45° \cdot \cos(\theta)$) than the Late Permian run. Though this could be an effect of the topography in the NE corner.

Running models at lower resolutions saves computational time due to length of run. Isolated, specific processes that is missing in the lower-resolution climate models has been discovered, and it has been shown that lower resolution models could lead to poor representation of ocean currents [Kelly and Thompson, 2016].

Chapter 6

Summary and Concluding Remarks

The overall goal of this thesis was to compare the buoyancy driven circulation in the Late Permian to a similar case, based on a square basin set-up, as well as discussing the Late Permian results in view of some theoretical models and knowledge gathered from paleoproxy data, and previous numerical paleoceanographic studies.

The results show that a square basin approximation for the Late Permian situation - while showing some of the same characteristics - is not a satisfactory approximation to the situation in the Late Permian. The main features, such as an eastward surface interior flow, a strong WBC, and UW along the Equator in surface layers is prevalent in both cases, but the inclusion of realistic topography leads to some major differences. The shape and strength of the MOC depends on the latitude at which major DW occur. While the major DW occurred at approximately the same latitudes in both runs, and the strength of the DW was of the same magnitude, the shape of the DW area differs in the two cases. The addition of continental shelves and sloping bathymetry along the boundaries affected the flow in the Late Permian case, particularly along the polar boundaries. The inclusion of seafloor topography has profound local effects in both the vertical and horizontal velocity field. The topography around the Paleo-Tethys Sea strongly affected the WBC in the NH, as the main northwards flow was located in the Paleo-Tethys, and the subsurface returnflow in the Panthalassic Ocean.

Regarding theoretical models, it is clear that while some characteristics predicted by the theory is seen in the Late Permian results, the assumptions made in the the theory does not fit with the model results. Theoretical models are however, useful to gain a greater understanding of the driving mechanisms behind the ocean circulation, and separating the different effects.

About the paleoproxy data, the focus of this thesis was to study the evidence of widespread anoxic or euxinic conditions on the PTr boundary, and compare the data to the model results. Anoxia is often correlated with ocean stagnation, as water not in contact with the surface will eventually get depleted in oxygen. Thus comparing the ocean circulation and the existence of oxygen depleted waters can be used as a tool to understand whether the anoxic conditions evolved due to circulation, or biological factors, as well as validating the model. Comparing the model results to paleoproxy data it was seen that anoxia was present in areas with little circulation, it was also present at locations where where circulation was not stagnant. It is however, imperative to keep in mind that the model study was conducted for the situation *prior* to the Permian mass extinction, and the onset of the widespread anoxia. A comparison for the ocean situation before and after the Siberian Traps volcanic eruption should be conducted to fully understand the role the ocean circulation had in triggering the anoxic conditions observed. Moreover, analyzing the model results in terms of paleodata illustrate the importance of the topography surrounding the Paleo-Tethys Sea. This is the most studied area from the PTr boundary, and comparing this result to previous studies imply that the coupling between the Paleo-Tethys and the Panthalassic Ocean is crucial when it comes to the strength of the circulation and its possible role in depleting the waters in the Paleo-Tethys Sea of oxygen.

This thesis is meant as a proof of concept study. It is illustrated that coupling an OGCM with known proxydata can be a useful tool for separating causes and effects regarding the Permian extinction at the PTr boundary, as the short time span of the event makes using proxydata to establish the sequence of events challenging.

Appendix A

Calculations

A.1 Calculations on mixing

Starting with

$$\frac{\partial \vec{u}}{\partial t} + \vec{u} \cdot \nabla \vec{u} + f\hat{k} \times \vec{u} = -\nabla \phi + b\hat{k} + \nu \nabla^2 \vec{u}$$

and utilizing the vector identity

$$(\mathbf{A} \cdot \mathbf{B}) = \mathbf{A} \times (\nabla \times \mathbf{B}) + (\mathbf{A} \cdot \nabla)\mathbf{B} + \mathbf{B} \times (\nabla \times \mathbf{A}) + (\mathbf{B} \cdot \nabla)\mathbf{A},$$

inserting $\vec{u} = A$ and $\vec{u} = B$ yields

$$\vec{u} \cdot \nabla \vec{u} = \frac{1}{2}|\vec{u}|^2 + (\vec{\omega}) \times \vec{u},$$

where $\vec{\omega} = \nabla \times \vec{u}$. Inserting into (2.7) and rearranging the terms results in

$$\frac{\partial \vec{u}}{\partial t}(2\omega + f\hat{k}) \times \vec{u} = -\nabla B + b\hat{k} + \nu \nabla^2 \vec{u},$$

where B is the Bernoulli function given by $B = \frac{1}{2}|\vec{u}|^2 + \frac{p'}{\rho_0}$. Multiplying by $\vec{u}$ yields

$\cdot\frac{\partial \vec{u}}{\partial t}(2\omega + f\hat{k}) \times \vec{u} \cdot \vec{u} = -\nabla B \cdot \vec{u} + b\hat{k} \cdot \vec{u} + \cdot\vec{u}\nu \nabla^2 \vec{u},$

and further utilizing the reciprocal and the product rule for derivatives, and continuity $\nabla \cdot \vec{u} = 0$, we end up with the Bernoulli Equation:

$$\frac{1}{2}\frac{\partial}{\partial t}\vec{u}^2 = -\nabla \cdot (\vec{u}B) + wb + \nu\vec{u} \cdot \nabla^2\vec{u},$$

The second term on the LHS falls out because the Coriolis force does not carry out work on the fluid. The term on the LSH is a measure of the kinetic energy E_k. The kinetic energy of a parcel depends on the pressure, conversion between potential energy to kinetic energy, and dissipation.

Utilizing that $\nabla^2\mathbf{A} = \nabla(\nabla \cdot \mathbf{A}) - \nabla \times (\nabla \times \mathbf{A})$ and

$\nabla \cdot (\mathbf{A} \times \mathbf{B}) = \mathbf{B} \cdot (\nabla \times A) - \mathbf{A} \cdot (\nabla \times \mathbf{B})$ we can write the last term on the RHS as

$$\nu\vec{u} \cdot \nabla^2\vec{u} = \nu\vec{u} \cdot (\nabla(\nabla \cdot \vec{u}) - \nabla \times (\nabla \times \vec{u})).$$

Utilizing that $\nabla \cdot u = 0$, and $\vec{\omega} = \nabla \times \vec{u}$:

$$\nu\vec{u} \cdot \nabla^2\vec{u} = \nu\vec{u} \cdot (-\nabla \times \vec{\omega})) = \nu(\nabla \cdot (\vec{u} \times \vec{\omega}) - \vec{\omega} \cdot (\nabla \times \vec{u})).$$

Finally the last term of the Bernoulli Equation becomes

$$\nu\vec{u} \cdot \nabla^2\vec{u} = -\nu(\nabla \cdot (\vec{u} \times \vec{\omega}) - \vec{\omega}^2).$$

Integrating over a closed basin with rigid no-slip boundaries -$\vec{u} = 0$ here, the first term on the RHS disappears, and we are left with:

$\int\int\int_V \nu\vec{u} \cdot \nabla^2\vec{u}dV = -\nu\langle\vec{\omega}^2\rangle \equiv -\epsilon < 0.$

Thus integrating the Bernoulli Equation over a closed basin yields

$$\frac{\mathrm{D}}{\mathrm{d}t}\langle\frac{1}{2}\vec{u}^2\rangle = \langle wb\rangle - \epsilon,$$

Where angle brackets denote volume integration, and is the total kinetic energy dissipation given by $\epsilon = \langle wb\rangle$. ϵ is negative.

The potential energy can be expressed in terms of bz. Thus the potential energy equation can be obtained by multiplying the buoyancy equation (2.8) by z and integrating over the whole domain. This yields

$$\frac{\mathrm{D}}{\mathrm{d}t}\langle\frac{1}{2}\vec{u}^2 - bz\rangle = \langle zQ\rangle - \epsilon,$$

where Q is the total heating given by $Q = J - \kappa\nabla^2 b$. With no surface heating, i.e. $Jz = 0$ for all z, the potential energy and kinetic energy equations can be combined to obtain

$$\langle zQ\rangle = -\nu\langle\vec{\omega}^2\rangle < 0. \tag{A.1}$$

Hence the heat source term is balanced by the energy dissipation, which is strictly negative. The RHS of the equation above is defined negative, and thus heating and the height z must be negatively correlated, or the heating must on average, occur on lower $z-$levels than the cooling.

A.2 Calculations on the Stommel-Arons model

The calculations are heavily based on Cessi [2001] and Vallis [2006]. The starting point will be an adaptation of the planetary geostrophic equations in a steady state, which look as follows in the lower layer (ρ_2):

$$f\hat{k} \times \vec{u} = -\nabla_H \phi_2 + -r\vec{u}, \tag{A.2}$$

where $\phi_2 = \frac{p_2'}{\rho_2}$. It can be written as

$$\hat{k}f \times \vec{u} = \frac{1}{\rho_2}\nabla p_2 - r\vec{u}, \tag{A.3}$$

where $p_2 = p_{02}(z) + p_2'(x,y)$, omitting the z-variance in the perturbation term. $r \ll f$ is the dissipation rate. Since $\rho_1, \rho_2 = \text{const.}$ the hydrostatic equation (2.4), and the continuity equation (2.3) applies in both layers;

$$\frac{\partial p_{1,2}}{\partial z} = -\rho_{1,2}g. \tag{A.4}$$

Ignoring the smaller terms, equation (A.4) can be integrated to obtain

$$p_1(z) = -\rho_1 g z + p_1'(x,y) \tag{A.5}$$

and

$$p_2(z) = -\rho_2 g z + p_2'(x,y). \tag{A.6}$$

The pressure is continuous at the interface between the upper and lower layer at $z = -h$, thus $p_1(-h) = p_2(-h)$, which results in

$$p_2'(x,y) = -\rho_2 g' h + p_1'(x,y), \tag{A.7}$$

where $g' \equiv g\frac{\rho_2-\rho_1}{\rho_2}$ is the *reduced gravity*. Now we can express the pressure in the lower layer in terms of the layer thickness $H - h$ by integrating in the vertical and taking the gradient.

$$\int_{-H}^{-h} p_2\,dz = \int_{-H}^{-h} \rho_2 g' h + p_1'\,dz p_2(-h) - p_2(-H) = \rho_2 g'(H-h) + \int_{-H}^{-h} p_1'\,dz \quad \text{(A.8)}$$

If the horizontal velocities are small, we can assume that the change in p_1' is small, and hence take $\int_{-H}^{-h} p_1' dz = (H-h)p_1' \simeq \text{const.}$ Thus

$$\nabla p_2 = \nabla(\rho_2 g'(H-h) + \text{const.}) = \rho_2 g' \nabla H - h. \quad \text{(A.9)}$$

The momentum equation becomes

$$f\hat{k} \times \vec{u} = -g'\nabla(H-h) - r\vec{u}. \quad \text{(A.10)}$$

We have that $\nabla\vec{u} = 0$, hence the height of the lower layer is directly proportional to the net injection of mass. The continuity equation can be written as

$$\frac{\partial h}{\partial t} + \nabla \cdot (\vec{u}h) = S, \quad \text{(A.11)}$$

where S is the local mass gain, so the local mass input through convection minus the loss by UW into the upper layer.

Straight-forward manipulation of equations (A.10) and (A.11) through cross-multiplication yields the *potential vorticity equation* (PV-equation) for this shallow water system:

$$\frac{\mathrm{D}}{\mathrm{d}t}\left(\frac{f}{H-h}\right) = -\frac{r}{H-h}\nabla \times \vec{u} - \frac{fS}{(H-h)^2}. \quad \text{(A.12)}$$

In the interior of the basin we assume that $\frac{r}{f} \to 0$, and hence the first term on the RHS vanishes away from boundaries. The flow is then considered geostrophic, and the PV-equation, (A.12) is reduced to

$$\beta v = -\frac{S}{H-h}, \quad \text{(A.13)}$$

which resembles the Sverdrup Balance (equation (2.14)).

In the lower layer the continuity equation can be expressed in terms of the mass transport, by integrating in the vertical as follows:

$$\vec{U} \equiv \int_{-H}^{-h} \hat{u} = u(H-h)\hat{\imath} + v(H-h)\hat{\jmath}. \tag{A.14}$$

Hence

$$Ux + Vy = s_u = -w', \tag{A.15}$$

where w' is given by

$$w' \equiv \int_{z=-H}^{z=-h} \frac{\mathrm{d}w}{\mathrm{d}z}\mathrm{d}z = w(-h) - w(-H) = w(-h). \tag{A.16}$$

Since we are away from convective sources, $S = s_u < 0$, where s_u is the *local* mass loss though UW. s_u is considered uniform. Thus the interior flow is polewards, regardless of the location of the convective mass source.

w' in equation (A.16) is the diffusive UW rate, through which the lower layer loses mass to the upper layer. $w(-H)$ is the vertical velocity at the bottom of the basin, which is taken to be zero.

In a steady state, it is assumed that the mass injection from the upper to the lower layer at high latitudes is compensated by the UW. Thus to satisfy this steady state condition we can write $S_0 - S_u = 0$, where S_u is the total loss by UW from the abyssal layer in the basin and S_0 is the total mass input though convection. We can then write

$$S_u = \int_{\text{basin}} w'\mathrm{d}x\mathrm{d}y = -S_0. \tag{A.17}$$

A.2.1 Solutions

First equation (A.10) and (A.11) are rewritten in terms of the mass transports,

$$f\hat{k} \times \vec{U} = -g'\nabla\Phi - r\vec{U} \tag{A.18}$$

where $\Phi = g'\frac{(H-h)^2}{2}$. We consider r to be much smaller than f, and thus the mass transport is approximately equal to $\vec{U} = \frac{1}{f}\hat{k} \times \nabla\Phi$. Inserting this into the RHS of equation (A.18) gives

$$\vec{U} = \frac{1}{f}\hat{k} \times \nabla\Phi - \frac{r}{f^2}\nabla\Phi. \tag{A.19}$$

Decomposing equation (A.19) and differentiating the zonal and meridional component with respect to x and y, and inserting into equation (A.15), recalling that $f = f_0 + \beta y$ yields

$$\frac{\beta}{f}\Phi x = -fs_u - f\nabla \cdot (\frac{r}{f^2}\nabla\Phi). \tag{A.20}$$

The last term on the RHS vanishes in the interior. Inserting $V = \frac{1}{f}\Phi x$ into equation (A.20), keeping in mind that $V \equiv v(H - h)$ we are back to equation (A.13). Due to conservation of mass however, the flow can not be poleward through the entire range of longitudes. Thus we impose a frictional western boundary layer, where the frictional forces matter. We can write $\Phi = \Phi_I + \Phi_B$, assuming that the interior field Φ_I and the boundary layer correction Φ_B do not depend on each other.

Solving for the interior field where $\frac{\beta}{f}\Phi_I x = -fs_u$ through integration from the eastern boundary to some longitude x in the interior:

$$\Phi_I = \Phi_I(x, y) = \frac{f^2}{\beta}s_u(x_E - x) + \Phi_C, \tag{A.21}$$

where Φ_C is the integration constant (i.e. the value of Φ_I at the eastern boundary x_E), which may be set to zero, as its value has no impact on the flow, which depends on the *derivative* of Φ, and we are working in a square basin.

At the western boundary we assume that the frictional term in equation (A.20) is much larger than the stretching term. Moreover, it was assumed that the zonal variations in Φ_B are greater than the meridional variations in the boundary layer ($\frac{\partial^n\Phi_B}{\partial y^n} \ll \frac{\partial^n\Phi_B}{\partial x^n}$). Omitting the derivatives of Φ_B in the $y-$ direction, the dominant balance in the western boundary layer becomes

$$\beta\Phi_B x = -r\Phi_B x. \tag{A.22}$$

Integrating twice in the $x-$direction, and recalling that $\Phi = \Phi(x, y)$ the solution becomes

$$\Phi_B = C(y)e^{-\frac{r}{\beta}x}, \tag{A.23}$$

and by the following reasoning, $C(y)$ can be determined: We have assumed that the abyssal circulation is in a steady state, hence the total loss of mass through UW to the upper layer equals the total input of mass through convection at high latitudes. Also, the net mass flux equatorwards of any latitude y is zero. Hence the equatorward mass flux in the boundary current at latitude y equals the poleward interior flux at the same latitude minus the loss of UW. The convective source term is not taken into the calculation because it is assumed that the convective region is poleward of y. Assuming that y is in the northern hemisphere, that the southern boundary of the basin is at the Equator $(y = 0)$, and that the western boundary is situated at $x = 0$, we can calculate the mass loss though UW

$$\int_0^y \int_0^{x_E} s_u = s_u x_E y \equiv U(y), \tag{A.24}$$

and the interior flux past latitude y. Taking $\Phi_C = 0$;

$$\int_0^{x_E} V\,\mathrm{d}x = \int_0^{x_E} \frac{1}{f}\Phi_i x\,\mathrm{d}x \int_0^{x_E} \frac{1}{f}\frac{f^2}{\beta}s_u(x_E - x)x)\,\mathrm{d}x = \int_0^{x_E} -\frac{f}{\beta}s_u\,\mathrm{d}x = -\frac{f}{\beta}s_u x_E = -\frac{f}{\beta}s_u x_E. \tag{A.25}$$

In the western boundary layer $\Phi_B \gg \Phi_I$ and thus the boundary flux $= \int_0^\infty V_b\,\mathrm{d}x$, where V_b is the meridional mass transport in the boundary layer can be calculated. We can integrate from zero to infinity because it is assumed that $\Phi_B \to 0$ for large x.

$$\int_0^\infty V_b\,\mathrm{d}x = \int_0^\infty \frac{1}{f}\Phi_B x - \frac{r}{f^2}\Phi_B y\,\mathrm{d}x \simeq \int_0^\infty \frac{1}{f}\Phi_B x dx = \int_0^\infty C(y)e^{-\frac{\beta}{r}x}\,\mathrm{d}x = C(y). \tag{A.26}$$

We can integrate from zero to inifinty because it is assumed that $\Phi_B \to 0$ for large x. It is assumed that $\frac{r}{f}\Phi_B y \ll \Phi_B x$. Thus the boundary flow changes more rapidly in the $x-$ than the $y-$direction.

By mass conservation the boundary layer flux past latitude y equals the interior flow past y plus the UW south of y. Since the southern boundary is situated at $y = 0$, we take $f = \beta y$. Hence

$$C(y) = U(y) + \frac{f}{\beta}s_u x_E = s_u x_E y + \frac{f}{\beta}x_E s_u = s_u(x_E y + \frac{\beta y}{\beta}x_E) = 2s_u x_E y \qquad \text{(A.27)}$$

To satisfy mass conservation in the entire basin, the total mass loss though UW must equal the total mass input by convection. By using equation (A.27) and keeping in mind that s_u is considered a constant we have that

$$S_0 = \delta x \delta y s_u = (x_E - x_W)(y_N - y_S)s_u = -x_e y_N s_u. \qquad \text{(A.28)}$$

Solviung for s_u and inserting into equation (A.27), keeping in mind that $s_u < 0$ yields

$$C(y) = -2S_0 \frac{y}{y_N}. \qquad \text{(A.29)}$$

Inserting (A.29) into (A.23), the complete solution for Φ becomes

$$\Phi = \Phi_B + \Phi_I = -2S_0 \frac{y}{y_N} e^{-\frac{r}{\beta}x} + \frac{f^2}{\beta}s_u(x_E - x). \qquad \text{(A.30)}$$

Appendix B

The complete Figure 4.10

Box number	vertical transport [Sv]
A1	0
A2	-0.1
A3	-5.3
A4	-2.4
A5	0.1
A6	0
B1	12
B2	2.6
B3	-7.4
B4	-7.5
B5	9
B6	7
C1	2.1
C2	-7.6
C3	-4.5
C4	-5
C5	-17.7
C6	5.6
D1	5.4
D2	-1.1
D3	-4.3
D4	-2.8
D5	-1.3
D6	0.8
E1	5.1
E2	1.2
E3	-5.9
E4	4.6
E5	-1.7
E6	2.9
F1	9.1
F2	-1
F3	1.7
F4	-1.4
F5	-1.6

TABLE B.1: The DW (positive numbers) and UW (negative numbers) in the areas marked by the boxes in Figure B.1.

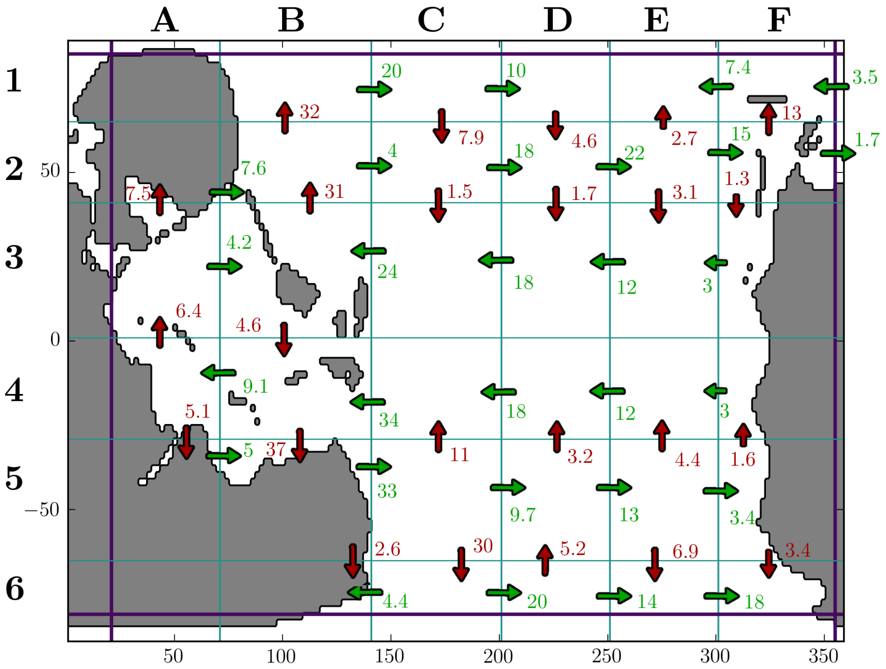
A
B
C
D
E
F
1
2
3
4
5
6
50
0
−50
20
10
7.4
3.5
32
7.9
4.6
2.7
13
15
1.7
4
18
22
7.6
1.3
7.5
31
1.5
1.7
3.1
4.2
24
18
12
3
6.4
4.6
9.1
18
12
3
34
5.1
11
3.2
4.4
1.6
5
37
33
9.7
13
3.4
2.6
30
5.2
6.9
3.4
4.4
20
14
18
50
100
150
200
250
300
350

FIGURE B.1: The full figure showing the horizontal transport between different areas, as in Figure 4.10. The arrows are not scaled to proportion to the transport. Transitions between boxes without arrows indicate transports $< 10^{-4}$ Sv. Red arrows show zonal transport, green arrows meridional. The DW in the different locations is given in the table below. Each box is labeled with one letter from A-F and a number 1-6 given by the names of the columns and rows.

Appendix C

MITgcm Model Parameters

```
# ====================
# | Model parameters |
# ====================
#
# Continuous equation parameters
 &PARM01
 sRef = 24*35.,
 no_slip_sides=.TRUE.,
 no_slip_bottom=.TRUE.,
 viscAr=1.E-4,
 viscAhGrid=0.1,
 diffKhT=500.,
 diffKrT=1.E-4,
 diffKhS=0.,
 diffKrS=0.,
 rhonil=1035.,
 rhoConstFresh=1000.,
 eosType = 'JMD95Z',
 ivdc_kappa=100.,
 rigidLid=.FALSE.,
 implicitFreeSurface=.TRUE.,
 implicitViscosity=.TRUE.,
 implicitDiffusion=.TRUE.,
 allowFreezing=.FALSE.,
 tempAdvScheme = 33,
 StaggerTimeStep = .TRUE.,
 vectorInvariantMomentum = .TRUE.,
 useRealFreshWaterFlux=.FALSE.,
 useCDscheme=.FALSE.,
 hFacInf=0.1,
 hFacSup=5.,
 hFacMin=0.3,
 hFacMinDr=50.,
# set precision of data files
 readBinaryPrec=32,
 writeBinaryPrec=32,
 &

# Elliptic solver parameters
 &PARM02
 cg2dMaxIters=500,
 cg2dTargetResidual=1.E-10,
 &

# Time stepping parameters
 &PARM03
# 1000 years of integration will yield a reasonable flow field
 startTime =          0.,
 endTime   = 31536000000.,
 deltaT= 1800.,
 abEps = 0.1,
 cAdjFreq=0.,
 pChkptFreq= 0.,
 dumpFreq=   1.5768E9,
 taveFreq=   1.5768E9,
 monitorFreq= 86400.,
# 1 months restoring timescale for temperature
 tauThetaClimRelax=  2592000.,
# 6 months restoring timescale for salinity
# tauSaltClimRelax = 15552000.,
 tauSaltClimRelax = 0.,
 periodicExternalForcing=.FALSE.,
# externForcingPeriod=2592000.,
# externForcingCycle=31104000.,
 &
```

Appendix D

Thickness of Vertical Layers in MITgcm

Layer	Thickness in meters
1	14.8461
2	17.7881
3	21.3130
4	25.5365
5	30.5969
6	36.6601
7	43.9247
8	52.6290
9	63.0581
10	75.5539
11	90.5259
12	108.4648
13	129.9585
14	155.7114
15	186.5677
16	223.5385
17	267.8356
18	320.9107
19	384.5033
20	460.6977
21	551.9909
22	661.3751
23	792.4352
24	949.4666

TABLE D.1: The thickness of the vertical layers used in the MITgcm model run, starting from the surface layer.

Bibliography

Mitgcm online documentation. `http://mitgcm.org/public/r2_manual/latest/`, 2006. [Latest update: 2017-01-02].

National physical laboratory: Kaye and laby: Tables of physical and chemical constants. `http://www.kayelaby.npl.co.uk/`, 2016. [Value extracted November 2016].

David Beerling. *The Emerald Planet: How Plants Changed Earth's History*. Oxford University Press; 1 edition, 2008. ISBN 0199548145.

Michael J. Benton and Richard J. Twitchett. How to kill (almost) all life: the end-permian extinction event. *Trends in Ecology Evolution*, 18(7):358–365, 2003. ISSN 0169-5347. doi: http://dx.doi.org/10.1016/S0169-5347(03)00093-4.

Robert A. Berner. Examination of hypotheses for the permo–triassic boundary extinction by carbon cycle modeling. *Proceedings of the National Academy of Sciences*, 99(7): 4172–4177, 2002. doi: 10.1073/pnas.032095199.

David P.G. Bond, Paul B. Wignall, Michael M. Joachimski, Yadong Sun, Ivan Savov, Stephen E. Grasby, Benoit Beauchamp, and Dierk P.G. Blomeier. An abrupt extinction in the middle permian (capitanian) of the boreal realm (spitsbergen) and its link to anoxia and acidification. *Geological Society of America Bulletin*, 127(9-10):1411–1421, 2015. doi: 10.1130/B31216.1.

Gregory A. Brennecka, Achim D. Herrmann, Thomas J. Algeo, and Ariel D. Anbar. Rapid expansion of oceanic anoxia immediately before the end-permian mass extinction. *Proceedings of the National Academy of Sciences*, 108(43):17631–17634, 2011. doi: 10.1073/pnas.1106039108.

Seth D. Burgess and Samuel A. Bowring. High-precision geochronology confirms voluminous magmatism before, during, and after earth's most severe extinction. *Science Advances*, 1(7), 2015. doi: 10.1126/sciadv.1500470.

Paola Cessi. Thermohaline circulation variability. Lecture notes, 2001. URL `https://www.whoi.edu/fileserver.do?id=21418&pt=10&p=17292`.

Thomas M. Cronin. *Paleoclimates: Understanding Climate Change Past and Present*. Columbia University Press, 2009. ISBN 9780231144940.

Ying Cui and Lee R. Kump. Global warming and the end-permian extinction event: Proxy and modeling perspectives. *Earth-Science Reviews*, 149:5–22, 2014. ISSN 0012-8252. doi: http://dx.doi.org/10.1016/j.earscirev.2014.04.007.

Marta Sanchez de La Lama, J H LaCasce, and Helle Kristine Fuhr. The vertical structure of ocean eddies. *Dynamics and Statistics of the Climate System*, 1(1):dzw001, 2016. doi: 10.1093/climsys/dzw001.

C Denis, A.A Schreider, P Varga, and J Závoti. Despinning of the earth rotation in the geological past and geomagnetic paleointensities. *Journal of Geodynamics*, 34(5):667–685, 2002. ISSN 0264-3707. doi: http://dx.doi.org/10.1016/S0264-3707(02)00049-2.

Mathew Domeier, Rob Van der Voo, and Trond H. Torsvik. Paleomagnetism and pangea: The road to reconciliation. *Tectonophysics*, 514-517:14–43, 2012. ISSN 0040-1951. doi: http://dx.doi.org/10.1016/j.tecto.2011.10.021. URL `//www.sciencedirect.com/science/article/pii/S0040195111004550`.

Douglas H. Erwin. *Extinction: How Life on Earth Nearly Ended 250 Million Years Ago*. Princeton University Press, 2008. ISBN 978-0691136288.

Raffaele Ferrari and David Ferreira. What processes drive the ocean heat transport? *Ocean Modelling*, 38(3-4):171 – 186, 2011. ISSN 1463-5003. doi: http://dx.doi.org/10.1016/j.ocemod.2011.02.013. URL `http://www.sciencedirect.com/science/article/pii/S1463500311000485`.

F. Fluteau, J. Besse, J. Broutin, and G. Ramstein. The late permian climate. what can be inferred from climate modelling concerning pangea scenarios and hercynian range altitude? *Palaeogeography, Palaeoclimatology, Palaeoecology*, 167(1–2):39 – 71, 2001. ISSN 0031-0182. doi: http://dx.doi.org/10.1016/S0031-0182(00)00230-3.

Alexandre Ganachaud and Carl Wunsch. Large-scale ocean heat and freshwater transports during the world ocean circulation experiment. *Journal of Climate*, 16(4):696–705, 2003. doi: 10.1175/1520-0442(2003)016<0696:LSOHAF>2.0.CO;2.

Sarah T Gille, E Joseph Metzger, and Robin Tokmakian. Seafloor topography and ocean circulation. *Oceanography*, 17(1):47–54, 2004.

A. Hallam and P.B. Wignall. Mass extinctions and sea-level changes. *Earth-Science Reviews*, 48(4):217–250, 1999. ISSN 0012-8252. doi: http://dx.doi.org/10.1016/S0012-8252(99)00055-0.

Roberta M. Hotinski, Karen L. Bice, Lee R. Kump, Raymond G. Najjar, and Michael A. Arthur. Ocean stagnation and end-permian anoxia. *Geology*, 29(1):7–10, 2001. doi: 10.1130/0091-7613(2001)029<0007:OSAEPA>2.0.CO;2.

Yuangeng Huang, Zhong-Qiang Chen, Paul B. Wignall, and Laishi Zhao. Latest permian to middle triassic redox condition variations in ramp settings, south china: Pyrite framboid evidence. *Geological Society of America Bulletin*, 2016. doi: 10.1130/B31458.1.

Harley E. Hurlburt and J. Dana Thompson. The dynamics of the loop current and shed eddies in a numerical model of the gulf of mexico. Technical Report ADA114352, Naval Ocean Research and Development Activity, October 1981.

Yukio Isozaki. Permo-triassic boundary superanoxia and stratified superocean: Records from lost deep sea. *Science*, 276(5310):235–238, 1997. ISSN 0036-8075. doi: 10.1126/science.276.5310.235.

Yoshimichi Kajiwara, Satoshi Yamakita, Kotaro Ishida, Hiroaki Ishiga, and Akira Imai. Development of a largely anoxic stratified ocean and its temporary massive mixing at the permian/triassic boundary supported by the sulfur isotopic record. *Palaeogeography, Palaeoclimatology, Palaeoecology*, 111(3):367–379, 1994. ISSN 0031-0182. doi: http://dx.doi.org/10.1016/0031-0182(94)90072-8.

Kathryn A. Kelly and Luanne Thompson. Climate science: Unexpected fix for ocean models. *Nature*, 535(7613):497–498, 2016. doi: 10.1038/535497a.

Jeffrey T. Kiehl and Christine A. Shields. Climate simulation of the latest permian: Implications for mass extinction. *Geology*, 33(9):757–760, 2005. doi: 10.1130/G21654.1.

Ben P. Kirtman, Cecilia Bitz, Frank Bryan, William Collins, John Dennis, Nathan Hearn, James L. Kinter, Richard Loft, Clement Rousset, Leo Siqueira, Cristiana Stan, Robert Tomas, and Mariana Vertenstein. Impact of ocean model resolution on ccsm climate simulations. *Climate Dynamics*, 39(6):1303–1328, 2012. ISSN 1432-0894. doi: 10.1007/s00382-012-1500-3.

J.H. LaCasce. Diffusivity and viscosity dependence in the linear thermocline. *Journal of Marine Research*, 62(6):743–769, 2004. doi: doi:10.1357/0022240042880864.

Joseph LaCasce. Surface quasigeostrophic solutions and baroclinic modes with exponential stratification. *Journal of Physical Oceanography*, 42(4):569–580, 2012. doi: 10.1175/JPO-D-11-0111.1.

Joseph LaCasce and Ada Gjermundsen. Comparing the linear and nonlinear buoyancy driven circulation. *Tellus*, 2017.

Joseph H. LaCasce. The preference for the ocean surface mode. 2017. Submitted February 2017.

Alban Lazar, Gurvan Madec, and Pascale Delecluse. The deep interior downwelling, the veronis effect, and mesoscale tracer transport parameterizations in an ogcm. *Journal of Physical Oceanography*, 29(11):2945–2961, 1999. doi: 10.1175/1520-0485(1999)029<2945:TDIDTV>2.0.CO;.

J.R. Ledwell, Andrew J. Watson, and Clifford S. Law. Evidence for slow mixing across the pycnocline from an open-ocean tracer-release experiment. *Nature*, 364:701–703, 1993. doi: doi:10.1038/364701a0.

J.R. Ledwell, E.T. Montgomery, K.L Polzin, L.C. St. Laurent, R.W. Schmitt, and Toole J.M. Evidence for enhanced mixing over rough topography in the abyssal ocean. *Nature*, 403:179–182, 2000. doi: doi:10.1038/35003164.

Jochem Marotzke and Jeffery R. Scott. Convective mixing and the thermohaline circulation. *Journal of Physical Oceanography*, 29(11):2962–2970, 1999. doi: 10.1175/1520-0485(1999)029<2962:CMATTC>2.0.CO;2.

John Marshall and R. Alan Plumb. *Atmosphere, Ocean and Climate Dynamics: An Introductory Text*. Academic Press, 2007. ISBN 978-0125586917.

Walter Munk and Carl Wunsch. Abyssal recipes ii: energetics of tidal and wind mixing. *Elsevier*, 45:1977–2010, 1998.

R. Dietmar Müller, Maria Sdrolias, Carmen Gaina, and Walter R. Roest. Age, spreading rates, and spreading asymmetry of the world's ocean crust. *Geochemistry, Geophysics, Geosystems*, 9(4), 2008. ISSN 1525-2027. doi: 10.1029/2007GC001743.

Angela K. Osen, Arne M.E. Winguth, Cornelia Winguth, and Christopher R. Scotese. Sensitivity of late permian climate to bathymetric features and implications for the mass extinction. *Global and Planetary Change*, 105:171–179, 2013. ISSN 0921-8181. doi: http://dx.doi.org/10.1016/j.gloplacha.2012.01.011. New developments in Permian-Triassic paleoceanographic and global climate system research.

Young-Gyu Park. Dependence of an eastern boundary current on the horizontal resolution in thermally driven circulations. *Journal of Geophysical Research: Oceans*, 111 (C9), 2006. ISSN 2156-2202. doi: 10.1029/2005JC003362.

Young-Gyu Park and Kirk Bryan. Comparison of thermally driven circulations from a depth-coordinate model and an isopycnal-layer model. part ii: The difference and structure of the circulations. *Journal of Physical Oceanography*, 31(9):2612–2624, 2001. doi: http://dx.doi.org/10.1175/1520-0485(2001)031<2612:COTDCF>2.0.CO;2.

Jonathan L. Payne and Matthew E. Clapham. End-permian mass extinction in the oceans: An ancient analog for the twenty-first century? *Annual Review of Earth and Planetary Sciences*, 40(1):89–111, 2012. doi: 10.1146/annurev-earth-042711-105329.

Joseph Pedlosky. Linear theory of the circulation of a stratified ocean. *Journal of Fluid Mechanics*, 35(1):185–205, 1969. doi: 10.1017/S0022112069001030.

Pascale F. Poussart, Andrew J. Weaver, and Christopher R. Barnes. Late ordovician glaciation under high atmospheric co2: A coupled model analysis. *Paleoceanography*, 14(4):542–558, 1999. ISSN 1944-9186. doi: 10.1029/1999PA900021.

Grzegorz Racki and Paul B. Wignall. Chapter 10 late permian double-phased mass extinction and volcanism: an oceanographic perspective. In J.R. Morrow D.J. Over and P.B. Wignall, editors, *Understanding Late Devonian And Permian-Triassic Biotic and Climatic EventsTowards an Integrated Approach*, volume 20 of *Developments in Palaeontology and Stratigraphy*, pages 263–297. Elsevier, 2005. doi: http://dx.doi.org/10.1016/S0920-5446(05)80010-X.

Callum Roberts. *The Ocean of Life: The Fate of Man and the Sea*. Penguin Books, 2013. ISBN 978-0143123484.

Allan Robinson and Henry Stommel. The oceanic thermocline and the associated thermohaline circulation. *Tellus*, 11(3):295–308, 1959. ISSN 2153-3490. doi: 10.1111/j.2153-3490.1959.tb00035.x.

Marco Roscher, Frode Stordal, and Henrik Svensen. The effect of global warming and global cooling on the distribution of the latest permian climate zones. *Palaeogeography, Palaeoclimatology, Palaeoecology*, 309(3-4):186–200, 2011. ISSN 0031-0182. doi: http://dx.doi.org/10.1016/j.palaeo.2011.05.042.

Alakendra N. Roychoudhury, Joel E. Kostka, and Philippe Van Cappellen. Pyritization: a palaeoenvironmental and redox proxy reevaluated. *Estuarine, Coastal and Shelf Science*, 57(5–6):1183 – 1193, 2003. ISSN 0272-7714. doi: http://dx.doi.org/10.1016/S0272-7714(03)00058-1.

Dana L. Royer. Co2-forced climate thresholds during the phanerozoic. *Elsevier: Geochimica et Cosmochimica Acta*, 70:5665–5675, 2006. doi: 10.1016/j.gca.2005.11.031.

J.B Sallée, Kevin Speer, R. Morrow, and Lumpkin R. An estimate of lagrangian eddy statistics and diffusion in the mixed layer of the southern ocean. *Journal of Marine Research*, 66(4):441–463, 2008. doi: https://doi.org/10.1357/002224008787157458.

R. Salmon. A simplified linear ocean circulation theory. *Journal of Marine Research*, 44 (4):695–711, 1986. doi: 10.1357/002224086788401602.

J.W. Sandström. Dynamische versuche mit meerwasser. *Ann. Hydrog. Mar. Meteorol.*, 1908.

Fabian Schloesser, Ryo Furue, Julian P McCreary Jr., and Axel Timmermann. Dynamics of the atlantic meridional overturning circulation. part 1: Buoyancy-forced response. *Progress in Oceanography*, 101(1):33–62, 2012. ISSN 0079-6611. doi: http://dx.doi.org/10.1016/j.pocean.2012.01.002.

Shane D. Schoepfer, Charles M. Henderson, Geoffrey H. Garrison, Julien Foriel, Peter D. Ward, David Selby, James C. Hower, Thomas J. Algeo, and Yanan Shen. Termination of a continent-margin upwelling system at the permian–triassic boundary (opal creek, alberta, canada). *Global and Planetary Change*, 105:21 – 35, 2012. ISSN 0921-8181. doi: http://dx.doi.org/10.1016/j.gloplacha.2012.07.005. New developments in Permian-Triassic paleoceanographic and global climate system research.

Henry Stommel and Arons A. B. On the abyssal circulation of the world ocean -ii. an idealized model of the circulation pattern and amplitude in oceanic basins. *Abyssal recipes*, 1959.

Henrik Svensen, Sverre Planke, Alexander G. Polozov, Norbert Schmidbauer, Fernando Corfu, Yuri Y. Podladchikov, and Bjørn Jamtveit. Siberian gas venting and the end-permian environmental crisis. *Earth and Planetary Science Letters*, 277(3-4):490–500, 2009. ISSN 0012-821X. doi: http://dx.doi.org/10.1016/j.epsl.2008.11.015.

J.R. Toggweiler and R.M. Key. Ocean circulation: Thermohaline circulation. In James R. Holton, editor, *Encyclopedia of Atmospheric Sciences*, pages 1549 – 1555. Academic Press, Oxford, 2003. ISBN 978-0-12-227090-1. doi: http://dx.doi.org/10.1016/B0-12-227090-8/00281-5.

Geoffrey K. Vallis. *Atmospheric and Oceanic Fluid Dynamics*. Cambridge University Press, Cambridge, U.K., 2006.

Geoffrey K. Vallis and Matthew E. Maltrud. Generation of mean flows and jets on a beta plane and over topography. *Journal of Physical Oceanography*, 23(7):1346–1362, 1993. doi: 10.1175/1520-0485(1993)023<1346:GOMFAJ>2.0.CO;2.

Amy F Waterhouse, Jennifer A. MacKinnon, Jonathan D Nash, Matthew H Alford, Eric Kunze, Harper L Simmons, Kurt L Polzin, Louis C St Laurent, Oliver M Sun, Robert Pinkel, Lynne D. Talley, C. B. Whalen, Tycho N. Huussen, Glenn S Carter, Ilker Fer, Stephanie Waterman, Alberto C Naveira Garabato, T. B. Sanford, and Craig M. Lee. Global patterns of diapycnal mixing from measurements of the turbulent dissipation rate. *Journal of Physical Oceanography*, 44:1854–1872, 2014. doi: 10.1175/JPO-D-13-0104.1.

Paul B. Wignall and A. Hallam. Anoxia as a cause of the permian/triassic mass extinction: facies evidence from northern italy and the western united states. *Elsevier*, 93: 21–46, 1996. ISSN 0036-8075. doi: 0031-0182/92/$05.00.

Paul B. Wignall and Richard J. Twitchett. Oceanic anoxia and the end permian mass extinction. *Science*, 272(5265):1155–1158, 1996. ISSN 0036-8075. doi: 10.1126/science.272.5265.1155.

R.T. Wilkin, H.L. Barnes, and S.L. Brantley. The size distribution of framboidal pyrite in modern sediments: An indicator of redox conditions. *Geochimica et Cosmochimica Acta*, 60(20):3897 – 3912, 1996. ISSN 0016-7037. doi: http://dx.doi.org/10.1016/0016-7037(96)00209-8.

A. M. E. Winguth, C. Heinze, J. E. Kutzbach, E. Maier-Reimer, U. Mikolajewicz, D. Rowley, A. Rees, and A. M. Ziegler. Simulated warm polar currents during the middle permian. *Paleoceanography*, 17(4):9–1–9–18, 2002. ISSN 1944-9186. doi: 10.1029/2001PA000646. URL `http://dx.doi.org/10.1029/2001PA000646`.

Arne M.E. Winguth and Ernst Maier-Reimer. Causes of the marine productivity and oxygen changes associated with the permian–triassic boundary: A reevaluation with ocean general circulation models. *Marine Geology*, 217(3-4):283–304, 2005. ISSN 0025-3227. doi: http://dx.doi.org/10.1016/j.margeo.2005.02.011.

Cornelia Winguth and Arne M.E. Winguth. Simulating permian–triassic oceanic anoxia distribution: Implications for species extinction and recovery. *Geology*, 40(2):127–130, 2012. doi: 10.1130/G32453.1.

Michael Winton. The damping effect of bottom topography on internal decadal-scale oscillations of the thermohaline circulation. *Journal of Physical Oceanography*, 27(1): 203–208, 1997. doi: 10.1175/1520-0485(1997)027<0203:TDEOBT>2.0.CO;2.

Carl Wunsch. *The Ocean Circulation Inverse Problem*. Cambridge University Press, 1996. ISBN 978-0521480901.

Carl Wunsch. The vertical partition of oceanic horizontal kinetic energy. *Journal of Physical Oceanography*, 27(8):1770–1794, 1997. doi: 10.1175/1520-0485(1997)027<1770:TVPOOH>2.0.CO;2.

Carl Wunsch. Determining paleoceanographic circulations, with emphasis on the last glacial maximum. *Elsevier*, 22(2):371–385, 2003. doi: 10.1016/S0277-3791(02)00177-4.

Carl Wunsch. The total meridional heat flux and its oceanic and atmospheric partition. *Journal of Climate*, 18(21):4374–4380, 2005. doi: 10.1175/JCLI3539.1.

Carl Wunsch and Raffaele Ferrari. Vertical mixing, energy, and the general circulation of the oceans. *Annual Review of Fluid Mechanics*, 36(1):281–314, 2004. doi: 10.1146/annurev.fluid.36.050802.122121.

R. Zhang, M.J. Follows, Grotzinger J.P., and J. Marshall. Could the late permian deep ocean have been anoxic? *Paleoceanography*, 16(3):317–327, 2001. doi: 10.1029/2000PA000522.